2007

An Investigation of the Frictional and Thermal Behavior of Oscillatory Sliding Line Contacts

Mongi Mansouri
Louisiana State University and Agricultural and Mechanical College, mmanso2@lsu.edu

AN INVESTIGATION OF THE FRICTIONAL AND THERMAL BEHAVIOR OF OSCILLATORY SLIDING LINE CONTACTS

A Dissertation

Submitted to the Graduate Faculty of the
Louisiana State University and
Agricultural and Mechanical College
in partial fulfillment of the
requirements of the degree of
Doctor of Philosophy

in

The Department of Mechanical Engineering.

By
Mongi Mansouri
M.M.E, Carnegie-Mellon University
B.M.E, University of Minnesota
December 2007

Acknowledgements

I am thankful to my advisor, Professor Michael M. Khonsari, for providing valuable advice and support throughout my degree program. I would also like to give thanks to members of my Graduate Committee: Professor Yitshak M. Ram, Professor Su-Seng Pang, Professor Wen Jin Meng, Dr. Jack Helms, and Professor George Z. Voyiadjis, and the Dean's Representatives, Professor Jianhua Cheng and Professor Evangelos Triantaphyllou, for their valuable observations and feedback.

I would also like to say Thanks to Professor Glenn Sinclair for discussions and his valuable feedback about contact theory. My Thanks also go to my Friend and colleague Dr. J.Y. Jang for the many helpful and informative discussions on Tribology. I must also say Thanks the Staff of the Mechanical Engineering Department including Diane Morgan, Debbie Hernandez, and Polly McKenzie for their help with administrative issues throughout my program.

This research was supported in part by the Louisiana Board of Regents [LEQSF (2002-05)-RD-B-03] through an industrial ties research program with Caterpillar Inc. The author greatly acknowledges the sponsors' financial support and encouragement.

Table of Contents

List of Tables

List of Figures

Nomenclature

A_r	Aspect ratio, $A_r = L/D$
a	Half-contact width (m)
B_i	Biot number.
C	Radial clearance (m)
C_r	Clearance ratio, $C_r = 2C/D$
c	Specific heat (J/kg·K)
c_i	Reduced model Coefficients.
D	Pin diameter, $D = 2r_s$
h	Ambient Heat Transfer Coefficient (W/m$^{2.}$.K)
k, K	Thermal conductivity (W/m·K), Dimensionless quantity.
L	Axial component length (m)
m	Component Index (m = 1 for moving, m = 0 for stationary body)
N	Rotational speed (rpm)
N_c	Number of cycles.
q, Q	Heat flux (W/m^2), Dimensionless heat flux.
p, P,	Contact pressure (Pa), Dimensionless quantity
P_e	Peclet number.
$\mathbf{r}$	Position vector $\mathbf{r} = (r, \theta)$, (x, y) in polar or Cartesian coordinates.
t	Time (sec)

$T, \Delta T$ Temperature rise, temperature difference (C)

u, U Displacement (m), Dimensionless quantity.

v Linear sliding speed (m/s)

V Dimensionless sliding speed, $V = v/v_r = \dot{\phi}/\omega$.

w_a Applied load (N)

α Contact half-angle (radians)

$\phi(t)$ Angular position of motion.

ϕ_m Amplitude of oscillation angle (rad)

λ Heat partition ratio.

κ, Λ Thermal diffusivity, Dimensionless value.

μ Coefficient of friction

ρ Mass density (kg/m^3)

σ, τ Normal and shear stresses (Pa).

ε, γ Normal and shear strains.

Θ Dimensionless temperature rise.

ω Angular frequency (rad/sec)

ξ, β Intermediate variables used in conformal contact model.

τ Dimensionless time, $\tau = \omega t$.

Υ Dimensionless period, $\Upsilon = \mathrm{T}/t_r$

Ω Dimensionless angular frequency, $\Omega = \omega/\omega_r$

Other notation:

Subscripts: a = mean or measured quantity, *b* = internal body quantity,

c = computed or contact quantity, *r* = ratio or reference quantity,

m = measured or maximum quantity, 0 = initial value, p = parameter.

A, B, C, D, E Symbols used to denote factors in factorial analysis of variance.

S_c, S_g, S_e Symbols used to denote the contact, gap, outer boundaries, respectively.

$\mathbb{R}, \partial\mathbb{R}$ Region, its boundary.

$[\ ]$ matrix or tensor quantity

$\{\ \}$ vector quantity.

Abstract

This research deals with an experimental and numerical investigation of the frictional and thermal behavior of pin-bushing pairs, operating at reciprocating sliding motion or under heavy loads. Large interfacial temperatures developed due to frictional heating can cause failure. Therefore, numerical prediction and analysis of the surface temperature under various operating conditions are important. Laboratory tests using a pin-bushing tester provided measurements of the friction coefficient and temperature. Hard coated and plain (uncoated) bushings, both made of induction hardened stainless steel, were tested. Lower coefficient of friction and surface temperature were observed in the case of the coated bushing.

In the modeling of the thermal problem, classical contact theory was used and a quasi-three-dimensional thermal model was developed and expressed by a set of partial differential equations and boundary conditions. Convective terms in the heat equation are handled by upwinding. This aspect of the computational model is important as it allows accurate solutions at high sliding velocities in concentrated contact.

The boundary condition at the pin-bushing sliding interface is expressed as a mixed formula of heating and cooling, both of which can be space and time dependent. In most published literature dealing with surface temperature prediction, the heat flux is assumed uniform, and regions outside the contact are assumed to be adiabatic for simplicity. This aspect of the research is important and contributes to the field.

Heat partitioning at the contact interface is computed as part of the solution. The method relies on coupling conditions at the interface, the material properties, and the solution gradients with respect to the normal direction at the interface. The effect of sliding is incorporated into the calculations. This is important in Tribology if it is desired to investigate heat flux division at

contact interface for any material combination and sliding velocity. The results can be used in design and material selection in many applications where the heat flow within conducting bodies is to be controlled.

Factorial analysis of variance was used to study the thermal response at steady state. This technique has not been applied previously to the analysis of surface temperature in pin-bushing joints.

Chapter 1. Introduction

Tribology is the science and technology of interacting surfaces in relative motion, and embraces the study of friction, wear and lubrication. Examples can be found in bearings, cams, gears, cutting tools, pin-joints, and the like. A typical tribological process is influenced by many parameters including the mechanical and thermal properties of the materials in contact, the lubricant, and the surrounding environment. These interacting physical factors make tribology an interdisciplinary science, involving physics, chemistry, mechanical engineering and materials science. Leonardo DaVinci (1452-1519) was one of the first scholars to study friction systematically. He focused on various friction mechanisms and drew a distinction between sliding and rolling friction.

Friction and Wear

Friction and wear of surfaces have a major role in the deterioration of machine elements. Proper knowledge and control of the friction and wear processes can lead to substantial savings of energy, maintenance and replacement costs. Frictional heating may cause contact failure of components in various heavy-duty machines.

Controlling the adverse influence of frictional heating has been a vital part of mechanical engineering design. With the development and constant improvement of computers and computational techniques researchers are in a position to conduct detailed modeling and simulation of the performance of engineering components subject to frictional heating. Tribological studies must include analyses of the thermal effects on friction and wear at the interface of the contacting materials. Because of its importance, there have been many studies of the influence of temperature on friction and wear. However, much of the past research has been

directed to understanding the performance of tribo-components where the load is constant and the velocity is unidirectional. Operation of many industrial machines and mechanisms is often in the unsteady boundary, mixed and even dry friction regimes. Unsteady friction occurs due to acceleration, deceleration and the periodic motion reversals and start/stop operations of the moving machine component in sliding contact. A particular case of interest is an operation in which the applied load varies dynamically and the sliding velocity reciprocates in an oscillatory fashion. Operating under high loads at slow speeds often leads to solid-solid contact where the applied load is carried mainly by the surface asperities at the contact region. Examples of such sliding systems include polymer sleeve bearings used for precision motion control in lightly loaded machines; pin-joint assemblies in undercarriage systems used in mining, demolition, heavy construction, and waste disposal application, and hydraulic seals for reciprocating piston rods used in actuators, pumps and cylinders.

Friction and Temperature

Friction converts mechanical energy primarily into thermal energy, which results in a temperature rise. In concentrated contacts, a film lubricant exists to protect the surfaces. Yet, excessively high loads or severity of the operating conditions can bring about large friction intensity that causes a substantial temperature rise on the surface. Thus, development of appropriate correlations between the surface temperature and friction is needed for the engineer to guard against failure at design stage.

The coefficient of friction depends on the nature of the surface and can vary widely depending on whether the surfaces are dry/unlubricated or lubricated by solid lubricants, greases, hydrodynamic or elastohydrodynamic films. The evaluation of the coefficient of friction is primarily based on experimental measurements, and does not lend itself to theoretical prediction.

A simplifying assumption often made is that all the frictional heat is conducted into the solids in contact. However, the presence of a lubricant in the immediate vicinity of the contact results in convection heat transfer, thereby cooling the surfaces close to the contact. This would generally tend to lower the predicted temperature.

Calculations of the contact surface temperature at the surface asperity level involve the calculation of the so-called flash temperature. Flash temperature refers to the transient temperature, above the bulk temperature, that a pair of surfaces in sliding contact experience, as a result of friction energy dissipation. However, the temperature level, not rise, in the contact area is frequently of major concern in predicting problems associated with excessive local temperatures. The surface temperature rise can influence the local surface geometry through thermal expansion, causing high spots on the surface, leading to load concentration and severe local wear. The temperature level can also cause physical and chemical changes in the surface layers and the bounding solids. These changes can lead to transitions in lubrication mechanisms and wear phenomena resulting in significant changes in the wear rate. Therefore, an overall system-heat transfer analysis may be required to predict the bulk and the local surface temperatures.

Procedures for modeling and solving real thermal problems generally involve computational methods such as the finite element method. Finite difference and boundary element methods have also been applied to the study of surface temperature in concentrated contacts.

Damage Due to Thermal Effects

Thermal galling is a failure mode of surfaces of similar chemical composition or surface hardness in sliding contact in which there is gross metal transfer from one surface to the other[1];

see Figure 1[1]. Elevated surface temperatures and high surface loads increase the tendency of galling. Galling is believed to occur when operating conditions force direct metal-to-metal contact and bonding occurs at an asperity level where very high stresses and large surface temperatures occur. As the surface undergoes sliding, galling may occur resulting in a cold-welding type of a failure. Shear forces, at the sliding interface subsequently lead to wear of the welded parts. This often leads to the destruction of machinery components, and costly downtime. Conventional lubricants can control galling but often fail under high temperatures. Since metal transfer (adhesive wear) appears to be one of the first steps in a galling failure, the appropriate combination of dissimilar materials (metal coatings, inserts, etc.) is often used to delay or eliminate the tendency to gall.

Scuffing damage is the lifting of the fibers on the surface of a material when the surface is in sliding contact with another[1]; see Figure 2(a)[1]. For instance, damage results from contact between the bearing and journal surfaces, due to a reduction in the localized clearance. This causes an increase in the local operating temperature and melting and subsequent removal of the bearing material. Typically, insufficient clearance or inadequate oil supply can cause scuffing damage. If scuffing persists, then scoring and fatigue of the material can occur[1]; see Figure 2(b)[1].

Thermally induced seizure occurs when there is partial or complete clearance loss in a bearing due to thermal effects. Too small a clearance leads to seizure by a thermal ratcheting effect. This occurs when the clearance has decreased by a swelling process to the point when the heat removed by conduction and by lubricant flow does not balance the heat generated [1]. The

[1] www.gvbearings.com

shaft attempts to expand against the bushing which increases the contact pressure, and consequently the heat generation. Beyond the point of seizure, the interface temperature will increase at an unknown rate until the bushing lining material collapses. If the thermal conductivity of the material is low, only a thin layer may be affected and the process may recover and continue to operate, depending on the application.

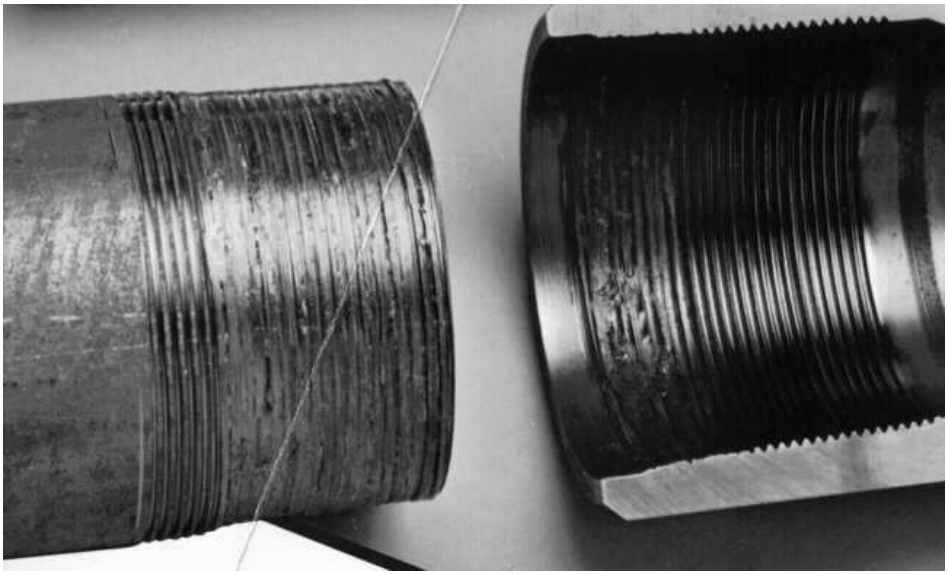

Figure 1. Thermal galling damage

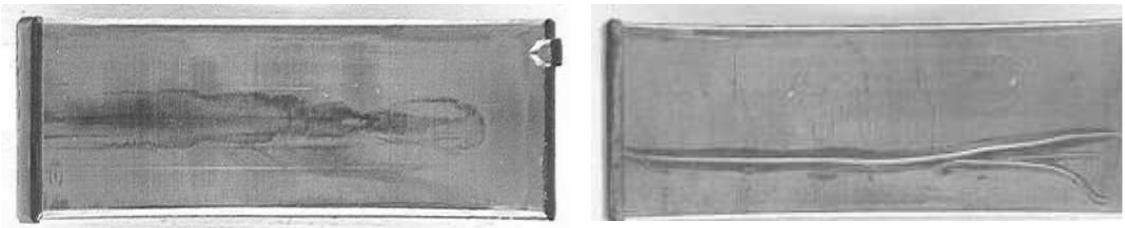

(a) Thermal scuffing damage (b) Thermal scoring damage

Figure 2. Thermal scuffing and scoring patterns

Pin-Bushing Joints

Pin-joint assemblies are found in undercarriage systems used in mining, demolition, heavy construction, waste disposal applications, earth moving machinery, as well as hydraulic

seals for reciprocating piston rods used in linear hydraulic actuators, pumps, cylinders and engine crank-pin-piston assembly. Pin-joint assemblies in earth moving machinery are used in combination with a linkage system to handle intermittent heavy load cycle and generally operating at low speeds. Table 1 shows typical operational parameters for the pin-joint assemblies found in wheel loaders[2]. The mean contact pressure and width of contact are estimated using Hertzian theory. According to Table 1, for a nominal coefficient of friction of 0.1, the amount of frictional heat generation ranges from 39 kW/m^2 to 1500 kW/m^2.

Table 1. Typical operating parameters

Parameters	Application range
Pin Diameter (mm)	100 – 180
Bush ID (mm) Bush OD (mm)	120 – 200 180 – 230
Bearing Length (mm)	100 – 150
Applied Load (kN)	1000 – 3600
Oscillation speed (rpm)	0.25 -- 8
Oscillation angle (deg)	±6 – ±60
Contact pressure (MPa)	150 – 200
Contact angle (deg)	50 – 110

Figures 3(a, b)[3] show examples of industrial applications (circles indicate pin-bushing locations). Heavy-duty pin-joint assemblies in earthmoving machinery such as wheel loaders are often heavily loaded with the added requirement that they must sustain repeated or intermittent oscillatory motion under a specified load-cycle. While the bucket swings back and forth, there is a significant amount of heat generation at the interface of the pin joint. Close proximity of the pin and sleeve with no provision for external cooling often generate very high contact

[2] Internal communication, Caterpillar Inc.
[3] Photos courtesy Caterpillar Inc.

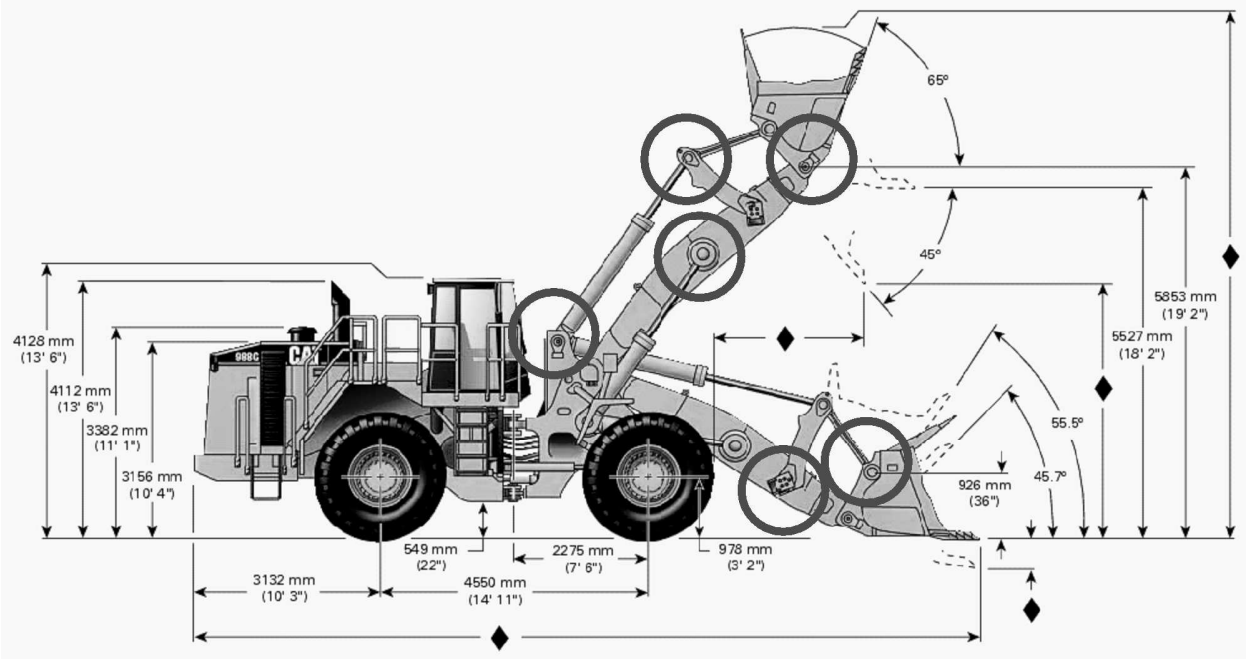

Figure 3a. Industrial applications of pin-bushing joints – wheel loader

Figure 3b. Industrial applications of pin-bushing joints: bucket.

temperatures, which if exceeded beyond a limit can result in thermal galling, scuffing, and seizure failure.

The pin and bushing are typically made of induction-hardened steel alloy. The bushing surface may be treated with protective metal coating to reduce friction and wear. The pin-bushing pair may be packed with grease during assembly. During operation, automatic grease feeders may be used or grease is applied periodically.

There is no provision for a continuous supply of lubrication in the system and the packed grease is the only source of lubrication. After some time of operation in the field, the pin-bushing pair exhausts the supply of grease packed in the assembly by normal operational leak or degradation. The absence of proper lubrication leads to the wear of the anti-friction liner on the surfaces of the pin-bushing pair. Further operation causes metal-to-metal contact between the pin and the bushing leading to large heat generation in the contact region. The absence of proper lubrication, very high loads and ineffective cooling leads to surface failure either by galling or thermally induced seizure. The time it takes for initial failure to occur is generally long; But once failure starts, the surface temperature at the pin-bushing interface shoots up to very high values introducing possible galling, scuffing or seizure, depending on the operating conditions.

The bushing is connected to a linkage arm, and, during operation, the pin and bushing may be oscillating relative to one another while the bucket is being lifted or lowered. During loading or unloading, the pin may be stationary while the bushing swings back and forth. In some applications, and this is determined by the purpose and function of the machine, the pin rotates while the bushing is stationary with housing. The moving parts are assumed to follow a reciprocating sliding motion or operate under a well defined load cycle. It is this phase of the operation that is the focus of this work. The transient and steady state temperature behaviors are of interest. In-situ measurements of the surface temperature are difficult due to complications in the placement of thermocouples near the sliding interface. For this reason, in the numerical treatment of these problems, solution to the temperature field is computed everywhere within the

solid media. This allows measurements of the temperature at points away from the sliding interface to be used in the verification of the predicted values.

Scope of This Work

This research deals with the modeling and analysis frictional and thermal behaviors of pin-bushing joints that are operating at reciprocating sliding speeds under prescribed load cycles. The influence of the various operating parameters on the surface temperature rise developed at the sliding interface is investigated. The study can be useful in component design, material selection, and the choice of operating parameters, for the purpose of prolonging life and avoiding thermal failure.

Overview of the Dissertation

Chapter 2 presents an overview of existing knowledge and published work with regard to the prediction of surface temperature. An experimental setup is described and selected experimental data are presented in Chapter 3. A mathematical model of the thermal problem for the prediction of surface temperature rise is described in Chapter 4 for a general configuration of two bodies in sliding contact. Thermo-elastic governing equations and mechanical boundary conditions are presented in Chapter 5 for a general deformation state. Dimensionless governing equations are developed in Chapter 6. In Chapter 7, the formulation is applied to simple configurations found in the literature, and then to the pin-bushing joint in Chapter 8. Several examples of published work in the field are considered and compared to the numerical results obtained using the computational code. The pin-bushing case study is treated in more details in the remainder of this document. In Chapter 9, analytical contact models are described that are borrowed from classical contact theory, and used to estimate the contact parameters and heat flux input in the pin-bushing joint. In Chapter 10, thermal analysis of a set of pin-bushing pairs is

presented. The analysis represents a first attempt to study the problem, and relies on the classical Hertzian contact model to estimate the heat flux input and the finite difference method to compute the thermal problem. Subsequently, the conformal contact model and the finite element method were utilized to model the problem and compute the solution more realistically. A simplified mathematical model for the experimental setup and a comparison of finite element solutions with experimental data are presented and discussed in Chapter 11. A factorial analysis of variance is carried out and results are presented and discussed in Chapter 12. General conclusions and recommendations for enhancement of the solution method and future work are discussed in Chapter 13.

Chapter 2. Overview of the Literature

Surface temperature developed at sliding contact interfaces in rotating machinery has a major influence on material properties, surface degradation and wear, galling initiation and scuffing damage. The converse is usually true: the frictional and wear characteristics of the surfaces in contact have a pronounced effect on the thermal and mechanical behavior in a frictional process. Thermal galling, scuffing, and thermally induced seizure are examples of failures attributed to surface temperatures at sliding contacts.

Ling et al. [2], relying on Block's postulate for the flash temperature at interasperity contact, predicted thermal galling when the temperature of sliding surface exceeds the recrystallization value of the metal. A galling criterion was then derived in terms of sliding velocity, applied load, and time. Dyson [3], in a review on scuffing failure, stated that the metallurgical reaction on a scuffed or a galled surface is characterized by the formation of a hard white etch-resistant layer on the sliding surfaces. The presence of this transformed layer, often separated from the bulk of the material by a tempered layer suggests that the scuffed surfaces have been subject to high temperatures and rapid cooling. Bishop and Ettles [1] investigated the seizure of journal bearings due to frictional heat and the thermoelastic behavior of the journal. The pin was assumed to be free to expand radially due to temperature gradients but remain circular. The bushing was assumed to conform to the pin over the contact angle but was not allowed to expand. The frictional heat flux, and therefore, the temperature rise depended on the sliding speed, projected load, and clearance. Bishop and Ettles derived a seizure number as the ratio of the limiting PV factor to the radial clearance (that should not be exceeded for safe operation). Many other researchers in the field such as Dufrane et al. [4]; Khonsari and Kim [5]; Hazlett and Khonsari [6]; Wang et al. [7]; Wang [8]; Pascovici et al. [9]; Krithivasan and

Khonsari [10]; investigated seizure in dry and lubricated bearings by considering the effect of surface temperature rise on the clearance loss at the contact interface.

A study of the influence of temperature on the tribological behavior in processes with frictional sliding contact requires accurate prediction of the contact temperature. The normal operation of such processes is controlled by the frictional and wear behavior at the contact interface. Thus, a correlation between the surface temperature and friction and wear, would provide a good basis for predicting failure and therefore the operational limits of the application.

In a number of publications such as Berthier et al. [11] and Kennedy et al. [12], temperature predictions using a computational model are correlated to measured friction and wear behaviors. The surface temperature depends on the size and shape of the contact region, the coefficient of friction, the applied load, the sliding velocity, the thermal properties of the contacting bodies; in components that undergo oscillatory motion, the amplitude and frequency of oscillation also play important roles. It also has been reported ([11]-[17]) that the tribological behavior in oscillating contacts can be quite different from that in unidirectionally sliding contacts.

Theoretical prediction of surface temperature due to frictional heating in unidirectional sliding at constant velocity is pioneered by (Blok [18]; Jaeger [19]; Holm [20]; Archard [21], Francis [22]). Such early analytical works involve calculation of the temperature in a semi-infinite body subjected to a heat flux on its surface, with the body moving relative to the heat source. Figure 4 shows a general configurations used by Jaeger and others in early analytical treatments of surface temperature. The analytical solution is fundamentally based on a Greens function technique expressed in integral form or integral transform technique ([11]-[24]).

The temperature increment at point s on the surface of body, at time t, due to a heat flux $q(s',t')$ generated at point s' at time t' is given by [23]:

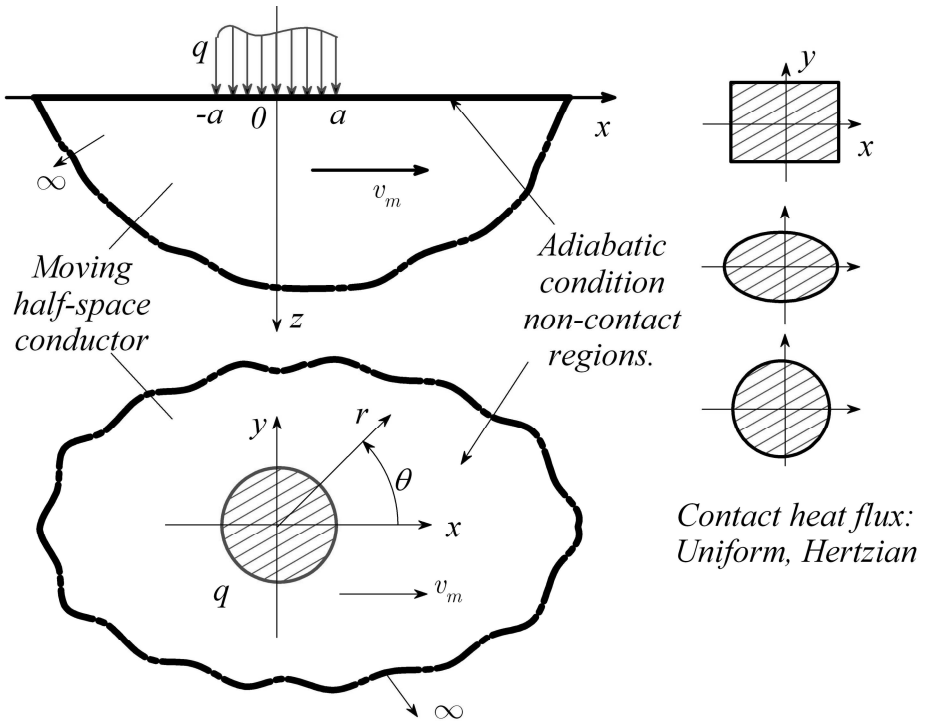

Figure 4. General configurations used in analytical studies of surface temperature.

$$dT = \frac{q(s',t')ds'dt'}{2\pi k\left(t-t'\right)}\exp\left[-R^2(s,s')\Big/\left(4\kappa\left(t-t'\right)\right)\right]$$

where

$$R^2(s,s') = \left[\left(s-s'\right) - \int_{t'}^{t} v(t')dt'\right]^2$$

and $v(t)$ is the sliding speed, assumed to be a function of time and in the direction of *s*. The surface temperature at any point is calculated by integrating the above increment from the initial time t_0 to the desired time t and over the entire domain S of the heat flux:

$$T(s,t) - T_0(s) = \int_{t_0}^{t} \int_{S} \frac{q(s',t')}{2\pi\rho c\kappa\left(t-t'\right)} \exp\left[-R^2(s,s') \Big/ \left(4\kappa_b\left(t-t'\right)\right)\right] ds'dt'$$

The controlling parameter in deriving integral solutions is the Peclet number, often defined as $P_e = v_m a \big/ (2\kappa)$., where v_m is the sliding velocity, a is the radius of the heat source, and κ is the thermal diffusivity for the conducting body. The *Peclet* number represents the ratio of heat diffusion characteristic time – i.e., $a^2 \big/ \kappa$ – to the transit time of the heat source – i.e., $2a \big/ v_m$. When the Peclet number becomes large, typically $P_e > 5$, a solution is obtained by neglecting heat diffusion over the plane of heat source. The heat equation is simplified and the solution is proportional to $1 \big/ \sqrt{P_e}$ ([13]-[16], [24]). For small Peclet number, $0 < P_e < 5$, the solution is determined by numerical integration of the integral expression.

Gecim and Winer [24] used integral transforms in order to solve the steady state thermal problem, for large Peclet numbers, in a rotating cylinder subject to surface heating and convective cooling. The assumption in [24] was made that at high sliding speeds, heat conduction is negligible in the angular direction, thus reducing the heat equation in cylindrical coordinates to one dimension.

Tian and Kennedy ([13]-[16]), based on a heuristic reasoning, proposed simple correlations for the steady-state temperature for the entire range of Peclet numbers. Such theoretical studies are valuable and provide insight into the surface temperature behavior for unidirectional sliding speed. However, they rely on the restrictive assumption of concentrated contact where it is assumed that the contact region is small compared to bulk dimensions, and that the conductor resembles a semi-infinite body. In addition, uniform heat flux is assumed to

simplify the analytical derivation. Often, such analyses begin with the assumption of a point contact, which provides solutions to planar contact problems.

One of the original studies that dealt with the prediction of surface temperature rise in oscillatory sliding contact is that by Hirano and Yoshida [17]. They conducted an analytical treatment of a contact heat transfer problem with a sinusoidally moving heat source. Their main interest was to compare oscillatory sliding results with those of unidirectional sliding. Results in [17] predicted a larger temperature rise than that of unidirectional sliding friction for the same heat input. The difference was particularly magnified at higher oscillation frequencies or larger amplitudes. The work in [17] considered a model where the slider is adiabatic, and the heat transfer from the exposed (non-contact) surface at the interface is negligible. See Figure 5.

Kennedy et al [12] considered the case of dry rectilinear sliding system between a pin and flat in small oscillatory amplitudes in order to study the relationship between the contact temperatures, the friction coefficient and wear rate in polymeric sliding bearings. Infrared radiation pyrometry was used to experimentally measure the surface temperature. Their finite element modeling of the surface temperature showed good agreement with experiments. Temperature predictions from the computational model were then correlated to measured friction and wear behaviors.

Tian and Kennedy [16] considered the problem of frictional heating in oscillatory sliding, and applied the Green's function method for finite contacting bodies derived in a related study [13] to predict surface temperature. Utilizing this model and based on experimental measurements, it was concluded that the repetitive periodic heating is responsible for additional increase in the steady state surface temperature. Based on the work in ([13]-[16]), the steady state nominal surface temperature rise is influenced by convective cooling and the sliding system geometry.

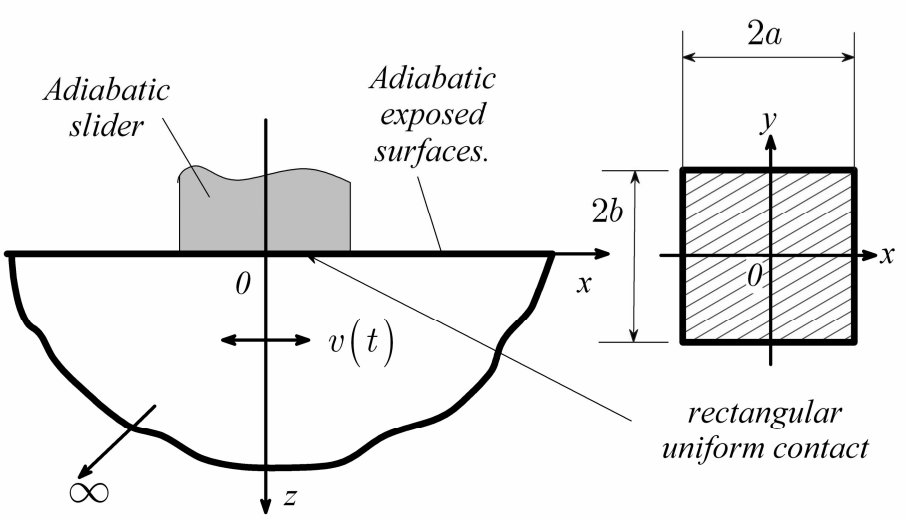

Figure 5. Schematic of the model and coordinate system used in [17]

Greenwood et al. [25] assumed the contact region to be small enough for conducting medium to be treated as a half-space with the slider remaining stationary. Their analysis pertains to applications that involve small-amplitude reciprocating contact, such as those encountered in fretting.

Furey et al. [26] developed theoretical model and solution in order to predict the thermal response to frictional heating in systems with oscillating fretting contact. The solution to the thermal boundary value problem was developed using the boundary integral equation method. The proposed solution technique was based on a full-space moving Green's function, used to transform the problem into a set of coupled integral equations for unknown boundary functions. In [26], the classical assumption of small concentrated contact and semi-infinite conducting body was also made to allow for the use of a full-space Green's function solution.

In practical applications, both contacting components are finite and conduct heat at the interface. Convective heat transfer boundary conditions at the interface, and nonlinear and second order effects such as radiation heat transfer and thermal contact resistance at the interface

may become important. The contact area, often idealized as small compared to the dimensions of the contacting bodies such as in the classic Hertzian theory, may be comparable to bulk dimensions such in conformal contacts. In analytical treatments, the frictional heat division at the interface of two bodies is approximated using Block's postulate, or a variation of it.

In the chapters that follow, an attempt is made to study the problem of surface temperature prediction using fundamental physical laws, and to analyze surface temperature change in response to key input parameters. Use is made of classical contact theories and their validity is discussed. This work was initiated before an experimental setup was available. But the documentation will begin with a description of the experimental data, followed by the mathematical modeling aspect of the problem. In some of the early simulations, the coefficient of friction was assumed based on available data in Tribology handbooks. The experimental data provided a more accurate depiction of the friction coefficient, which was used in all subsequent simulations.

Chapter 3. Experimental Setup

An overview of the test rig used in measurements is presented in this chapter. In order to perform laboratory tests, a test rig is utilized which was based on a scaled down model of actual pins-bushings found in real applications. This requires scaling down the sizes of the pin and bushing and the magnitude of the applied loads. The experiments are carried out with similar oscillation amplitude and contact pressure as the actual applications as well as similar Peclet numbers to determine the speed. All tests were performed at room temperature. The test rig is located at the LSU Center for Rotating Machinery laboratory.

Overview of the Tribo-Tester

Measurements of friction and temperature on an oscillating pin-bushing assembly are conducted on a friction tester (Lewis LRI-8H). Figure 6 shows an apparatus of the Lewis LRI-8H tester used in experiments. The machine is capable of testing steady rotational as well as oscillatory motion. For oscillating mode, the pulleys and belts used for rotation are replaced by a crank-rocker arm (15). The crank arm (15) is connected at the bottom to the DC motor (16) via a jack pin (19) and to spindle hub (11) at the top. This is a four-bar mechanism that can be modified to provide a wide range of oscillation angles and frequencies. The four-bar linkage also provides a smooth sinusoidally varying motion as shown in Figure 7. In the test rig, the pin is oscillating, while the bushing is stationary. The bushing is inserted into the housing (6) and locked with a set screw into a 0.060-inch deep hole drilled onto the bushing outer surface. The housing (6) mounts into the stabilizing load cartridge (9), where it is locked in place with a snap ring. The stabilizing load cartridge rides on linear bearings (10) that allow it to float up and down to reduce vibration impact and prevent slip. The housing (6) is free to rotate, but this

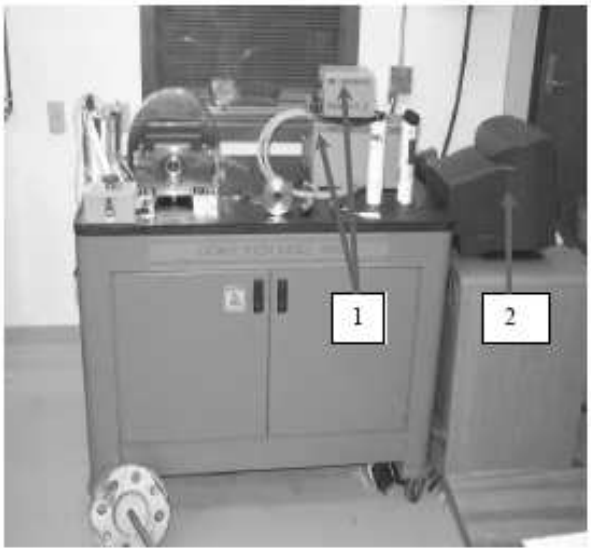

(a) Overview of the Tribo-tester

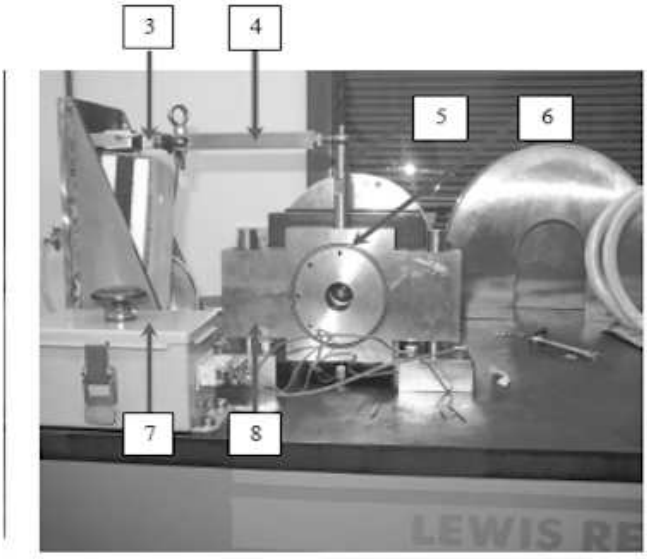

(b) Measurement sensors

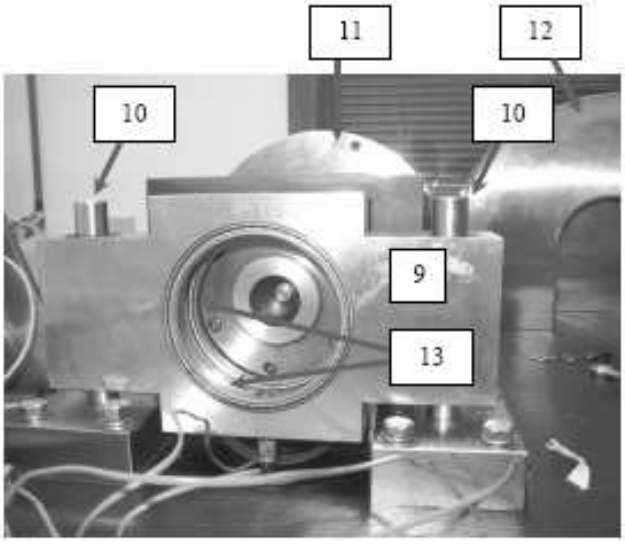

(c) Details of the bearing support

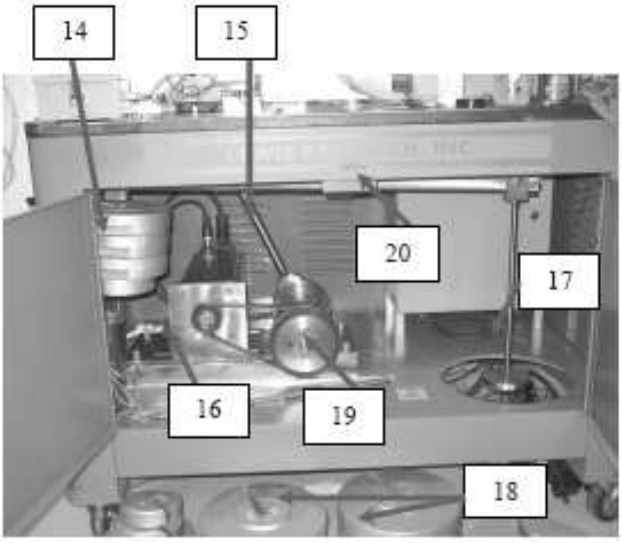

(d) Setup for Oscillations

Figure 6. The LRI-8H Tribo-Tester

rotation is acted against by the torque arm (5) that is connected to a load cell (3) through the connector arm (4). This allows measurement of the frictional force during oscillation. The torque arm is screwed into the top of the housing through a hole in the stabilizing load cartridge (9), and connected to a load cell (3), as shown in Figure 6 (b). Dead weights (18) are placed on a hanger bracket (17) as shown in Figure 6 (d). The load arm is supported on a 10:1 ratio lever

(20), with the output side pulling the free stabilizing load cartridge downwards bringing it in contact with the pin. Placing a 100-lbs weight on the hanger multiplies into an applied normal load of 1000 lbs at the contact.

The motion profile generated by the four-bar mechanism, described in Figure 6(c), is explained schematically in Figure 7(a). The mathematical equations describing the relationship between the input driving rotational motion and the output oscillatory motion are written as follows:

$$r_1 + r_4 \cos(\theta_4) - r_2 \cos(\theta_2) - r_3 \cos(\theta_3) = 0$$

$$r_4 \sin(\theta_4) - r_2 \sin(\theta_2) - r_3 \sin(\theta_3) = 0$$

where r_i, θ_i are respectively the lengths of the linkage arms and the angles they make with the horizontal direction, measured counterclockwise. The algebraic equations were solved iteratively using the Newton Raphson method. The generated motion profile is plotted by Figure 7(b).

Basic Components of the Tribo-Tester

Figure 8 shows the test parts of the oscillating pin-bushing assembly, namely the housing, the pin, and the bushing. Detailed drawings of the pin, bushing, and housing are also presented in Figure 9(a, b), and 10, respectively. The Pin has a #30 milling machine taper and connects into the spindle through a draw bolt.

Friction and Temperature Measurements

Measurements of the coefficient of friction and temperature are available on the LRI-8H tester. The friction force is sensed by a load cell that is connected to the torque arm. The torque arm transmits the friction force at the contact interface to the load; see Figure 11 for details. The

onboard driving software computes the coefficient of friction by taking the ratio of the measured friction force to the applied load.

The temperatures at four different locations on the bushing surface are measured using four different thermocouples. The locations of the thermocouples are as illustrated in Figure 12. The maximum sampling rate of the LRI-8H is 0.05 Hz. Readings are made, averaged, and displayed or recorded at a minimum of 20-second intervals.

Two types of bushings are tested, both made of carbon steel. The production bushing has a plain inner-wall surface coated with a layer of a hard metallic coating to reduce friction and help protect against wear; see Figure 13. The other bushing is of identical size but no coating is applied to it. Tests were carried out for each bushing at different applied loads at a frequency of 1.34 Hz, and oscillation amplitude of ϕ_m = 45 degree. Caterpillar ALG #1 grease was applied at the beginning of the tests. This is heavy-duty multipurpose grease that contains 5% MoS_2. For wear analysis, the bushing being tested is weighed before and after the test. Wear was estimated by the amount of material lost during a test.

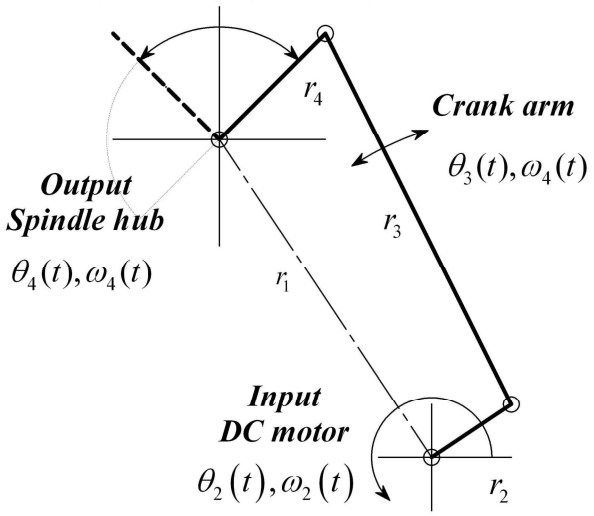

Figure 7a. The 4-bar driving mechanism

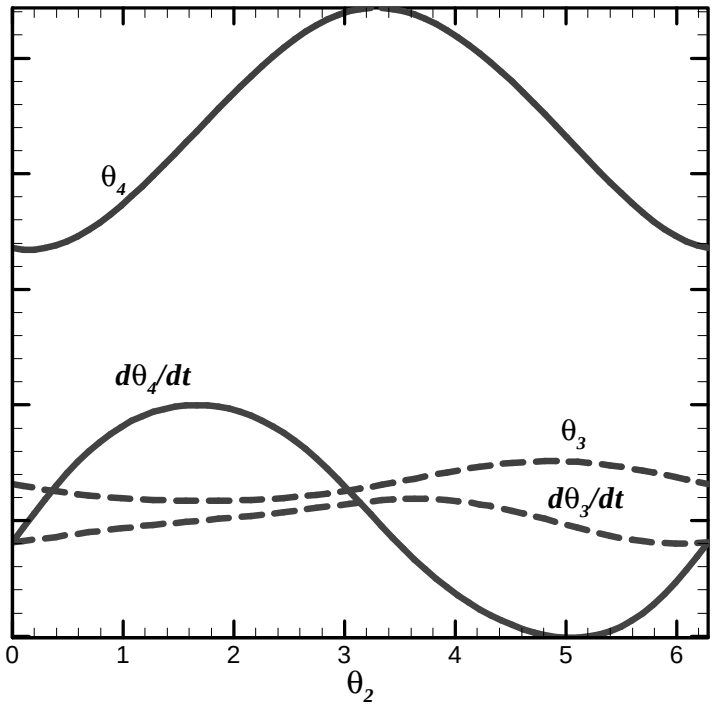

Figure 7b. The derived motion profile

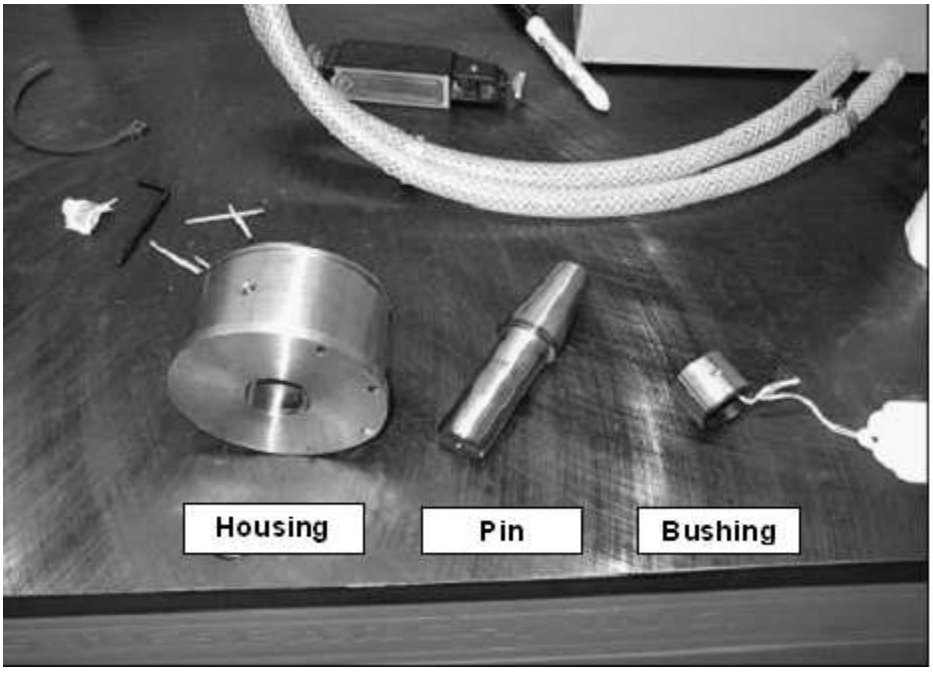

Figure 8. pin-bushing components used in experiment.

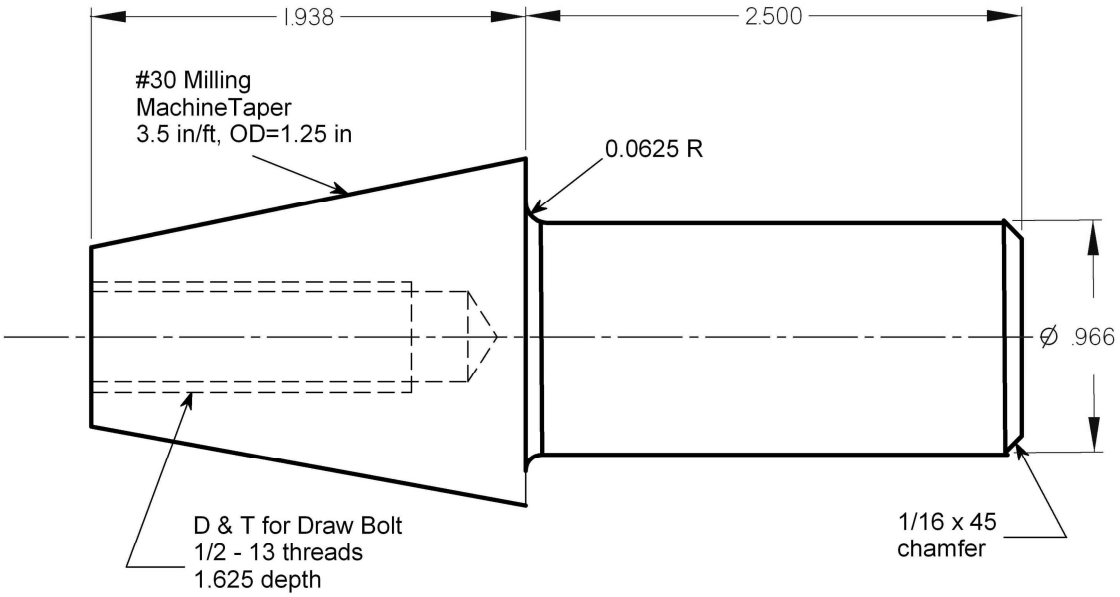

Figure 9a. Schematics of the pin.

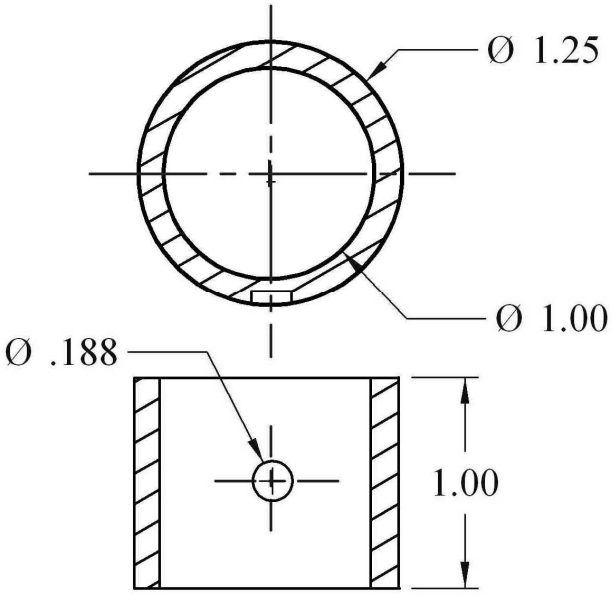

Figure 9b. Schematics of the bushing.

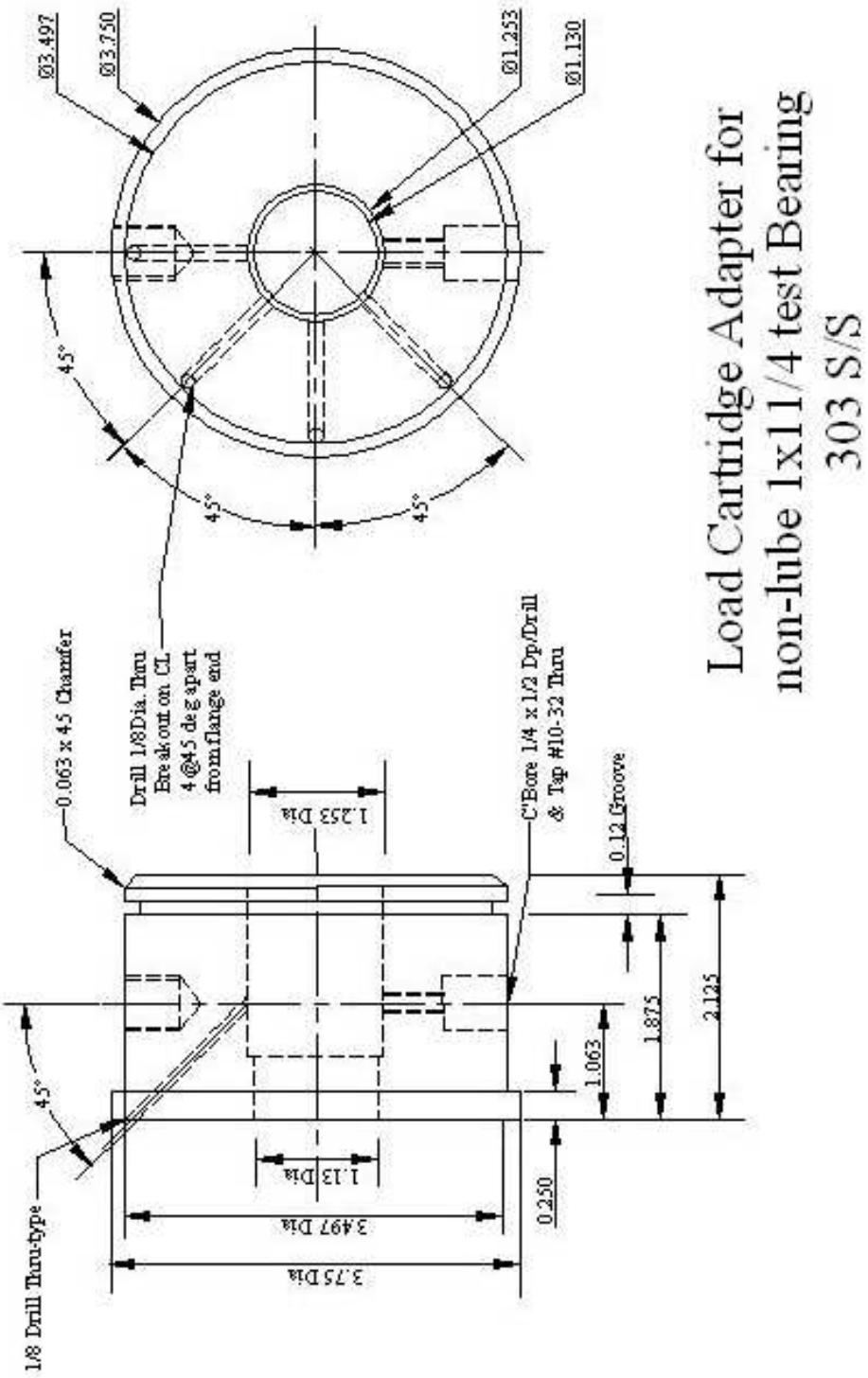

Figure 10. Schematic of the housing and its dimensions.

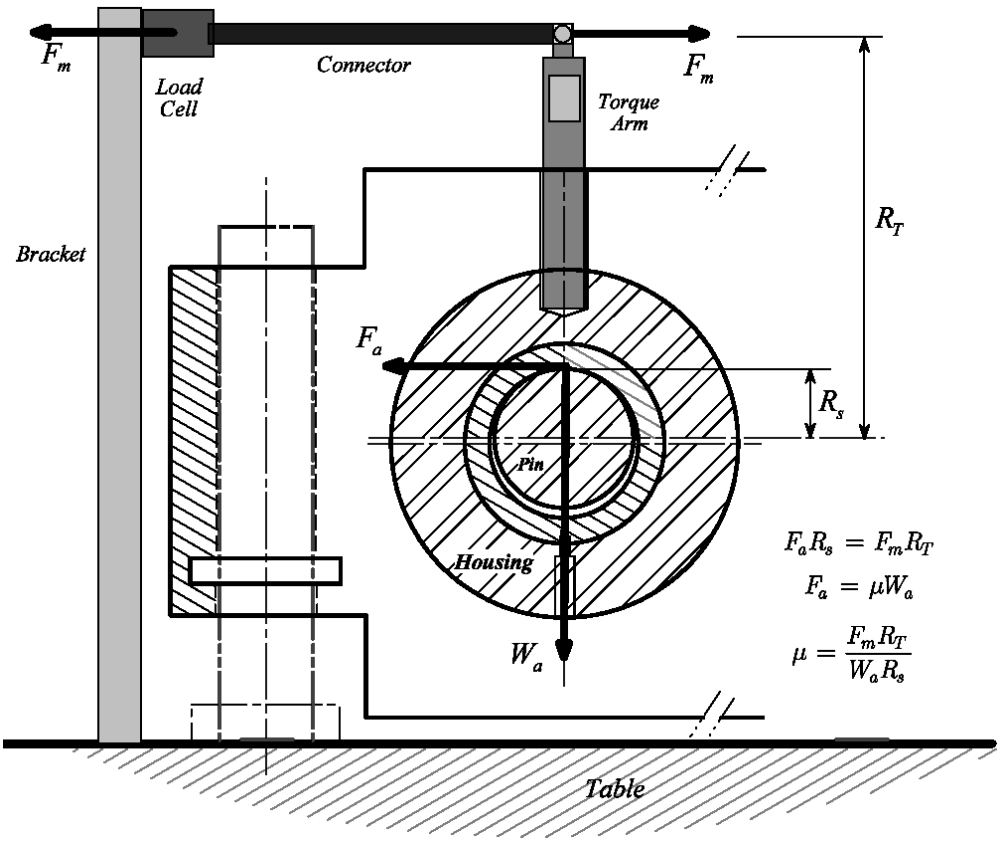

Figure 11. Friction measurement setup.

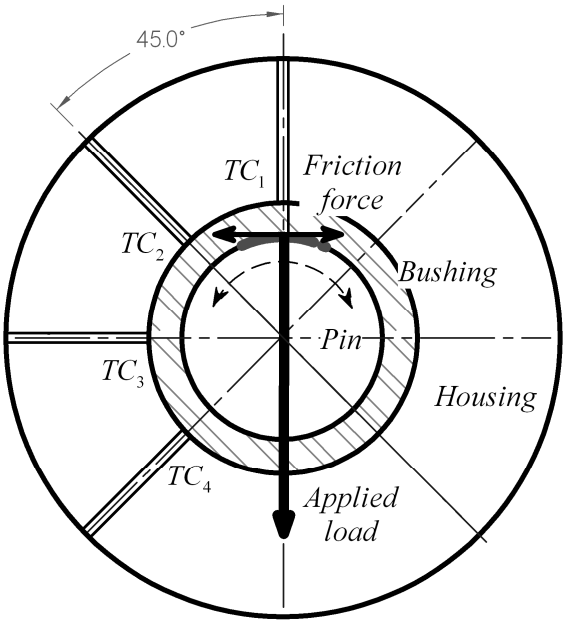

Figure 12. Temperature measurements - thermocouple arrangement.

Figure 13. Bushing used in experiments.

Experimental Results

Selected experimental results are shown below for both the production (coated) and plain (uncoated) bushings. Figures 14–15 show the temperatures measured at the four selected thermocouple locations, as described earlier in Figure 12, and the coefficient of friction (COF) measured as described in Figure 11, for the two pin-bushing pairs. The production bushing and pin are made of induction hardened steel to an estimated Hardness of 56 Rockwell C. The bushing inside surface is coated with a hard protective layer of metal film. A layer of grease was applied over the expected contact region on the bushing before the test. The test duration was set to 8 hours, and the applied load to 1000 lbs. Figure 14 shows the results for the production bushing. A steady state surface temperature condition appears to have been reached during this time frame as seen on the experimental temperature plots. Figure 14 reveals that when the temperature stabilized, a coefficient of friction of 0.115 was sustained. No visible failure resulted in this test to the pin or bushing surface. Figure 15 shows a similar test performed with a plain (uncoated) bushing made of mild 4041 steel. A slightly higher coefficient of friction and therefore larger temperatures were recorded as shown.

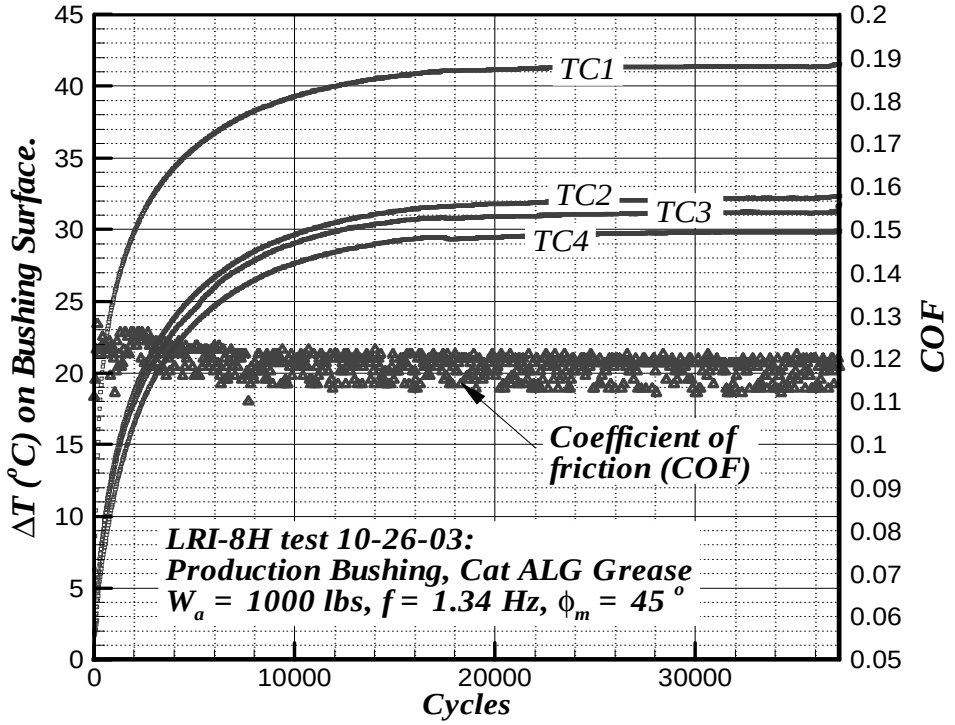

Figure 14. Friction and temperature measurements - production bushing

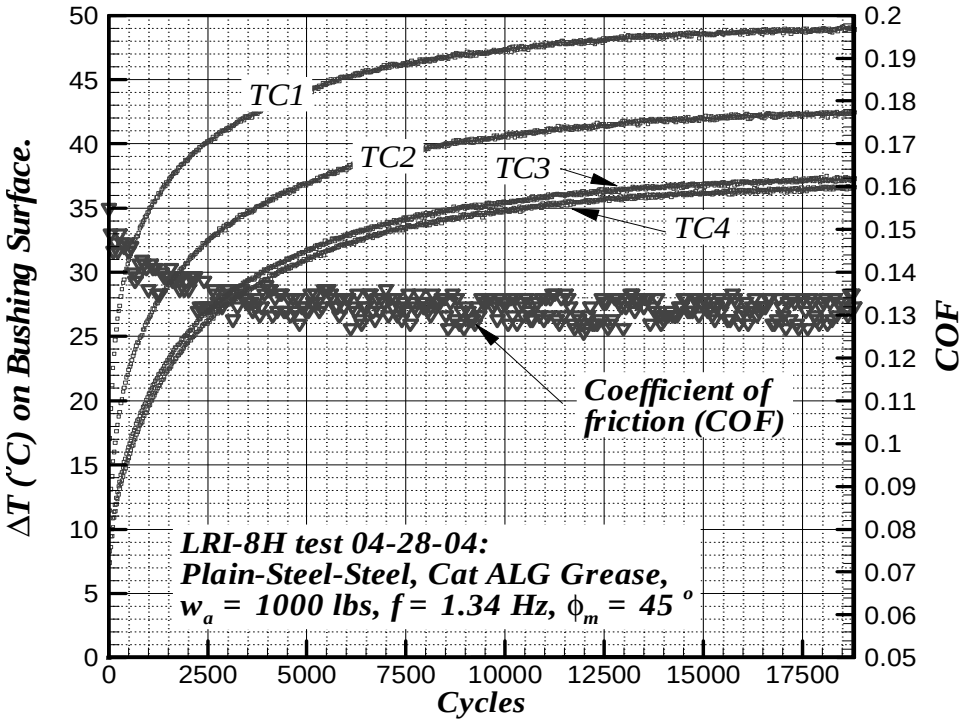

Figure 15. Friction and temperature measurements - plain bushing

A closer look at the coefficient of friction behavior during several oscillation cycles reveals some differences as well. Stability of the coefficient of friction is achieved within one measurement cycle (21 seconds) for the production (coated) bushing. For the uncoated bushing, the coefficient of friction took longer to become steady across the oscillation cycles; see Figures 16 and 17. Figures 18 and 19 show the behavior of the coefficient of friction over one measurement cycle. For the production bushing, the coefficient of friction in the counterclockwise direction is higher than its values in the reverse direction. This is not the case for the uncoated bushing. It may be explained by the surface roughness patterns being random in the case of the uncoated bushing case, while surface roughness in the coated bushing may have a directional pattern that favors a lower coefficient of friction with the direction of motion. Figures 20 and 21 show the behavior of the coefficient of friction over one oscillation cycle.

In both coated and uncoated bushings, the coefficient of friction cyclic variation is repeated prior to wear or surface damage. During the course of the experiments, wear damage occurred and the coefficient of friction value became suddenly large. When this occurred, the test was stopped.

The measured COF embodies much of the tribological behavior at the contact interface, and therefore significantly influences the thermal behavior at the contact interface and within the components. The COF was curve-fit for use in simulations. In most cases, the form of the COF follows a decaying function of time of the form:

$$\mu_c = c_1 + c_2 \exp\left[-t/\left(c_3 \mathrm{T}\right)\right]$$

where T is the period of oscillation and *t* is the time, and the dimensionless coefficients c_i are obtained by linear regression.

Two instances of the measured coefficient of friction are shown in Figures 22-23 showing the scatter plots, and Figures 24 - 25 showing the curve fit plots according the above decay function. The curve fit of interest is the curve in the middle of the 90% prediction band. The estimated curve fit coefficients are:

$$c_1 = 0.1173,\ c_2 = 0.0056,\ c_3 = 7339.546 \text{ :: production bushing}$$

$$c_1 = 0.1316,\ c_2 = 0.017,\ c_3 = 1548.33 \text{ :: plain bushing}$$

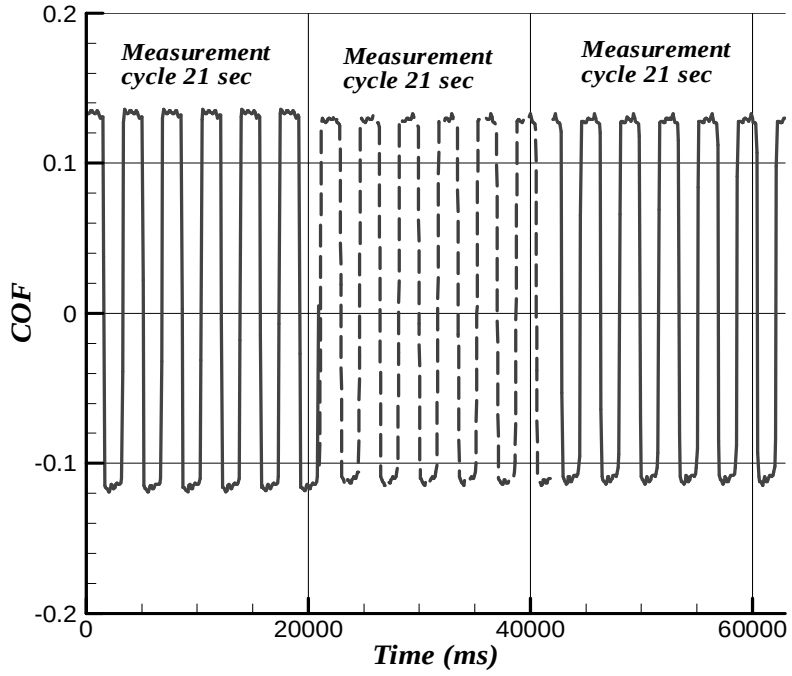

Figure 16. COF cyclic variation - production bushing.

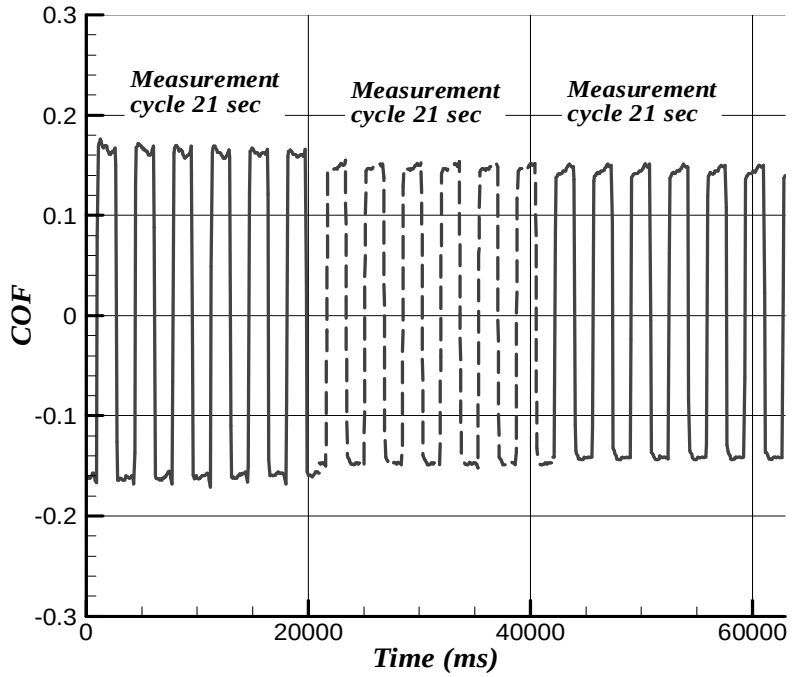

Figure 17. COF cyclic variation - plain bushing.

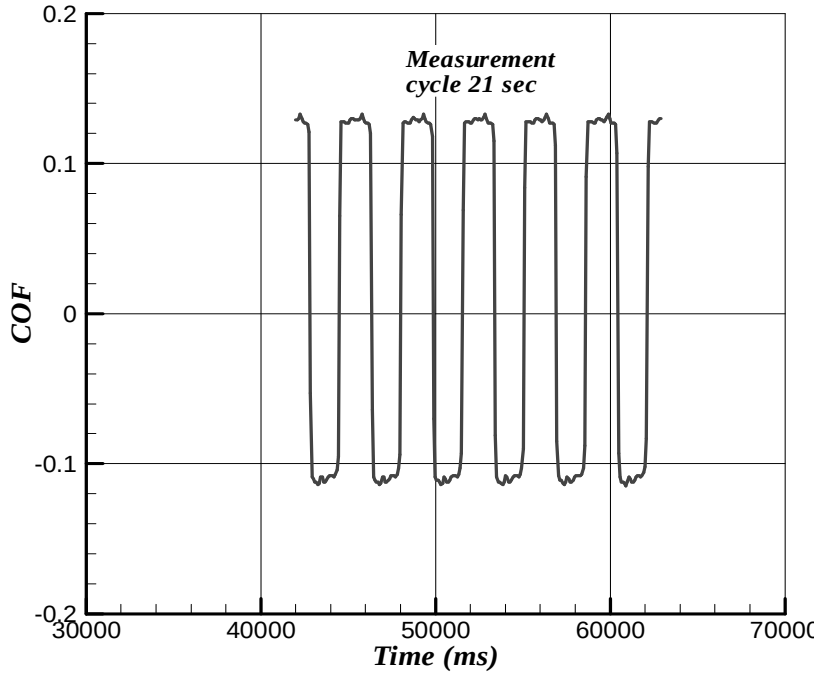

Figure 18. COF variation with direction of motion - production bushing.

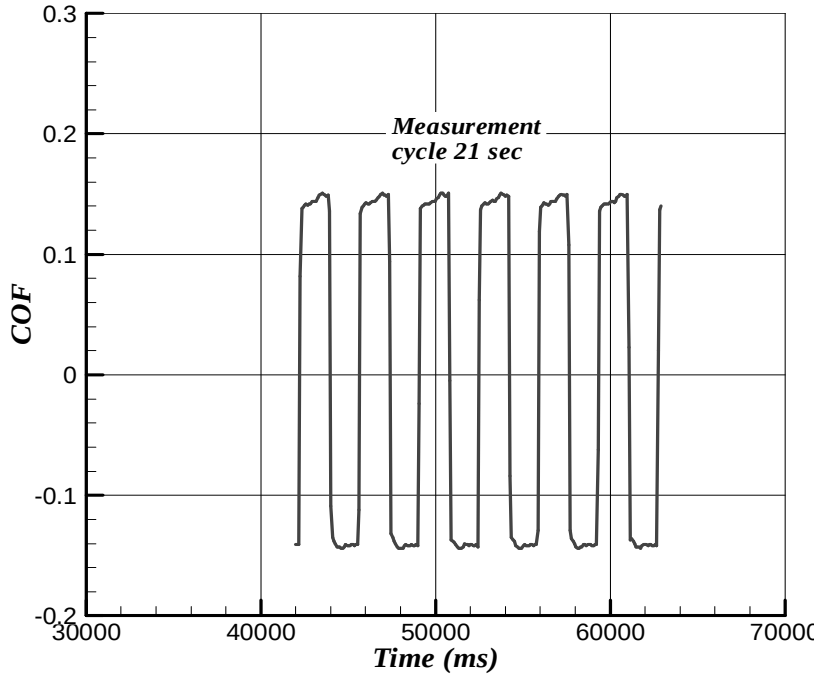

Figure 19. COF variation with direction of motion - plain bushing.

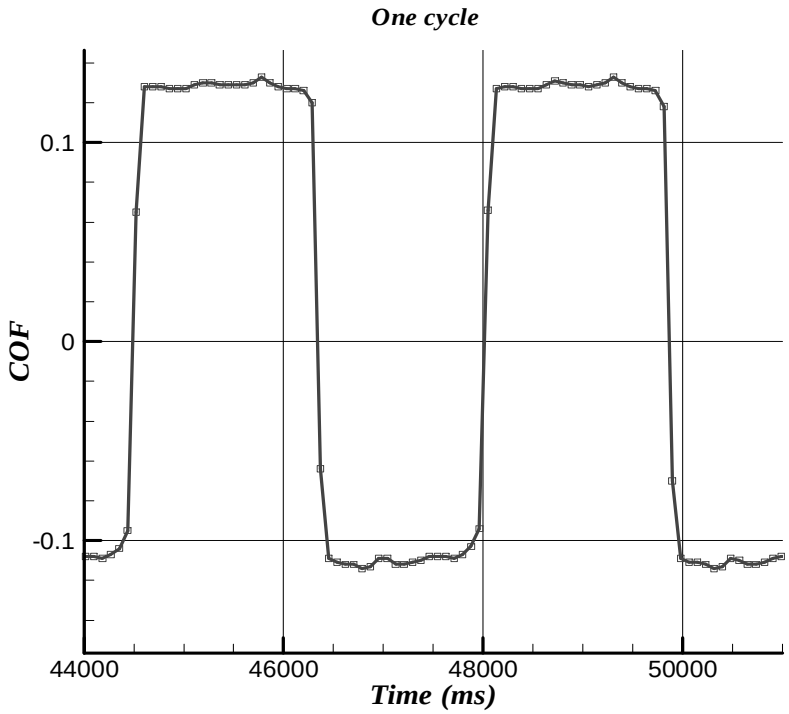

Figure 20. COF details over one cycle - production bushing.

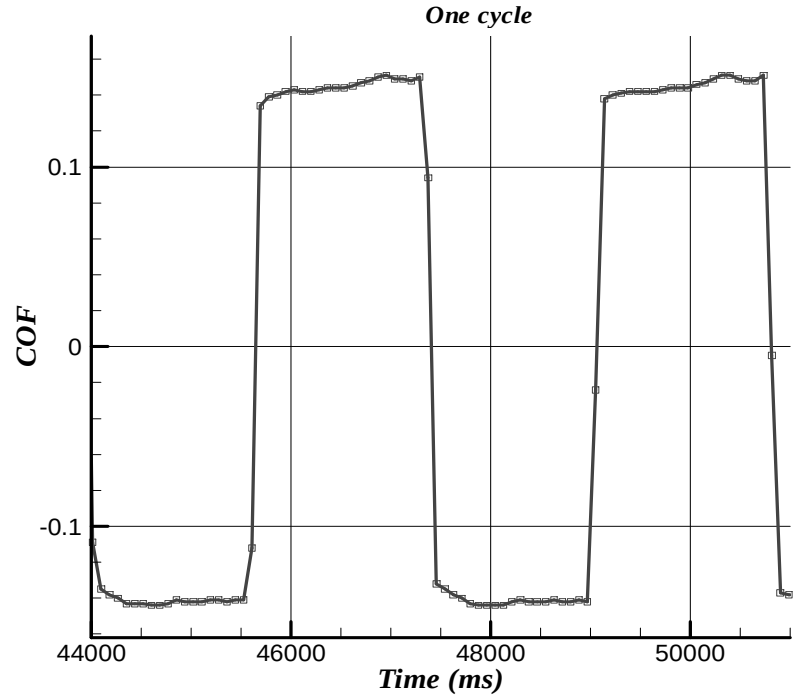

Figure 21. COF details over one cycle - plain bushing.

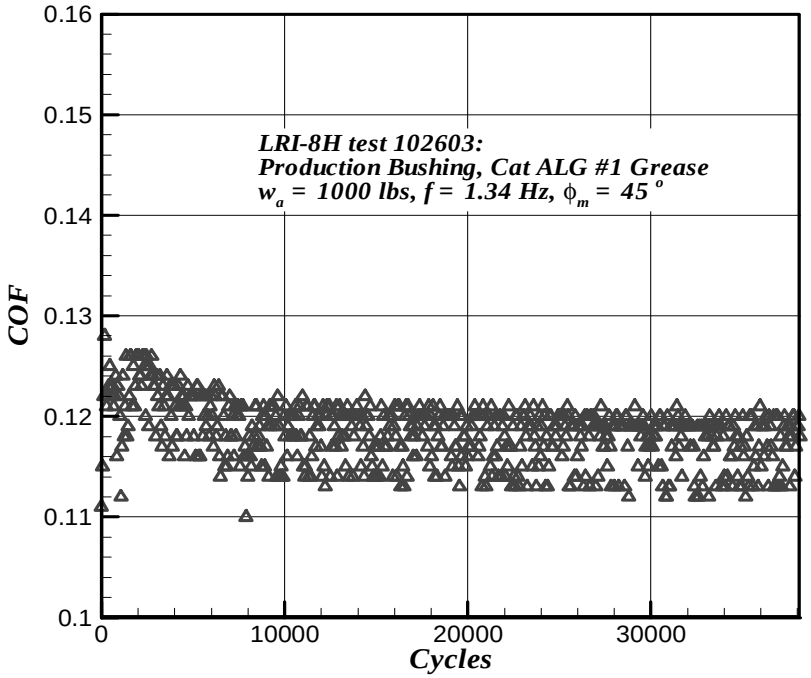

Figure 22. Scatter plot of the measured COF - production bushing

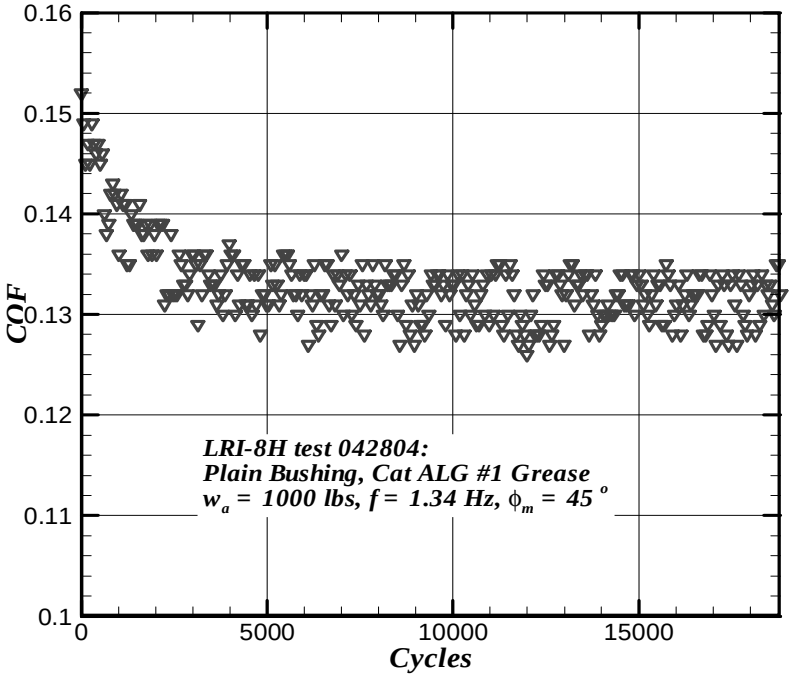

Figure 23. Scatter plot of the measured COF - plain bushing.

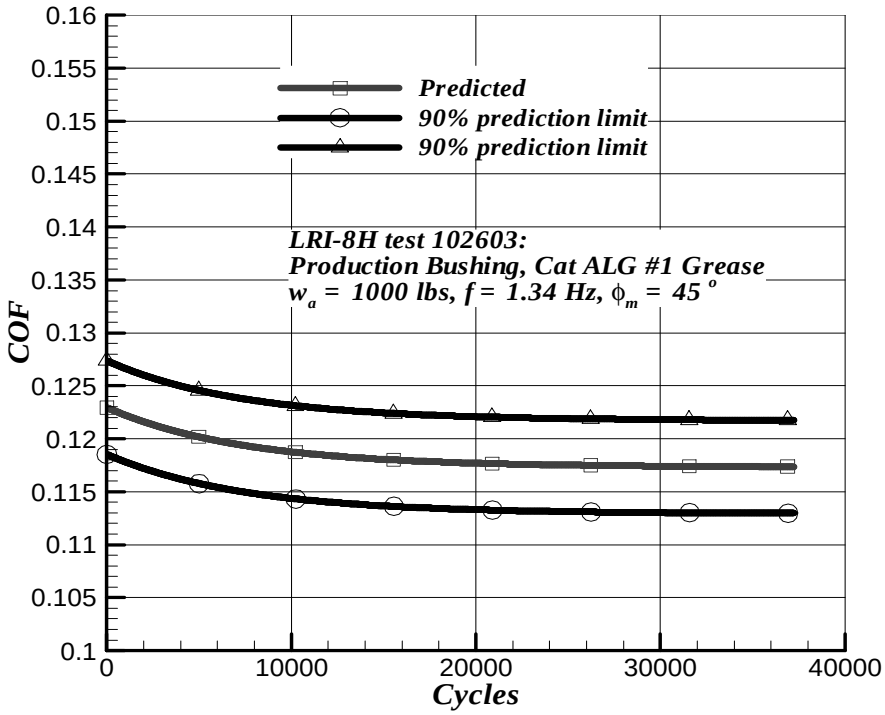

Figure 24. Curve fits of the COF - production bushing.

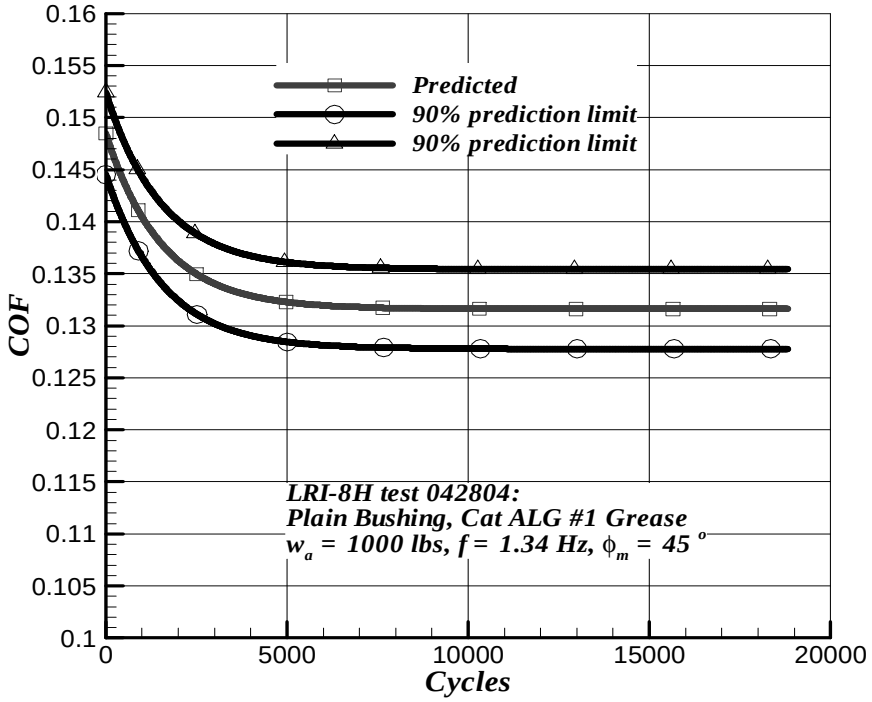

Figure 25. Curve fits of the COF - plain bushing.

Chapter 4. Thermal Model Description

A mathematical model is presented for the prediction of the surface temperature rise in a pair of contacting bodies that are sliding relative to one another. The model formulation is presented here for a general case, in dimensional form, and later applied to specific problems, in particular the pin-bushing joint. A dimensionless formulation is presented in the next Chapter. Appropriate solution technique will be presented too.

General Model Description and Assumptions

A schematic of a simple model describing contact and frictional heating between two sliding solids is displayed in Figure 26, along with the coordinate system. The tribo-system consists of two regions $\mathbb{R}_i$ of arbitrary geometry, bounded by surfaces $S_i = S_{ni} + S_c$, where $S_{ni},\ i = 1,2$ are the non-contacting portions of the boundary surfaces, and S_c is the common contact surface. The thermal material properties are k_i, c_i, ρ_i, and elastic material properties E_i, ν_i, α_i, where $i = 1,2$ for the stationary or moving region. The contact surface S_c, shared by both regions, consists of any number and distribution of contact patches or asperities. The contact area in the present model may be estimated from contact theory using available classical solutions, or numerically using conventional elasticity theory. The non-contacting portions of the boundary surfaces $S_{ni},\ i = 1,2$ are assumed to be subject to convective heat transfer and stress free boundary conditions. In the analytical treatment of contact problems, the coordinates are fixed to the center of the contact area, as shown, with the *z*-direction perpendicular to the contact area and pointing into the contacting bodies. Region $\mathbb{R}_2$ is stationary with respect to the contact area and the coordinate system $\left(x, y, z\right)$, while region $\mathbb{R}_1$ moves at a given velocity,

which can be either linear $v(t)$ in the *x*-direction as shown, or rotational about an axial direction. The configuration in Figure 6 may represent a number of applications, the simplest of which is a pin sliding back and forth on a flat or disk (which is often used in experimental wear tests), or the sliding contact of a cylinder in a bushing like in a dry bearing.

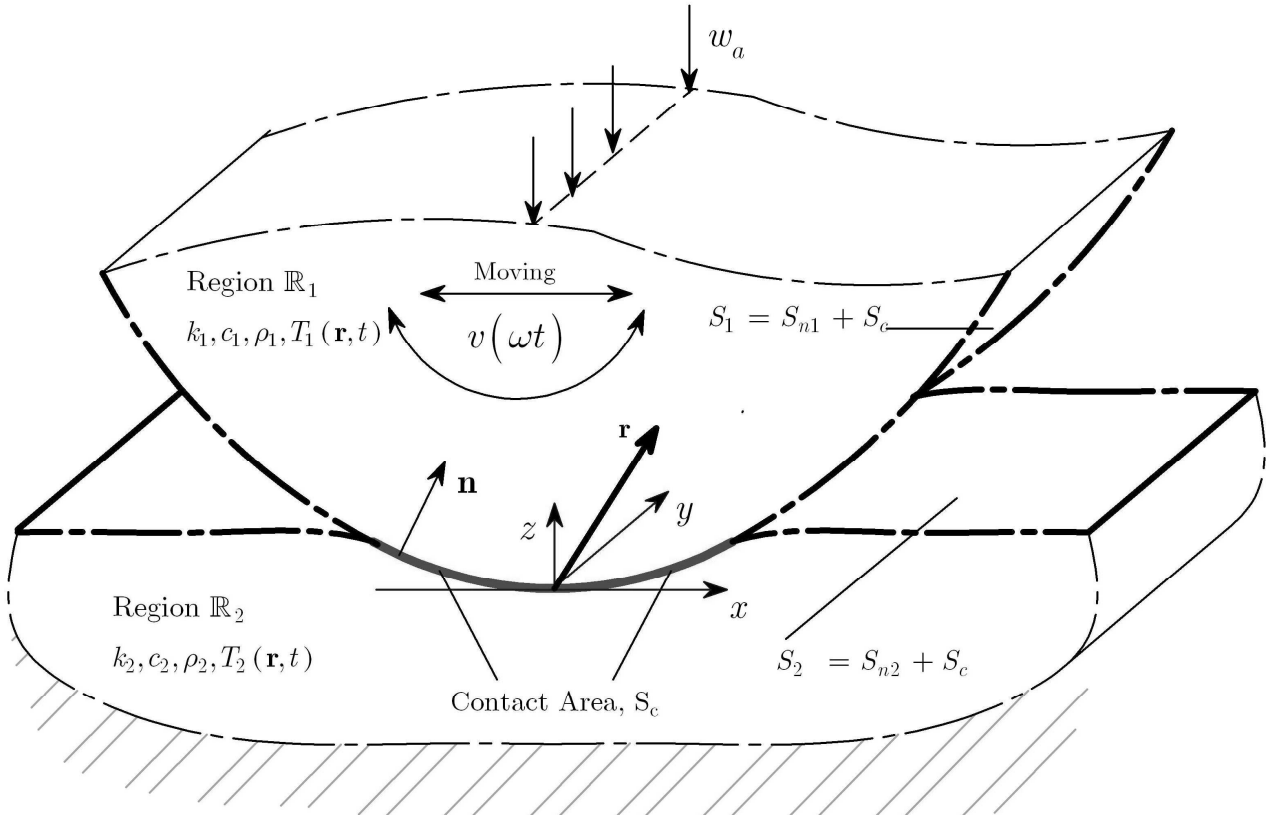

Figure 26. Schematic of the general model of two contacting bodies.

The velocity is an arbitrary time function. For instance, consider a rotational motion in the realm of a bearing with a shaft (pin) of radius r_s, rotating about its axis and sliding relative to a stationary journal surface. For oscillatory rotational motion with amplitude angle ϕ_{m} (radians), the position is given by $\phi(t) = \phi_0 + \phi_{\mathrm{m}}\Phi(\omega t)$, and the speed by $\dot{\phi}(t) = \phi_m \omega \dot{\Phi}(\omega t)$, $\dot{\Phi}(\omega t) = d\Phi / d(\omega t)$, where $\Phi(\omega t)$ is a periodic function of time, e.g.,

$\Phi(\omega t) = \sin(\omega t)$, or a triangular wave for constant speed, as illustrated in Figures 27-28. The corresponding linear motion is given by $s(t) = r_s \phi(t) = s_0 + s_{\mathrm{m}} \Phi(\omega t)$, and the linear velocity by $v(t) = \dot{s}(t) = v_{\mathrm{m}} \dot{\Phi}(\omega t)$, $v_{\mathrm{m}} = s_{\mathrm{m}} \omega$. For unidirectional rotational motion, the angular position is a saw-tooth time function of period 2π and amplitude is $\phi_{\mathrm{m}} = \pi/2$ radians for constant speed. The angular position is $\phi(t) = \phi_0 + \phi_{\mathrm{m}} (2\omega t/\pi) = \phi_0 + \phi_{\mathrm{m}} \Phi(\omega t)$, where $\Phi(\omega t) = 2\omega t/\pi$, $\dot{\Phi}(\omega t) = 2/\pi$ periodic over $0 \le \omega t \le 2\pi$, as shown in Figure 29.

In a real application, the above motion profiles may be combined in a particular manner for a specific process in order to accomplish a well defined sequence of events. Thus, the process may at different stages be moving or stationary depending on a given load cycle.

Governing Thermal Equations

The governing equation for temperature rise in region $\mathbb{R}_i$ reads

$$\rho_i c_i \frac{\partial T_i(\mathbf{r},t)}{\partial t} + \rho_i c_i m_i \mathbf{v}(t) \bullet \nabla T_i(\mathbf{r},t) = \nabla \bullet \left(k_i \nabla T_i(\mathbf{r},t) \right) :: \mathbf{r} \in \mathbb{R}_i,\ i = 1,2 \tag{1}$$

where $\mathbf{r} = (x,y,z)$ is the position vector, $\mathbf{v} = (v_x, v_y, v_z)$ is the velocity vector, $\nabla^2 = \dfrac{\partial}{\partial x^2} + \dfrac{\partial}{\partial y^2} + \dfrac{\partial}{\partial z^2}$, and $m_i = 1,0 :: i = 1,2$ (1 for the moving part, 0 for the stationary). The convective term in the heat equation for region $\mathbb{R}_i$ arises due to the motion relative to the fixed frame of reference. An initial condition is assumed where

$$T_i(\mathbf{r},0) = T_0(\mathbf{r}) :: \mathbf{r} \in \mathbb{R}_i,\ i = 1,2 \tag{2}$$

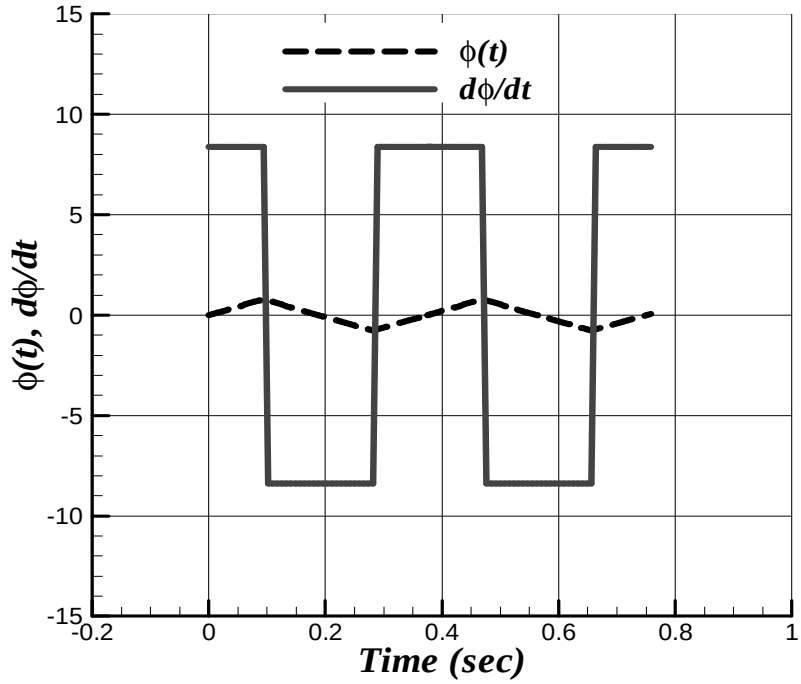

Figure 27. Oscillatory constant speed rotational motion profile.

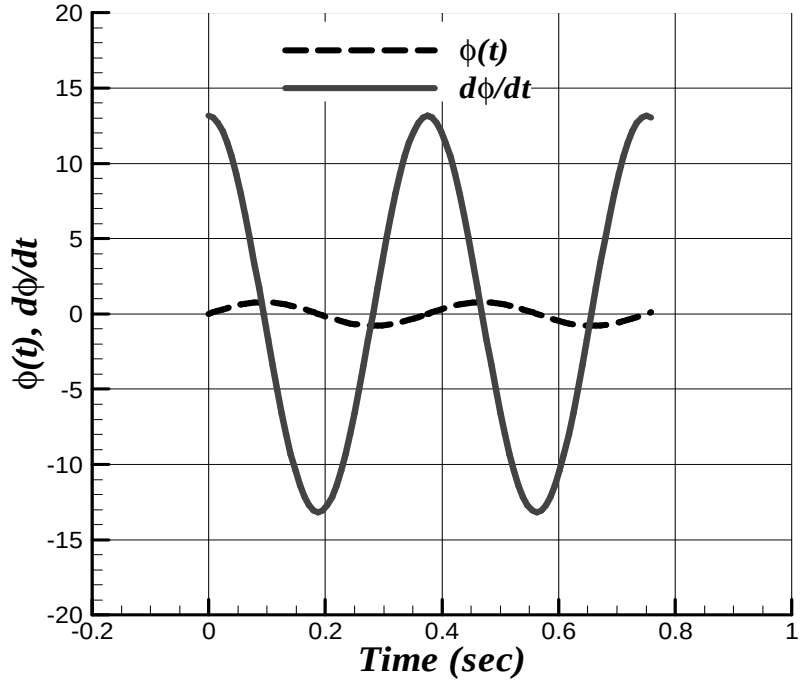

Figure 28. Oscillatory harmonic speed rotational motion profile.

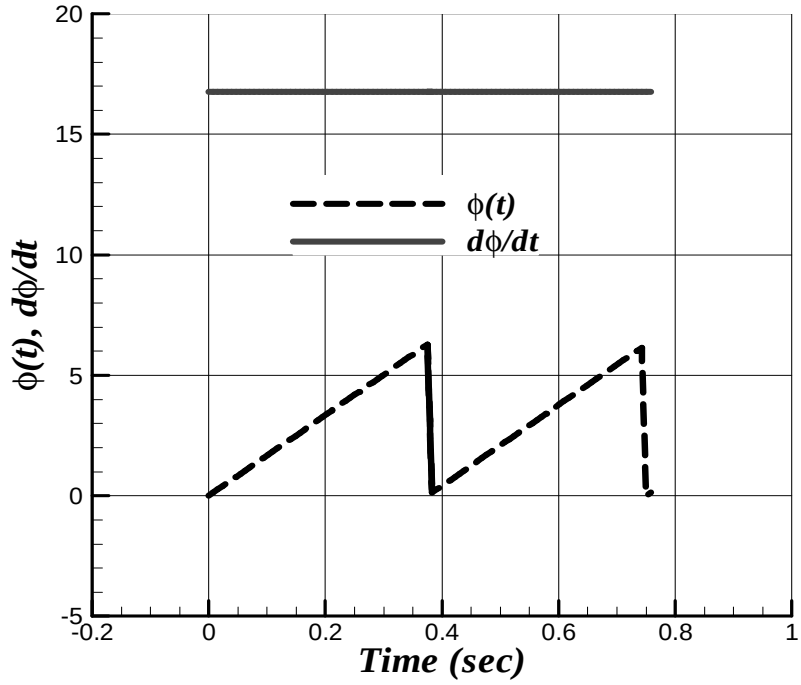

Figure 29. Unidirectional constant speed rotational motion profile.

Outside the contact region, the interface surfaces are assumed to be exposed to convective heat transfer conditions:

$$q_i\left(\mathbf{r},t\right) = -h_g \Delta T_g\left(\mathbf{r},t\right) :: \mathbf{r} \notin S_c,\ i = 1,2 \tag{3a}$$

$$\Delta T_g\left(\mathbf{r},t\right) = T_i\left(\mathbf{r},t\right) - T_j\left(\mathbf{r},t\right) :: i,j = 1,2 \tag{3b}$$

where $q_i = k_i\, \partial T_i \big/ \partial n$, and $\partial \big/ \partial n$ represents the gradient in the outward normal direction. A common interface outward normal direction is used for consistency of signs. The convection heat transfer coefficient $h_g\left(\mathbf{r},t\right)$ may vary along the boundary surface and with temperature. Coupling at the contact interface is established using continuity of the temperature and the conservation of heat flux. For perfect contact temperature continuity and energy balance must be enforced at the contact interface. For imperfect contact, there exists a jump in temperature between the two surfaces due to thermal contact resistance. Both of these conditions can be expressed mathematically as follows:

$$T_1(\mathbf{r},t) - T_2(\mathbf{r},t) = h_c\left[q_1(\mathbf{r},t) - q_2(\mathbf{r},t)\right] :: \mathbf{r} \in S_c. \tag{4}$$

$$\sum_{i=1}^{2} q_i(\mathbf{r},t) = q_c(\mathbf{r},t) :: \mathbf{r} \in S_c. \tag{5}$$

The frictional heat flux input $q_c(\mathbf{r},t)$ is defined below. For continuity at the contact interface, set $h_c = 0$, while for no-conduction across contact, $h_c = \infty$. For real contact, thermal contact resistance h_c has a finite range that may be determined using empirical rules [38]. The total heat flux input is related to the rate of mechanical work per unit area through frictional sliding and the contact pressure as follows:

$$q_c(\mathbf{r},t) = \mu_c p_c(\mathbf{r},t)\left|v(t)\right| \tag{6}$$

where μ_c is the coefficient of friction, $p_c(\mathbf{r},t)$ is the contact pressure distribution, and $v(t)$ is the relative linear sliding velocity.

In practice, a motion and load cycle may be prescribed where the velocity can vary from reciprocating to steady and even stationary, while the carried load may also follow a well defined sequence of events that consists in loading and unloading. During such events, the sliding interface undergoes periods of heating and cooling. This operating procedure directly influences the fluctuation of surface temperature rise. This can readily be implemented using a simulation procedure and will be considered in the analysis.

The partitioning of the frictional heat at the contact interface is a priori unknown. Extensive research and theories on heat flux division at the interface of contacting bodies have been reported in published literature, for instance [15], [28]-[32], but are limited to simple geometry not necessarily applicable to the pin-bushing conformal geometry. Typically, the heat flux division, at the interface of two contacting surfaces, is assumed to depend on their thermal conductivities and diffusivities [28]-[32]. When relative sliding occurs, the determination of the

partitioning factors is not well understood but has been discussed in [15] and [28]-[32]. In the present work, since the solution is sought in the entire domain including the interface, explicit knowledge of the heat flux division at the contact interface was not necessary for a solution to the boundary value problem. The material properties and the coupling conditions at the contact interface, which enforce continuity of the solution and the conservation of heat energy, will dictate how heat flux input is shared by the two contacting bodies. In other words, heat flux division is incorporated as part of the solution. Thus, the computational model can be used to study this aspect of the problem. It is customary to write the heat flux division in terms of ratios as follows:

$$\left|q_i\left(\mathbf{r},t\right)\right| = \lambda_i \left|q_c\left(\mathbf{r},t\right)\right|, \quad i = 1,2 \tag{7a}$$

where

$$0 < \lambda_i < 1\,,\ \lambda_1 + \lambda_2 = 1 \tag{7b}$$

From the above definitions,

$$\lambda_i = \left|\frac{q_i\left(\mathbf{r},t\right)}{q_c\left(\mathbf{r},t\right)}\right| = \left|\frac{k_i\,\partial T_i/\partial n}{q_c\left(\mathbf{r},t\right)}\right|, \quad i = 1,2\,. \tag{7c}$$

The distribution of heat flux partition is obtained once the temperature field is solved under the coupling conditions stated earlier. Clearly, the partitioning of the heat flux input has a direct influence on the surface temperature.

The contact pressure and contact area are not known in advance and must ordinarily be a part of the solution. This procedure is called thermal-mechanical coupling. For simplicity, the contact parameters are computed using a proper classical solution for which the contact pressure and extent are known. Thus, the total heat flux, $q_c\left(\mathbf{r},t\right)$, is known.

It is assumed that there is no misalignment in the original configuration along the axial direction, and that the contact pressure and extent are uniform in the axial direction. The material properties are assumed to be constant. These assumptions allow for a two-dimensional thermal analysis to be considered. A schematic of the general two-dimensional problem is shown in Figure 30, where the *z*-coordinate is in the axial direction and sliding is in the *x*-direction.

Axial thermal effects are averaged out by integrating the three-dimensional heat equation along the axial direction and considering the end boundary conditions. Convective end conditions are assumed to facilitate the formulation. Therefore, if the temperature field, $T\left(t,\mathbf{r}\right)$, is assumed to be a function of time and position, $\mathbf{r}=\left(x,y\right)$, in two-dimensional Cartesian coordinates, the averaged heat equation is augmented by an internal heat generation term, $q_b\left(\mathbf{r},T\right)$, that depends on the temperature distribution, and thermal and properties. Thus

$$\rho c\frac{\partial T}{\partial t}+m\rho c\mathbf{v}\bullet\nabla T=\nabla\bullet\left(k\nabla T\right)+q_b\left(\mathbf{r},T\right) \tag{8}$$

The term $q_b\left(\mathbf{r},T\right)$ is an internal heat source derived by integrating the three-dimensional heat transfer equation along the axial direction and taking into account the end-point boundary conditions, thus reducing the problem to a two-dimensional domain. This source term is expressed for each component as follows:

$$Lq_b\left(\mathbf{r},T\right)=\left[k\frac{\partial T}{\partial n}\right]_{-L/2}^{L/2} \tag{9a}$$

where L denotes the axial component length, which differs for different parts. If the endpoint boundary conditions of each component are described by convective conditions [33], then the expression for this source term turns out to be a function of the temperature as follows:

$$q_b\left(\mathbf{r},T\right)=-\left(2h_e/L\right)(T-T_e) \tag{9b}$$

The ambient temperature and heat transfer coefficient, (T_e, h_e), are assumed to be constant. The averaged heat equation and boundary conditions given above are applicable to any two-component system with sliding friction and arbitrary motion. The general formulation given above of the thermal problem and boundary conditions are illustrated in Figures 31 and 32 for two examples of sliding contact problems that are found in industry: the pin-on-flat and the pin-bushing systems. The former example is a simple application that has been reported extensively in the literature that deals with the prediction of surface temperature due to sliding friction. Some of the published work in the field relied on analytical methods, but much of it used numerical methods to simulate the problem. The latter of these applications is the focus of this research and will be considered in details.

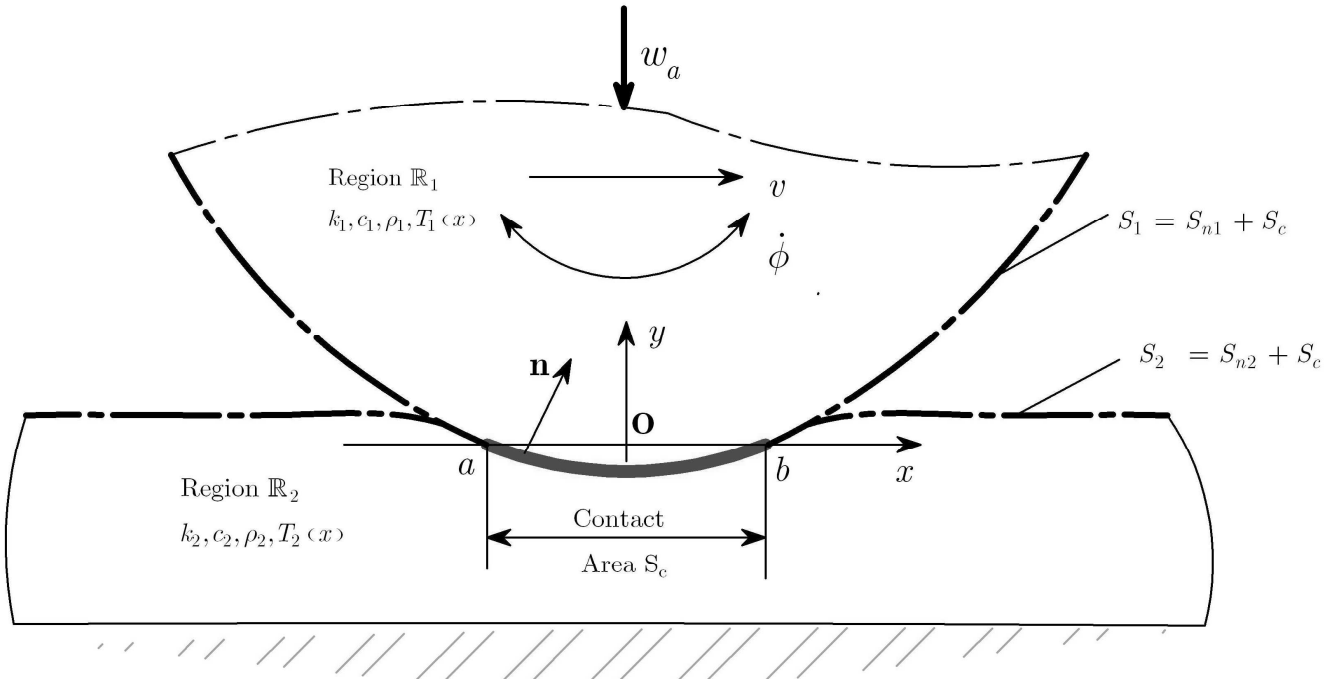

Figure 30. Schematic of the general two-dimensional problem.

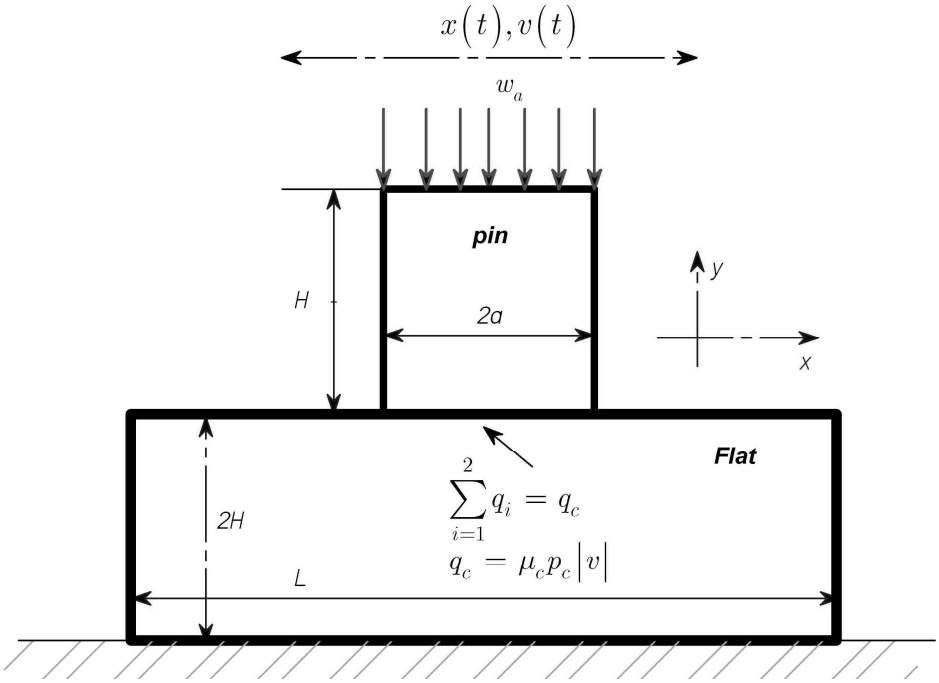

Figure 31. Pin-on-flat thermal problem.

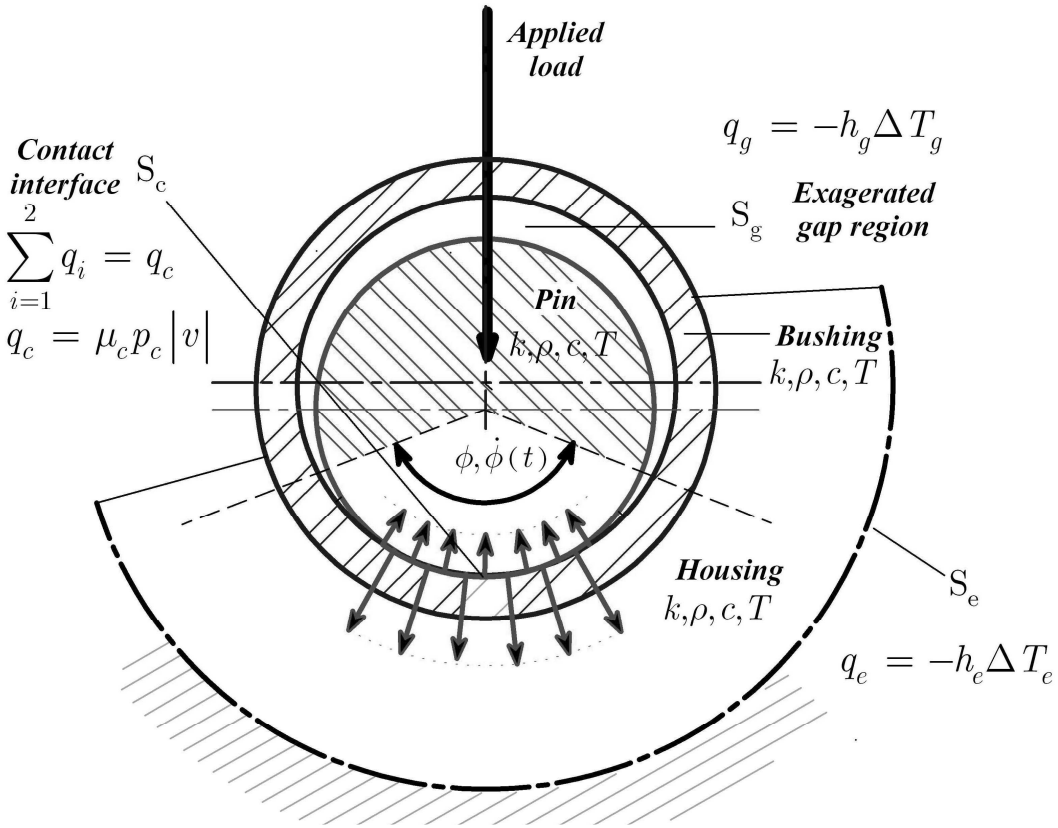

Figure 32. Pin-bushing thermal problem

Chapter 5 - Thermoelastic and Mechanical Problem

In this chapter coupled thermoelastic quazistatic linear elasticity equations and associated mechanical boundary conditions are considered. We begin with a general formulation, and then reduce it to the plane domain consistently with the averaged thermal model, described in the previous Chapter. The formulation of the thermoelastic and mechanical problem is necessary in order to account for thermal expansion, and introduce the concept of thermomechanical coupling.

General Thermoelasticity Equations

The displacement, stress and strain vectors in Cartesian coordinates are expressed by

$$\{u\} = \begin{bmatrix} u_x & u_y & u_z \end{bmatrix}^T \tag{10a}$$

$$\{\sigma\} = \begin{bmatrix} \sigma_{xx} & \sigma_{yy} & \sigma_{zz} & \tau_{xy} & \tau_{xz} & \tau_{yz} \end{bmatrix}^T \tag{10b}$$

$$\{\varepsilon\} = \begin{bmatrix} \varepsilon_{xx} & \varepsilon_{yy} & \varepsilon_{zz} & \gamma_{xy} & \gamma_{xz} & \gamma_{yz} \end{bmatrix}^T \tag{10c}$$

Engineering shear strain is used in the elastic material definitions. Thus,

$$\begin{aligned} 2\varepsilon_{mn} &= \left(u_{m,n} + u_{n,m}\right) :: m = n \\ &\quad , \; m,n = x,y,z \\ \gamma_{mn} &= \left(u_{m,n} + u_{n,m}\right) :: m \neq n \end{aligned} \tag{10d}$$

Linear thermal expansion for an isotropic material, due to a temperature change, produces thermal strains [34]

$$\{\varepsilon_T\} = \left(\alpha_e \Delta T\right)\{\mathbf{I}\}, \quad \{\mathbf{I}\} = \begin{bmatrix} 1 & 1 & 1 & 0 & 0 & 0 \end{bmatrix}^T \tag{10e}$$

In the above equations, α_e is the coefficient of linear thermal expansion (assumed constant), and ΔT is the temperature rise. Since thermal expansion is identical in all directions for an isotropic medium, only normal strains and no shearing strains arise. The stress-strain-temperature relations may be written in matrix as follows [34]:

$$\{\boldsymbol{\sigma}\} = [\mathbf{E}](\{\varepsilon\} - \{\varepsilon_T\}) \tag{11a}$$

where the elasticity matrix is given by [35]

$$[\mathbf{E}] = \begin{bmatrix} (1-\nu)c & \nu & \nu & 0 & 0 & 0 \\ \nu & (1-\nu)c & \nu & 0 & 0 & 0 \\ \nu & \nu & (1-\nu)c & 0 & 0 & 0 \\ 0 & 0 & 0 & G & 0 & 0 \\ 0 & 0 & 0 & 0 & G & 0 \\ 0 & 0 & 0 & 0 & 0 & G \end{bmatrix} \tag{11b}$$

$$c = \frac{E}{(1+\nu)(1-2\nu)},\ G = \frac{E}{2(1+\nu)} \tag{11c}$$

The inverse form reads:

$$\{\varepsilon\} = [\mathbf{C}]\{\boldsymbol{\sigma}\} + \{\varepsilon_T\} \tag{11d}$$

$$[\mathbf{C}] = [\mathbf{E}]^{-1} = \frac{1}{E}\begin{bmatrix} 1 & -\nu & -\nu & 0 & 0 & 0 \\ -\nu & 1 & -\nu & 0 & 0 & 0 \\ -\nu & -\nu & 1 & 0 & 0 & 0 \\ 0 & 0 & 0 & E/G & 0 & 0 \\ 0 & 0 & 0 & 0 & E/G & 0 \\ 0 & 0 & 0 & 0 & 0 & E/G \end{bmatrix} \tag{11e}$$

The relation given by Equation (11-d, e) is the **standard form** used in linear elasticity for an isotropic material (E, ν).

The strain-displacement relations for isotropic elasticity are:

$$\{\varepsilon\} = [\partial]\{\mathbf{u}\} :: [\partial] = \begin{bmatrix} \partial/\partial x & 0 & 0 \\ 0 & \partial/\partial y & 0 \\ 0 & 0 & \partial/\partial z \\ \partial/\partial y & \partial/\partial x & 0 \\ \partial/\partial z & 0 & \partial/\partial x \\ 0 & \partial/\partial z & \partial/\partial y \end{bmatrix}, \tag{12}$$

The equilibrium equations, assuming quasi-static elasticity, are typically written as follows:

$$[\partial]^T [\sigma] + \rho\{f\} = \{0\} \tag{13a}$$

where the external force (per unit mass) vector is denoted by $\{f\} = \begin{bmatrix} f_x & f_y & f_z \end{bmatrix}^T$.

The quasi-static displacement equations are obtained by substituting the stress-strain-temperature relations into the equilibrium equations.

$$[\partial]^T [\mathbf{E}](\{\varepsilon\} - \{\varepsilon_T\}) + \rho\{\mathbf{f}\} = 0 \tag{13b}$$

$$[\partial]^T [\mathbf{E}]([\partial]\{u\} - (\alpha_e \Delta T)\{\mathbf{I}\}) + \rho\{\mathbf{f}\} = 0 \tag{13c}$$

Boundary conditions for the mechanical problem are either Dirichlet type (displacement boundary conditions) or Neumann type (load boundary conditions):

$$u_i = d_i(\mathbf{r}, t) :: \text{on } \partial\mathbb{R},\ i = x, y, z \tag{14}$$

$$\sigma_{ij} n_j = S_i(\mathbf{r}, t) :: \text{on } \partial\mathbb{R},\ i, j = x, y, z \tag{15}$$

In the case of frictional contact, the traction $S_i(\mathbf{r}, t)$ represents the contact pressure $p_c(\mathbf{r}, t)$ in the normal direction to the contact interface, and shear stress in the tangential direction. In the case of sliding, the shear traction may be assumed to follow the coulomb

friction law, $\mu_c p_c(\mathbf{r},t)$, and the condition for sliding becomes: $\sigma_{ij} n_j \le \mu_c p_c(\mathbf{r},t)$. Since the thermal problem was reduced to two-dimensions, plane thermoelasticity equations will be considered.

Plane Thermoelasticity Equations

Plane-strain or plane-stress may apply depending on the situation. Plane strain prevails for long prismatic bodies in the axial direction when the *z*-axis is strain-free [35]. Thus,

$$u_m = u_m(x,y) :: m \equiv x,y\,,\; u_z = 0 \tag{17a}$$

Therefore,

$$\gamma_{xz} = \gamma_{yz} = \varepsilon_{zz} = 0 :: \text{zero } z\text{-strain.} \tag{17b}$$

$$\tau_{xz} = \tau_{yz} = 0 :: \text{zero } z\text{-shear stress} \tag{17c}$$

A plane stress state prevails in thin prismatic bodies (small thickness in the axial direction) and is defined by the following conditions:

$$\tau_{xz} = \tau_{yz} = \sigma_{zz} = 0 :: \text{zero } z\text{-stress.} \tag{17d}$$

$$\gamma_{xz} = \gamma_{yz} = 0 :: \text{zero } z\text{-shear strain} \tag{17e}$$

The displacement, stress, strain and force vectors reduce to:

$$\{u\} = \begin{bmatrix} u_x & u_y \end{bmatrix}^T \tag{18a}$$

$$\{\sigma\} = \begin{bmatrix} \sigma_{xx} & \sigma_{yy} & \tau_{xy} \end{bmatrix}^T \tag{18b}$$

$$\{\varepsilon\} = \begin{bmatrix} \varepsilon_{xx} & \varepsilon_{yy} & \gamma_{xy} \end{bmatrix}^T \tag{18c}$$

$$\{\varepsilon_T\} = (\alpha_e \Delta T)\{\mathbf{I}\}, \{\mathbf{I}\} = \begin{bmatrix} 1 & 1 & 0 \end{bmatrix}^T \tag{18d}$$

$$\left\{f\right\} = \begin{bmatrix} f_x & f_y \end{bmatrix}^T \tag{18e}$$

In either case, the stress-strain-temperature relations for plane isotropic elasticity are obtained by imposing the above conditions on the three-dimensional relations. Thus, for plane stress the stress-strain-temperature relations are:

$$\begin{Bmatrix} \sigma_{xx} \\ \sigma_{yy} \\ \tau_{xy} \end{Bmatrix} = \left[\mathbf{E}\right]\left\{\begin{Bmatrix} \varepsilon_{xx} \\ \varepsilon_{yy} \\ \gamma_{xy} \end{Bmatrix} - \begin{Bmatrix} 1 \\ 1 \\ 0 \end{Bmatrix}\alpha_e \Delta T\right\}, \left[\mathbf{E}\right] = \begin{bmatrix} (1-\nu)c & \nu & 0 \\ \nu & (1-\nu)c & 0 \\ 0 & 0 & G \end{bmatrix} \tag{19}$$

$$\begin{Bmatrix} \varepsilon_{xx} \\ \varepsilon_{yy} \\ \gamma_{xy} \end{Bmatrix} = \left[\mathbf{C}\right]\begin{Bmatrix} \sigma_{xx} \\ \sigma_{yy} \\ \tau_{xy} \end{Bmatrix} + \begin{Bmatrix} 1 \\ 1 \\ 0 \end{Bmatrix}\alpha_e \Delta T, \left[\mathbf{C}\right] = \left[\mathbf{E}\right]^{-1} = \frac{1}{E}\begin{bmatrix} 1 & -\nu & 0 \\ -\nu & 1 & 0 \\ 0 & 0 & E/G \end{bmatrix} \tag{20}$$

For plane strain we obtain the stress-strain-temperature relations by imposing the above conditions, or alternatively by making the following substitutions for E, ν, α_e in Equations (19)-(20):

$$E_1 = \frac{E}{1-\nu^2}, \quad \nu_1 = \frac{\nu}{1-\nu}, \quad \alpha_{e1} = \alpha_e(1+\nu) \tag{21}$$

Therefore,

$$\begin{Bmatrix} \sigma_{xx} \\ \sigma_{yy} \\ \tau_{xy} \end{Bmatrix} = \left[\mathbf{E}\right]\left\{\begin{Bmatrix} \varepsilon_{xx} \\ \varepsilon_{yy} \\ \gamma_{xy} \end{Bmatrix} - \begin{Bmatrix} 1 \\ 1 \\ 0 \end{Bmatrix}(1+\nu)\alpha_e \Delta T\right\}, \left[\mathbf{E}\right] = \begin{bmatrix} (1-\nu_1)c_1 & \nu_1 & 0 \\ \nu_1 & (1-\nu_1)c_1 & 0 \\ 0 & 0 & G_1 \end{bmatrix} \tag{22}$$

$$\begin{Bmatrix} \varepsilon_{xx} \\ \varepsilon_{yy} \\ \gamma_{xy} \end{Bmatrix} = \left[\mathbf{C}\right]\begin{Bmatrix} \sigma_{xx} \\ \sigma_{yy} \\ \tau_{xy} \end{Bmatrix} + \begin{Bmatrix} 1 \\ 1 \\ 0 \end{Bmatrix}(1+\nu)\alpha_e \Delta T, \left[\mathbf{C}\right] = \left[\mathbf{E}\right]^{-1} = \frac{1}{E_1}\begin{bmatrix} 1 & -\nu_1 & 0 \\ -\nu_1 & 1 & 0 \\ 0 & 0 & E_1/G_1 \end{bmatrix} \tag{23}$$

$$c_1 = \frac{E_1}{(1+\nu_1)(1-2\nu_1)}, \; G_1 = \frac{E_1}{2(1+\nu_1)} \tag{24}$$

The strain-displacement relations become:

$$\{\varepsilon\} = [\partial]\{\mathbf{u}\}, [\partial] = \begin{bmatrix} \partial/\partial x & 0 \\ 0 & \partial/\partial y \\ \partial/\partial y & \partial/\partial x \end{bmatrix} \tag{25a}$$

The equilibrium equations in 2D are typically the same as given before. In matrix form they read:

$$[\partial]^T [\sigma] + \rho\{f\} = \{0\} \tag{25a}$$

$$[\partial]^T [\mathbf{E}]\left(\{\varepsilon\} - \{\varepsilon_T\}\right) + \rho\{\mathbf{f}\} = 0 \tag{25b}$$

$$[\partial]^T [\mathbf{E}]\left([\partial]\{u\} - (\alpha_e \Delta T)\{\mathbf{I}\}\right) + \rho\{\mathbf{f}\} = 0 \tag{25c}$$

Boundary conditions for the mechanical problem are either Dirichlet type (displacement boundary conditions) or Neumann type (load boundary conditions):

$$u_i = d_i(t,x) :: \text{on } \partial\mathbb{R}, \; i = x, y \tag{26}$$

$$\sigma_{ij} n_j = S_i(t,x,y) :: \text{on } \partial\mathbb{R}, \; i, j = x, y \tag{27}$$

In the case of a frictional contact the traction $S_i(t,x)$ represents the contact pressure $p_c(t,x)$ in the normal direction to the contact interface, and shear stress in the tangential direction. At the onset of sliding, if the shear traction is assumed to follow the coulomb friction law, $\mu_c p_c(t,x)$, then the condition for sliding becomes: $\sigma_{ij} n_j \leq \mu_c p_c(t,x)$. At the contact interface, the following mechanical boundary conditions are assumed for frictional sliding:

$$\sigma_{z1} = \sigma_{z2} = p_c :: \text{on } S_c \tag{28a}$$

$$\tau_{xzi} = \mu p_c :: \text{on } S_c, \; i = 1,2 \tag{28b}$$

$$\sigma_{zi} = \tau_{xzi} = \tau_{yzi} = 0 :: \text{on } S_{nc}, \; i = 1,2 \tag{28c}$$

The stationary body, region $\mathbb{R}_2$ (see Figure 33), is constrained rigidly on the bottom surface. That is, no displacements are allowed there. An external load is applied at the contacting body, region $\mathbb{R}_1$, to keep it in contact with the flat. The external load is balanced with reaction forces at the contact interface. The contact pressure and frictional shear stresses at the sliding contact generate frictional heat. All other boundaries may be assumed to be stress-free. Figures 34 and 35 present two particular cases of sliding contact.

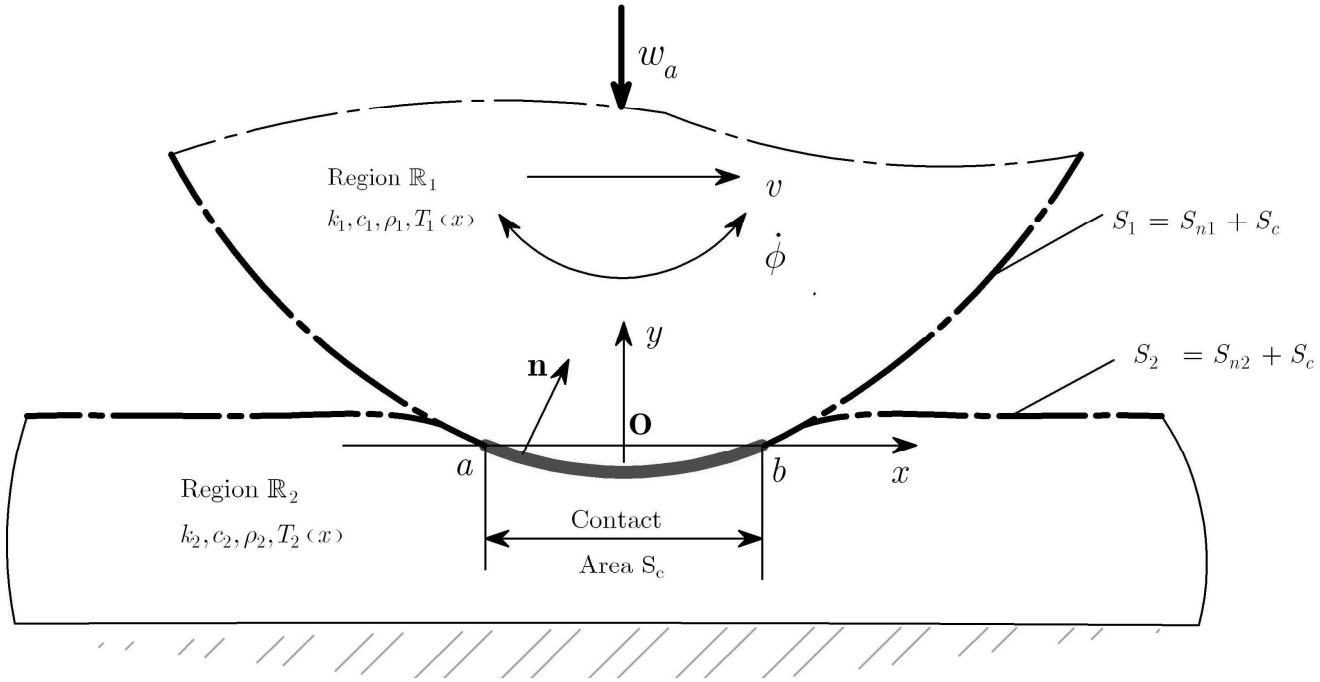

Figure 33. Mechanical boundary conditions

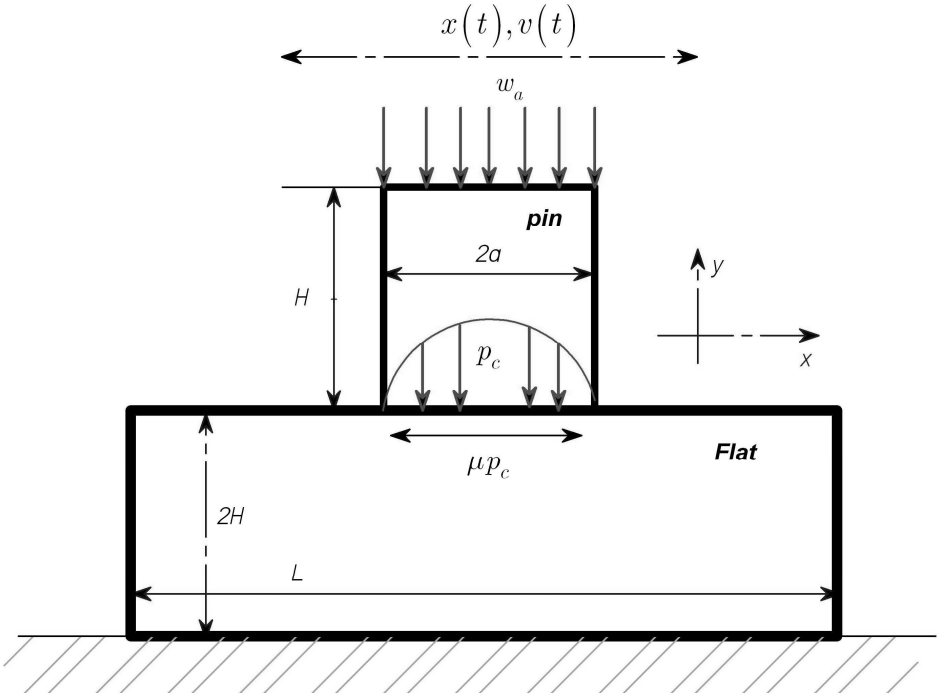

Figure 34. Pin-on-flat mechanical problem

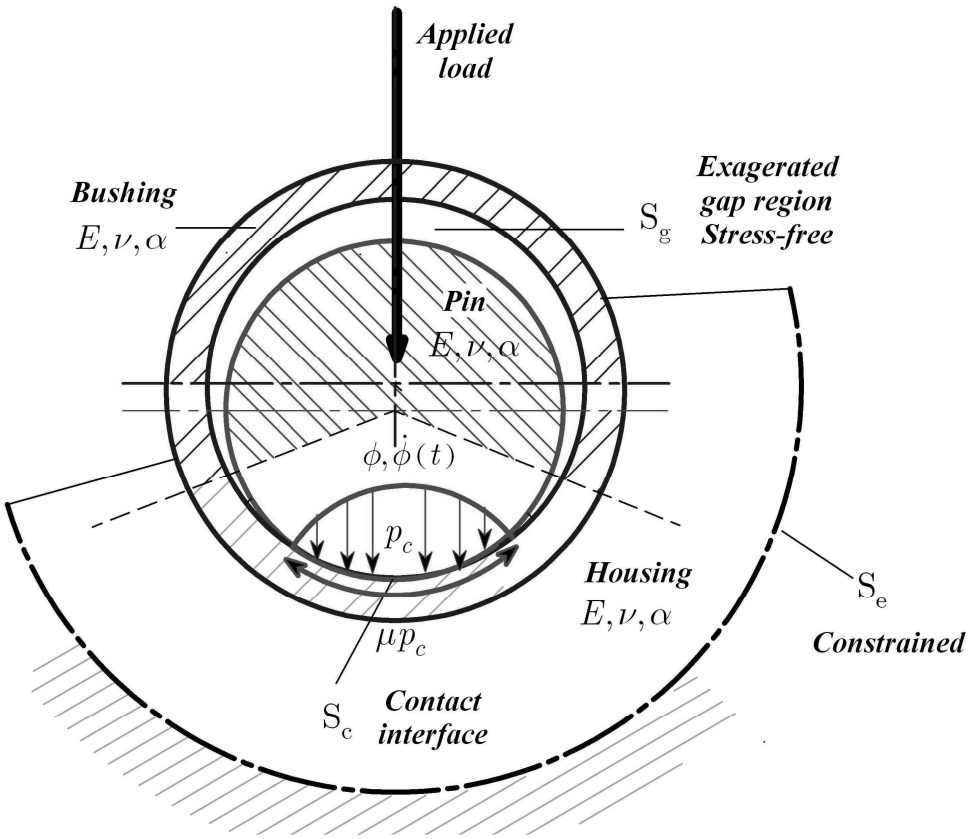

Figure 35. Pin-bushing mechanical problem

Chapter 6 – Dimensionless Equations

Since the physical thermal problem involves four independent dimensions, *length*, *time*, *temperature*, and *power*, it is convenient to nondimensionalize the problem. Four reference quantities are needed to render the problem dimensionless.

Dimensional Analysis

Using an order of magnitude analysis on the basic variables in the thermal problem, we may approximate the basic heat equation as follows:

$$k\left(\frac{\partial^2 T}{\partial x^2}+\frac{\partial^2 T}{\partial y^2}\right)=\rho c\frac{\partial T}{\partial t}+m\rho cv\frac{\partial T}{\partial x}\sim k\left(\frac{\delta T}{\delta_x^2}+\frac{\delta T}{\delta_y^2}\right)\simeq \rho c\frac{\delta T}{t}+m\rho cv\frac{\delta T}{\delta_x}$$

where the partial differentials have been approximated by finite values: $\partial x \simeq \delta_x$, $\partial y \simeq \delta_y$ for space, t for time, and $\partial T \simeq \delta T$ for temperature. Assume further that $\delta_x, \delta_y \sim \delta$. Substituting into the above equation leads to:

$$\frac{1}{\delta^2}\sim\frac{1}{\kappa}\frac{1}{t}+\frac{1}{\kappa}\frac{v}{\delta},\ \kappa=k\Big/\rho c$$

In the limit considering steady and initial conditions, we may obtain reference scales for time and space as follows:

$$\lim_{t\to\infty}\frac{1}{\delta^2}\sim\frac{1}{\kappa}\frac{v}{\delta}\Rightarrow\delta\sim\frac{\kappa}{v},$$

$$\lim_{t\to 0}\frac{1}{\delta^2}\sim\frac{1}{\kappa}\frac{1}{t}\Rightarrow t\sim\frac{\delta}{v}=\frac{\kappa}{v^2}$$

In order to get a reference value for the temperature rise, consider the boundary condition at the contact interface:

$$q_s = \sum_i q_i = \sum_i \left(-1\right)^i k_i \frac{\partial T_i}{\partial n} \Rightarrow k\frac{\delta T}{\delta} \sim q \Rightarrow \delta T \sim \frac{q}{k/\delta} = \frac{q}{h}$$

The above scale analysis provides a rough idea of how to nondimensionalize the thermal equations in rectangular coordinates. However, it does not offer the only or most suitable reference quantities. We will choose the thermal properties, $\rho_r, c_r, k_r, \kappa_r$, characteristic speed v_r associated with the moving body. The characteristic velocity will be taken as the maximum velocity value. The characteristic pressure will be defined as the mean pressure. The characteristic heat flux is defined as the product of the above characteristic velocity and pressure, $q_r = p_r v_r$. A reference heat transfer coefficient is defined based on the above scale analysis as $h_r = k_r/s_r$, where s_r is the characteristic length. The characteristic temperature is defined in terms of these reference parameters. In the following sections, the thermal and thermoelastic equations and boundary conditions are nondimensionalized in a general manner and the subscript "*r*" indicates a reference value. Reference parameters will be defined more explicitly specifically for the particular applications considered.

Dimensionless Thermal Equations

To normalize the problem, we define the dimensionless time and space variables conveniently as follows:

$$t = t_r \tau\,,\; x, y, z = s_r\left(X,\;\; Y,\;\; Z\right) \tag{29}$$

where t_r is a reference time and s_r is a characteristic length, both of which must be chosen for the specific application geometry and operating conditions. The resulting reference linear speed may be derived from the above transformation, and will be denoted $v_r = s_r/t_r$. The dimensionless sliding velocity is given by:

$$V(\tau) = v/v_r \tag{30}$$

The contact pressure is normalized with respect to the apparent pressure (projected load), while the reference heat flux is defined in terms of the reference values of velocity and contact pressure. Thus,

$$p_c = p_r P_c \tag{31}$$

$$q_c = q_r Q_c,\ q_r = p_r v_r \tag{32}$$

The dimensionless temperature rise is defined as:

$$\Delta T = T_r \Theta,\ T_r = q_r/h_r \tag{33}$$

The dimensionless boundary condition at the sliding interface reads:

$$K\frac{\partial \Theta}{\partial n} + B_i \Delta\Theta = B_{ir} Q \ :: \text{on } \boldsymbol{S}_{\mathrm{c}} \cup \boldsymbol{S}_{\mathrm{g}} \tag{34}$$

$$K = k/k_r,\ B_i = hs_r/k_r,\ B_{ir} = h_r s_r/k_r \tag{35}$$

where the reference thermal conductivity is that of the moving part, and the reference heat transfer coefficient is chosen as that of the surroundings. The dimensionless heating and cooling fluxes at the interface are described by:

$$Q = \begin{cases} Q_c & \text{on } S_c \\ 0 & Otherwise \end{cases},\ B_i = \begin{cases} 0 & \text{on } S_c \\ Bi_g & Otherwise \end{cases} \tag{36a}$$

$$Q_c = q_c/q_r = \mu_c P_c \left|V(\tau)\right|,\ Bi_g = h_g s_r/k_r \tag{36b}$$

The heat equation in dimensionless form is:

$$P_e \frac{K}{\Lambda}\frac{\partial \Theta}{\partial \tau} + mP_e \frac{K}{\Lambda} V(\tau)\frac{\partial \Theta}{\partial \theta} = \nabla\bullet\left(K\nabla\Theta\right) + B_{ie} Q_b \tag{37}$$

where

$$Q_b = \frac{s_r q_b}{q_r} = -\frac{2h_r s_r}{L q_r}\Delta T = -\frac{2s_r}{L}\Theta \tag{38}$$

$$\Lambda = \kappa \big/ \kappa_r \,,\; P_e = {s_r}^2 \omega \big/ \kappa_r \tag{39}$$

The dimensionless cooling boundary condition at the outer surface is

$$K\frac{\partial \Theta}{\partial n} + B_{ie}\Theta = 0 \;::\; \text{on } \mathrm{S_e} \tag{40}$$

The formulation given above reveals the appropriate dimensionless parameters that must be defined for a numerical solution of the thermal problem. Note that the coefficients of the dimensionless heat equation in the above form (37) may be rewritten in standard form:

$$K_e \nabla^2 \Theta + B_{ir} Q_b = D_e C_e \Theta_{,\tau} + m D_e C_e V\left(\tau\right)\Theta_{,X} \tag{41a}$$

where

$$K_e = K \,,\; D_e C_e = K P_e \big/ \Lambda \tag{41b}$$

To determine the equivalent density and heat capacity, we define the numerical proportionality ratio $\zeta = \rho \big/ c$, and impose the condition $D_e \big/ C_e = \zeta$, which physically enforces a proportionality condition between the density and heat capacity. Solving the two equations, we obtain:

$$C_e = \sqrt{K P_e \big/ \Lambda} \Big/ \sqrt{\zeta} \,,\; D_e = \sqrt{K P_e \big/ \Lambda}\sqrt{\zeta} \,. \tag{41c}$$

The thermal problem in its dimensionless standard form (41) may be solved with these equivalent dimensionless material properties.

Dimensionless Thermoelasticity Equations

To nondimensionalize the stress-strain-temperature relations, the normalized stress is defined with respect to the apparent pressure (here the projected load $p_r = p_l$) as

$$\left[\boldsymbol{\Sigma}\right] = p_r\left[\sigma\right] = p_r\left[\mathbf{E}\right]\left(\left[\varepsilon\right] - \left[\varepsilon_T\right]\right) \tag{42}$$

Recalling that: $\left\{\varepsilon_T\right\} = \left(\alpha_e \Delta T\right)\left\{\mathbf{I}\right\}$, $\Theta = \left(h_r / q_r\right)\Delta T$, and applying this to the stress-strain relations, we have

$$\left[\boldsymbol{\Sigma}\right] = p_r\left[\mathbf{E}\right]\left(\left[\varepsilon\right] - \left(\alpha_e \Delta T\right)\mathbf{I}\right) \Rightarrow \left[\boldsymbol{\Sigma}\right] = \left[\mathbf{E}'\right]\left(\left[\varepsilon\right] - \Lambda_e \Theta \mathbf{I}\right) \tag{43}$$

$$\left[\mathbf{E}'\right] = \left[\mathbf{E}\right] / p_r \,,\ \Lambda_e = \alpha_e q_r / h_r \,. \tag{44}$$

The above stress-strain relation is similar in form to the dimensional form of the stress-strain relation. Next, normalize the displacements with respect to a characteristic length s_r (as was done for the coordinates). That is,

$$\left[\mathbf{u}_m\right] = s_r\left[\mathbf{U}_m\right] \tag{45a}$$

Therefore [4] [5],

$$\left[\mathbf{u}_{m,n}\right] = \left[\mathbf{U}_{m',n'}\right] \tag{45b}$$

Using (45) and the strain-displacement relation, $2\varepsilon_{mn} = \left(u_{m,n} + u_{n,m}\right)$, we have

$$2\varepsilon_{mn} = \left(U_{m',n'} + U_{n',m'}\right) = 2\varepsilon'_{m'n'} \tag{46a}$$

$$\left[\varepsilon\right] = \left[\varepsilon'\right] \tag{46b}$$

The stress-strain-temperature relation in dimensionless form is

[4] Using subscripts *l, m, n,* to indicate plane strain formulation in place of *i, j, k.*
[5] Primed symbols and subscripts *l', m', n',* etc., indicate dimensionless directions.

$$\left[\boldsymbol{\Sigma}\right] = \left[\mathbf{E}'\right]\left(\left[\varepsilon\right] - \Lambda_e \Theta \mathbf{I}\right), \left[\mathbf{E}'\right] = \left[\mathbf{E}\right] / p_r \,. \tag{47a}$$

$$\left[\varepsilon\right] = \left[\mathbf{E}'\right]^{-1}\left[\boldsymbol{\Sigma}\right] + \Lambda_e \Theta \mathbf{I}, \left[\mathbf{E}'\right]^{-1} = p_r \left[\mathbf{E}\right]^{-1} \tag{47b}$$

This dimensionless form of the stress-strain relations is similar to the original standard dimensional form. This is important if the thermal and mechanical problems are to be solved simultaneously for multi-domains using the Finite element method. The dimensionless equilibrium equations in matrix form read

$$\left[\partial'\right]^T \left[\mathbf{E}'\right]\left(\left[\varepsilon\right] - \left[\varepsilon_T\right]\right) = -\rho s_r \left\{\mathbf{f}\right\} / p_r = -\left\{\mathbf{F}\right\} \tag{48a}$$

The dimensionless body force is given by:

$$\left\{\mathbf{F}\right\} = \rho s_r \left\{\mathbf{f}\right\} / p_r \tag{48b}$$

The quasi-static displacement equations are obtained by substituting the stress-strain-temperature relations into the equilibrium equations.

$$\left[\partial'\right]^T \left[\mathbf{E}'\right]\left(\left[\partial'\right]\left[\mathbf{U}\right] - \Lambda_e \Theta \mathbf{I}\right) = -\rho s_r \left\{\mathbf{f}\right\} / p_r = -\left\{\mathbf{F}\right\} \tag{49}$$

As stated earlier, thermal-mechanical coupling is originating at the frictional interface, through the frictional heat boundary conditions. From the theory of thermoelasticity, the coupled temperature equation, assuming a reference-stress-free temperature T_r is given by

$$\rho c \dot{T}(\mathbf{r}, t) + m \rho c \mathbf{v} \bullet \nabla T + \gamma T_r \dot{e} = \nabla \bullet \left(k \nabla T\right) + q_b \tag{50}$$

where $\dot{e} = \dot{\varepsilon}_{kk}$ is the volume dilatation. Under the assumption of a quasi-static mechanical model, the volume dilatational term on the left-hand side of the equation is to be neglected, thus leaving only the heat equation and its boundary conditions, as given in the previous section. Thermal expansion is considered in the elasticity equations, and thermal-mechanical coupling are enforced through the heat flux boundary condition and the coulomb friction law.

Dimensionless Mechanical Boundary Conditions

Dimensionless mechanical boundary conditions are either Dirichlet type (displacement is specified) or Neumann type (stress is specified):

$$U_i = D_i \text{ on } \partial\mathbb{R} \tag{51}$$

$$\boldsymbol{\Sigma}_{ij} n_j = P_i \text{ on } \partial\mathbb{R} \tag{52}$$

The dimensionless contact pressure

$$P_c = p_c \big/ p_r \tag{53}$$

The associated dimensionless heat flux input for the thermal problem is given by:

$$Q_c = \mu_c P_c \left| V \right| \tag{54}$$

The Contact Model

At the contact interface, the following mechanical boundary conditions are assumed for frictional sliding:

$$\sigma_{z1} = \sigma_{z2} = p_c :: \text{on } S_c \tag{55a}$$

$$\tau_{xzi} = \mu p_c :: \text{on } S_c,\ i = 1,2 \tag{55b}$$

$$\sigma_{zi} = \tau_{xzi} = \tau_{yzi} = 0 :: \text{on } S_{nc},\ i = 1,2 \tag{55c}$$

The contact pressure is ordinarily not known in advance and the conventional method of determining the contact parameters is as follows. Assume that the separation functions, between the two bodies before and after the application of load, are called $e_0\left(x,y\right)$ and $e_c\left(x,y\right)$ as shown in Figure 36. The following conditions must hold at the interface:

$$p_c\left(x,y\right) \geq 0\,,\; e_c\left(x,y\right) = 0 \;::\; \left(x,y\right) \in S_c \tag{55e}$$

$$p_c\left(x,y\right) = 0\,,\; e_c\left(x,y\right) \geq 0 \;::\; \text{otherwise.} \tag{55f}$$

The distance between two points A, B on the interface surfaces of the two bodies is given in terms of the relative approach distance denoted u_a, the initial distance, and the normal surface displacements, such that:

$$e_c\left(x,y\right) = e_0\left(x,y\right) + u_1 + u_2 - u_a \tag{55g}$$

where u_i, $i = 1,2$ are the normal surface displacements calculated as the summation of components due to normal, shear, and thermal loading.

This formulation describes the conventional numerical procedure of treating contact interface and thermomechanical coupling. This procedure is mathematically and computationally demanding, especially in a transient solution where an equilibrium state is required at each instant. In order to simplify the problem, the following assumption is adopted in this research: Classic contact theory is applied to compute the contact pressure distribution. This ensures load equilibrium at each time step and eliminates the need for iteration and speeds up the solution. Thermal expansion at the interface of the rubbing bodied affects the gap interface as the parts expand (or shrink) in response to thermal loading. This has a direct effect on the contact area and contact pressure. The computed displacements due to thermal expansion determine the geometry at the interface. This provides a method of calculating the evolution of the average contact width and mean pressure. In this research, two classic contact theories are considered: the Hertzian and the Conformal contact models. The solutions of these theories are described for the pin-bushing configuration in Chapter 9.

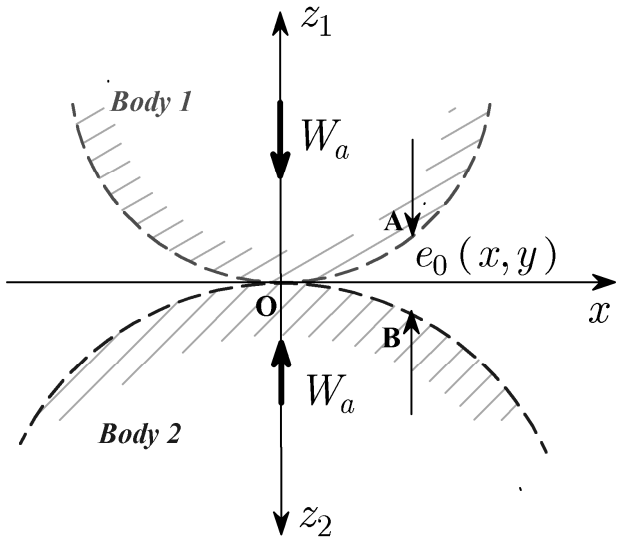

(a) configuration before loading.

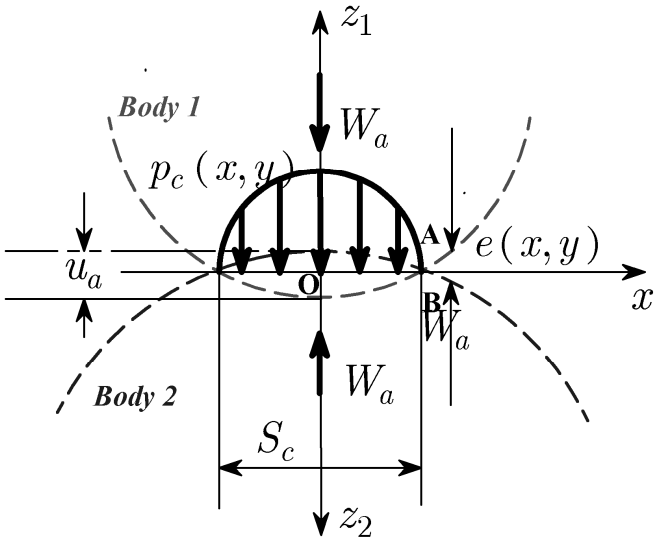

(b) deformed configuration.

Figure 36. Schematic of the conventional contact problem

Chapter 7. Application to Known Configurations

To validate the finite element solution, we look at some published results from the literature. Some of the reported literature in the field, such as Hirano and Yoshida [17]; Greenwood and Alliston-Greiner [25]; Krishnamurthy [36], considered the simple thermal problem configuration shown Figure 37(a), and relied on analytical methods to reach a solution. Other configurations where the motion is circular have been studied both analytically and numerically, such as Hazlett and Khonsari [6] in the study of bearing seizure, Tseng et al. [37] in the analysis of hot rolling process, with configurations as shown Figure 37(b). In the first case, the shaft is subject to a rotating heat flux, while in the second case, the roller is rotating and a heat flux is applied over the bite angle. These case studies were solved by applying the thermal model described in the previous chapters using the finite element method.

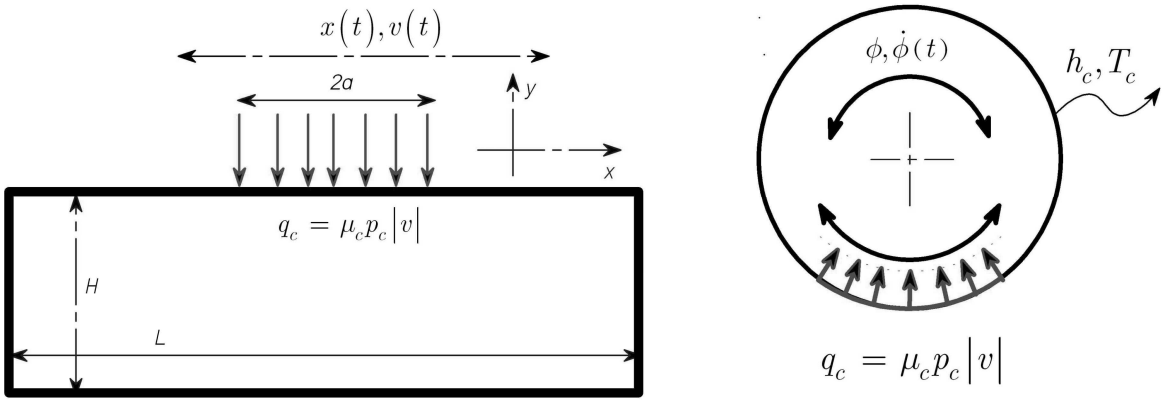

(a) Moving heat flux on flat.

(b) Heating/cooling on shaft surface.

Figure 37. Examples of thermal problems.

Heat Flux on Flat Thermal Problem

In the pin-on-flat configuration, the two parts are pressed together with an applied load, and are allowed to slide relative to one another. Therefore, frictional heating is generated at the contact between them and the temperature rises. It is assumed that the pin is adiabatic, that the flat is large compared to the contact width so that the temperature at the far ends may be considered fixed, and that the heat flux is constant over the contact area. Therefore, the thermal problem can be solved by considering only the conducting body subject to a heating flux on its surface, as shown in Figure 38. In this Figure, two physical configurations are considered. In the first one, the flat is moving while the heat flux is stationary [17]. In the second problem, the flat is stationary while the heat flux is moving on the surface [36]. Assume that the end walls of the flat are subject to identical boundary conditions in both cases. Notice that since the heat flux in both configurations sweeps through the same area on the surface of the conducting body, at the same speed, and with the same amount of heat flux at each instant, and provided that the same boundary conditions are applied at the far boundaries of the flat, the two thermal configurations are physically equivalent. Mathematically, the convective term present in the heat equation in case (a) is absent in case (b), and the two thermal problems are equivalent only when observed from proper reference frames. The two cases were solved on the same domain with identical material properties, operating and boundary conditions; see Example 1.

The governing equation for the temperature change in the conducting medium is

$$k\nabla^2 T + q_b = \rho c\, \partial T \big/ \partial t + m\rho c v\, \partial T \big/ \partial x\,,\ t > 0 \tag{56}$$

$$-L\big/2 \le x \le L\big/2\,,\ -H\big/2 \le y \le H\big/2 \tag{56a}$$

where the term q_b is an internal heat sink that results from averaging the 3D heat equation over the axial (z-) direction. This term will be neglected in this chapter. Suppose that the initial temperature everywhere is given by $T_0(x,y)$ = 0, and the boundary conditions are given as specified values and mixed at the boundaries as follows:

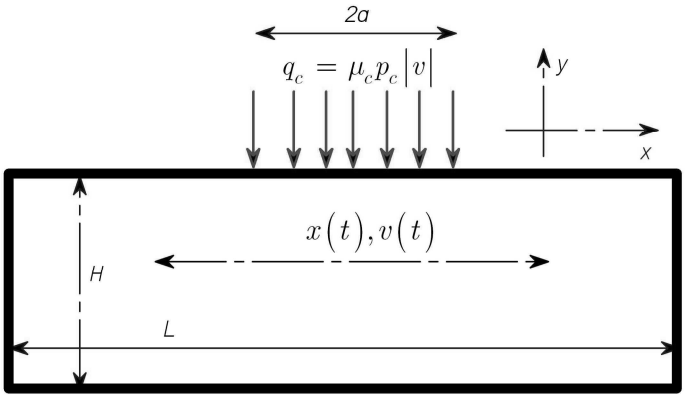

(a) Moving flat, stationary heat flux.

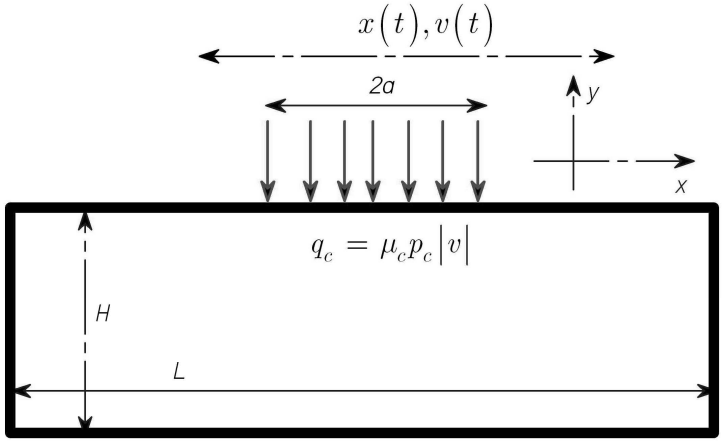

(b) Stationary flat, moving heat flux.

Figure 38. Pin-flat thermal problem

$$\left[T\left(x,y,t\right)\right]_{\substack{x=\pm L/2 \\ y=-H/2}} = T_e :: t > 0 \tag{57}$$

$$\left[k\,\partial T/\partial n + h\Delta T\right]_{y=H} = q\,,\; t > 0 \tag{58}$$

where $q\left(t,x\right)$ is a heat flux input and $h\left(t,x\right)$ is a convective heat transfer coefficient, both time and position dependent.

$$q\left(t,x\right)=\begin{cases} q_c & \left|x\right|\le a \\ 0 & Otherwise \end{cases},\quad h\left(t,x\right)=\begin{cases} 0 & \left|x\right|\le a \\ h_{nc} & Otherwise \end{cases} \tag{59}$$

The position, velocity and heat generation may be written as follows:

$$x=x_0+x_m\Phi\left(\omega t\right),\ v=dx\big/dt=x_m\,d\Phi\big/dt \tag{60a}$$

$$q_c=\mu p_c\left|v\right| \tag{60b}$$

where $\Phi\left(\bullet\right)$ is a periodic function of time of unit amplitude, period T, and frequency $\omega=2\pi\big/\mathrm{T}$. For a constant-speed oscillation, the velocity and position functions may be expressed over one period interval as:

$$v=\pm v_{m,c},\ x=x_0\pm v_{m,c}t::0\le t\le \mathrm{T} \tag{61a}$$

The position and speed amplitudes are related to the period as follows:

$$v_{m,c}\mathrm{T}=4x_m \tag{61b}$$

Thus, $x - x_0 = x_m \Phi\big(\omega t\big)$ where after using (61b),

$$\Phi\big(\omega t\big) = \pm\Big(v_{m,c}\Big/x_m\Big)t :: 0 \le t \le \mathrm{T} \tag{61c}$$

The frequency of oscillation is given by the familiar relation:

$$\omega = 2\pi\Big/\mathrm{T} = \Big(\pi\Big/2\Big)\Big(v_{m,c}\Big/x_m\Big). \tag{61d}$$

For instance, assuming that the velocity and position functions are defined on the time interval $0 \le \omega t \le 2\pi$ by

$$v = v_{m,c}\begin{cases} 1 & 0 \le \omega t \le \pi\Big/2 \\ -1 & \pi\Big/2 \le \omega t \le 3\,\pi\Big/2 \\ 1 & 3\,\pi\Big/2 \le \omega t \le 2\pi \end{cases} \tag{61e}$$

$$x - x_0 = x_m\begin{cases} 0 + \Big(v_{m,c}\Big/x_m\Big)t & 0 \le \omega t \le \pi\Big/2 \\ 2 - \Big(v_{m,c}\Big/x_m\Big)t & \pi\Big/2 \le \omega t \le 3\,\pi\Big/2 \\ -4 + \Big(v_{m,c}\Big/x_m\Big)t & 3\,\pi\Big/2 \le \omega t \le 2\pi \end{cases} \tag{61f}$$

$$\Phi\big(\omega t\big) = \begin{cases} 0 + \Big(v_{m,c}\Big/x_m\Big)t & 0 \le \omega t \le \pi\Big/2 \\ 2 - \Big(v_{m,c}\Big/x_m\Big)t & \pi\Big/2 \le \omega t \le 3\,\pi\Big/2 \\ -4 + \Big(v_{m,c}\Big/x_m\Big)t & 3\,\pi\Big/2 \le \omega t \le 2\pi \end{cases} \tag{61g}$$

For a harmonic motion, the amplitude and frequency are specified. Assuming sinusoidal time function, $\Phi_h\left(\omega t\right) = \sin(\omega t)$, we have:

$$x - x_0 = x_m \Phi_h(\omega t) = x_m \sin(\omega t),\ \omega = 2\pi/\mathrm{T} \tag{62a}$$

$$v = dx/dt = x_m \omega\, d\Phi_h/d(\omega t) = x_m \omega \cos(\omega t) = v_{m,h}\dot{\Phi}(\omega t) \tag{62b}$$

$$v_{m,h} = x_m \omega \tag{62c}$$

If it is desired that both square and harmonic motions have the same amplitude and period, then set equal periods to we obtain the equivalent harmonic frequency in terms of constant speed parameters. Recall that for constant speed motion, (61b) gives:

$$\mathrm{T} = 4x_m/v_{m,c} \tag{62d}$$

Thus,

$$2\pi/\omega_h = 4x_m/v_{m,c} \rightarrow \omega_h = 2\pi v_{m,c}/\left(4x_m\right) \tag{62e}$$

$$v_{m,h} = \left(\pi/2\right) v_{m,c} \tag{62f}$$

In the rotational case, we have

$$\mathrm{T} = 4\phi_m/\omega_c \tag{62d}$$

Thus,

$$2\pi/\omega_h = 4\phi_m/\omega_c \rightarrow \omega_h = 2\pi\omega_c/(4\phi_m) \tag{62e}$$

$$v_{m,h} = (\pi/2)v_{m,c} \tag{62f}$$

Thus, for an equivalent harmonic position of same amplitude and period, the constant velocity must be lower than the harmonic velocity amplitude by a factor of $\pi/2$, as seen from Equation (62f). In this case, the harmonic position function circumscribes the triangular position function, but the velocity amplitudes are related by Equations (62f); see Figure 39 (b). This relationship also ensures the same mean heat input per cycle. The resulting temperature distributions for the two motion profiles may however be different due to the difference the durations that heat flux is applied.

Dimensionless Equations

In this problem, we set the dimensionless time, coordinates, and temperature rise as follows, where we take the half contact width as a reference value for space, $s_r = a$, and the angular frequency is used to normalize time $t_r = 1/\omega$. Thus,

$$\tau = \omega t,\ x = aX,\ y = aY \tag{63a}$$

$$\Delta T = (q_r/h_r)\Theta \tag{63b}$$

Based on (63a), the normalized half width of contact is $A = 1$, the resulting normalizing speed is $v_r = (a\omega)$, the normalized cycle time is $\Upsilon = \omega \mathrm{T} = \omega(2\pi/\omega) = 2\pi$, the normalized angular frequency is unity, $\Omega = 1$, and the normalized cyclic frequency is $F = 1/\Upsilon = 1/(2\pi)$. The dimensionless harmonic position and velocity are:

$$(X - X_0) = X_m\Phi(\tau),\ X_m = x_m/a \tag{64a}$$

$$V(\tau) = dX/d\tau = X_m\, d\Phi(\tau)/d\tau \tag{64b}$$

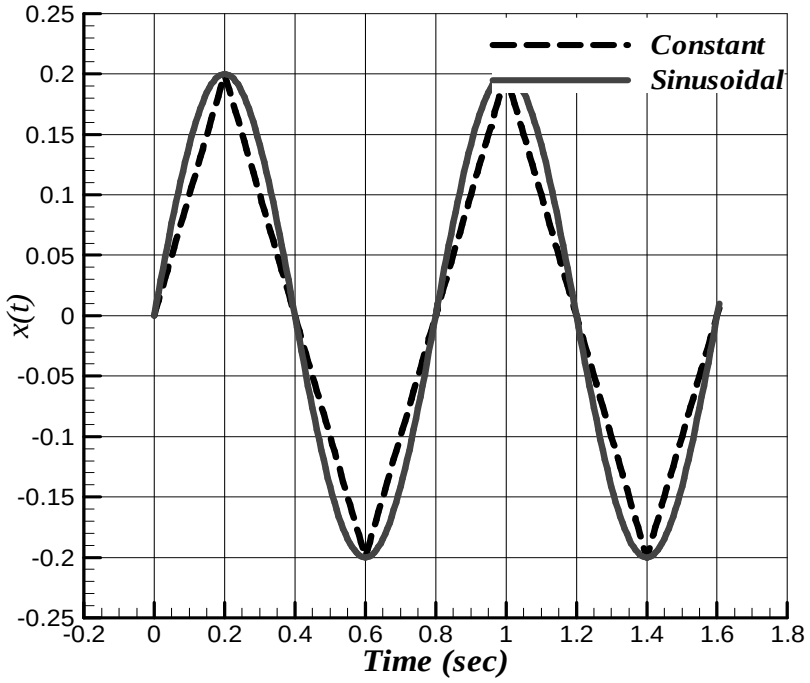

(a) Position

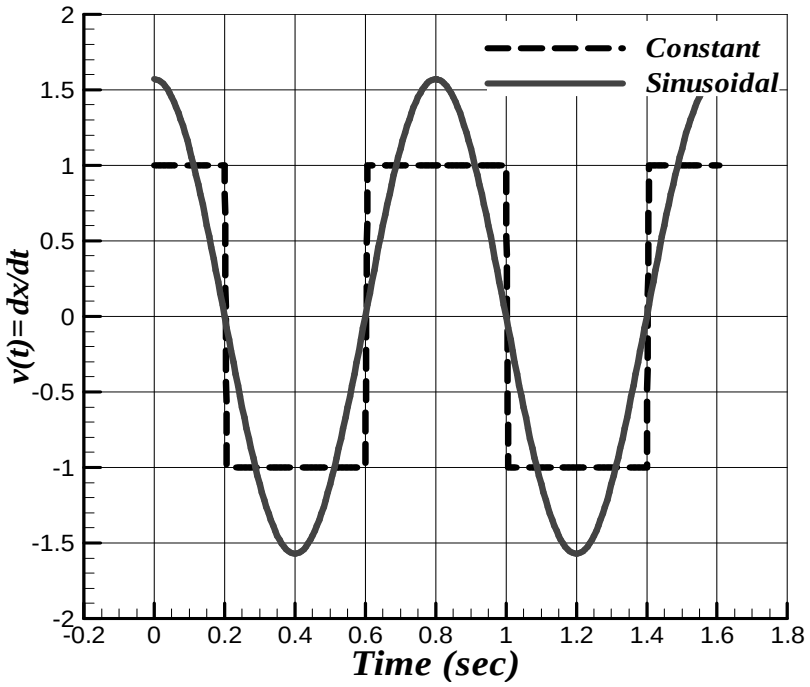

(b) Velocity

Figure 39. Equivalent harmonic and constant speed oscillatory motion.

For constant reciprocating velocity, the dimensionless velocity and position are given by

$$X - X_0 = X_m \Phi(\tau),\ \Phi(\tau) = \pm\left(2\tau/\pi\right). \tag{65a}$$

$$V(\tau) = dX/d\tau = X_m \, d\Phi(\tau)/d\tau = \pm(2/\pi) X_m \tag{65b}$$

More specifically, for the constant speed profile, we have

$$(X - X_0) = \begin{cases} (2X_m/\pi)\tau & 0 \le \tau \le \pi/2 \\ 2X_m - (2X_m/\pi)\tau & \pi/2 \le \tau \le 3\pi/2 \\ -4X_m + (2X_m/\pi)\tau & 3\pi/2 \le \tau \le 2\pi \end{cases} \tag{66a}$$

$$V = \begin{cases} (2X_m/\pi) & 0 \le \tau \le \pi/2 \\ -(2X_m/\pi) & \pi/2 \le \tau \le 3\pi/2 \\ (2X_m/\pi) & 3\pi/2 \le \tau \le 2\pi \end{cases} \tag{66b}$$

The interface boundary condition in its dimensionless form becomes

$$K\frac{\partial \Theta}{\partial n} + B_i \Delta\Theta = B_{ir} Q \tag{67a}$$

where the dimensionless conductivity is defined: $K = k/k_r$, with a reference conductivity corresponding to the moving part, and the Biot number is defined as $B_i = ha/k_r$, $B_{ir} = h_r a/k_r$. It is important to note that the thermal conductivity is not simplified out at the interface in order to account for material discontinuity at the boundary-interface in the case of multi-domain problems. The dimensionless heating/cooling fluxes at the interface are described by

$$Q = \begin{cases} \mu P_c |V(\tau)| & |X - X_c| \le 1 \\ 0 & Otherwise \end{cases} \tag{67b}$$

$$B_i = \begin{cases} 0 & |X - X_c| \le 1 \\ Bi_{nc} & Otherwise \end{cases} \tag{67c}$$

The heat equation in its dimensionless form becomes

$$K\nabla^2\Theta + B_{ir} Q_b = \frac{K}{\Lambda} P_e \Theta_{,\tau} + m\frac{K}{\Lambda} P_e V(\tau) \Theta_{,X} \tag{68}$$

The Peclet number is defined with respect to the moving part, as $P_e = av_r/\kappa_r = a^2\omega/\kappa_r$, and the thermal diffusivity is $\kappa = k/\rho c$. The dimensionless source term is zero in this case, $Q_b = 0$.

The coefficients of the dimensionless heat equation in the above form may be rewritten in standard form:

$$K_e\nabla^2\Theta + B_{ir}Q_b = D_eC_e\Theta_{,\tau} + mD_eC_eV(\tau)\Theta_{,X} \tag{69a}$$

$$K_e = K,\ D_eC_e = KP_e/\Lambda \tag{69b}$$

Define the numerical proportionality ratio $\zeta = \rho/c$, and impose the condition $D_e/C_e = \zeta$, which physically enforces a proportionality condition between the density and heat capacity. Solving we obtain:

$$C_e = \sqrt{KP_e/\Lambda}/\sqrt{\zeta},\ D_e = \sqrt{KP_e/\Lambda}\sqrt{\zeta}. \tag{69c}$$

Example 1. Heat Flux on a Moving Flat

Hirano and Yoshida. [17] used analytical methods to solve for the temperature rise at the surface of an oscillating flat body that is acted upon by an adiabatic square shaped pin, with side, $2a$. The flat was modeled as a semi-infinite body oscillating sinusoidally with amplitude x_m and frequency ω. The following dimensionless space, time, and temperature variables were used:

$$\tau' = \omega t,\ x = aX',\ y = aY',\ \Delta T = \left(\frac{2\mu_c p_r \kappa_r}{\pi^{3/2}k_r}\right)\Theta' \tag{70a}$$

Comparing these variables to the present dimensionless model parameters, we observe the following relations (primed symbols belong to the published model in [17]):

$$\tau' = \tau,\ A' = x_m \big/ a = X_m,\ M'^2 = a^2\omega \big/ \left(4\kappa_r\right) = P_e \big/ 4\,. \tag{70b}$$

$$\Delta T = \left(\frac{2\mu_c p_r \kappa_r}{\pi^{3/2} k_r}\right)\Theta' = \left(\frac{p_r v_r}{h_r}\right)\Theta \tag{70c}$$

Thus, given $A',\ M'$, we have $P_e = 4M',\ X_m = A'$. In order to compare results, we solve the problem numerically using the above parameters. We may consider any combination of material properties, geometries, and speeds provided that the Peclet number and dimensionless amplitude of oscillation are as given above. Notice that the dimensionless solution is independent of the load by normalization. The Peclet number is defined $P_e = a v_r \big/ \kappa_r = a^2\omega \big/ \kappa_r$, so if Carbon Steel is used, and a is selected, then the frequency is found from $\omega = \kappa_r P_e \big/ a^2$. We solve the problem using equivalent model parameters, and transform the temperature according to (18c). The first published example in [17] considers the following parameters: $A' = 1,\ M' = 1$, and the dimensionless surface temperature rise at $Y' = 0,\ X' = 0,\ 0.5,\ 1$, and looks at the transient and steady state behaviors of the dimensionless temperature rise at those locations. Figure 40 shows the finite element mesh used in the calculations, where the flat dimensions are assumed to be as shown.

Figures 41 (a, b) show the resulting transient temperature behavior at selected location on the heated surface obtained using the present model and from published results. Figures 42 (a, b) show the temperature variation at steady state at three selected locations obtained using the present model and from published results. The finite element code was able to capture the behavior that was predicted analytically. The Temperature rise in this case is slightly larger. This discrepancy can be explained by the finite domain limitation used in the numerical solution and the relative size of the flat compared to the contact width. Figures 43 and 44 illustrate the

case when the flat is stationary while the heat flux oscillates back and forth on the same surface. The same input data and boundary conditions as in Example 1 were used, but comparison with Figures 41 and 42 shows a difference in the temperature histories. This is because both solutions are carried out in the same fixed Eulerian frame. Identical solutions would be obtained if the problem is reformulated within a reference frame attached to the moving body in Example 1. However, the expression for the mixed boundary condition on the heated surface, as seen from the moving reference frame, would be more complicated and difficult to implement numerically. Within such a moving frame, identical temperature histories would be obtained since they would refer to identical locations on the finite element solution domain for the two configurations in Figure 38.

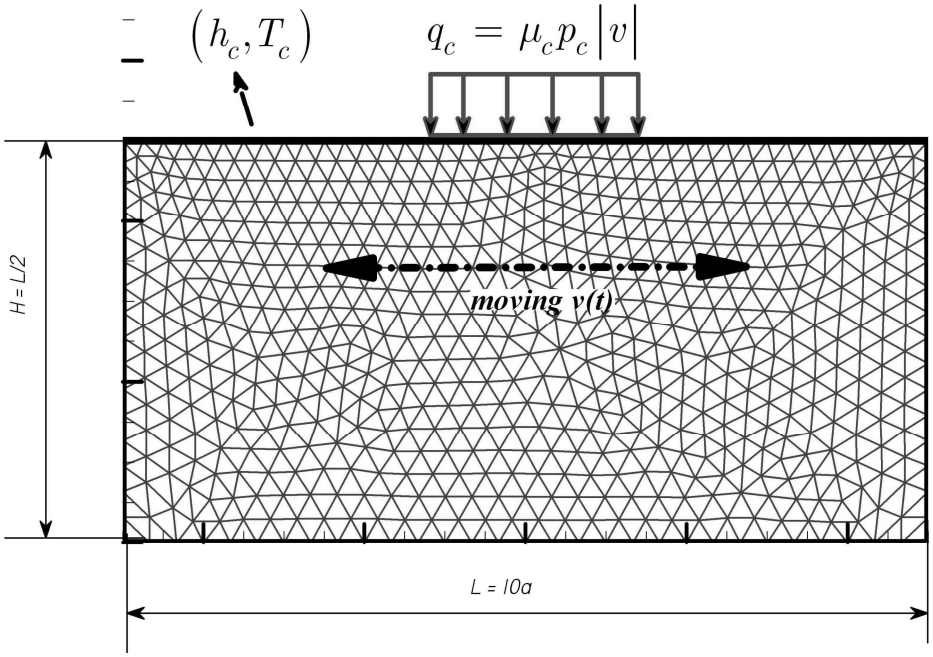

Figure 40. Finite element mesh used in Example 1.

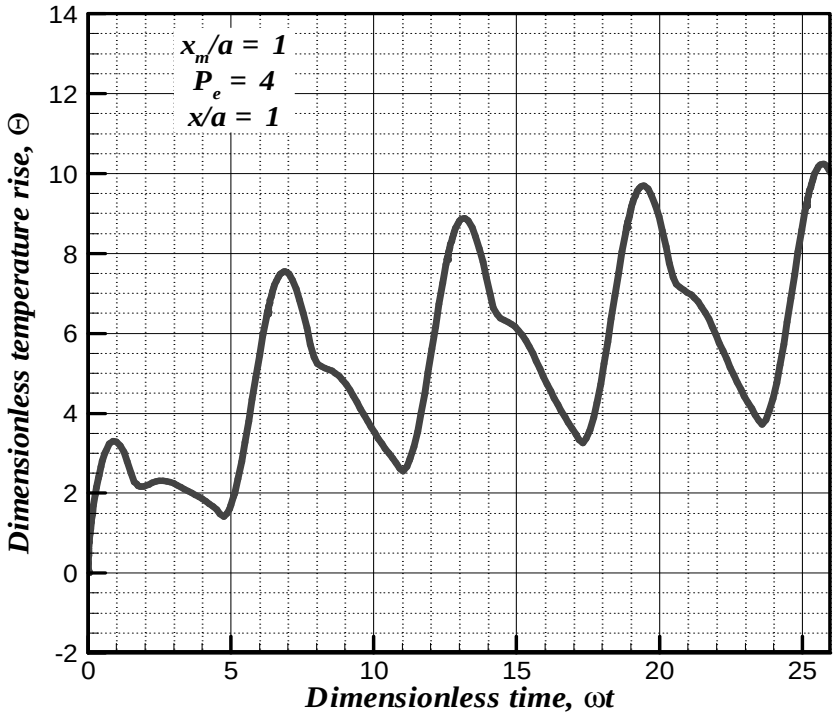

Figure 41a. Transient temperature rise at contact tip - present model [17].

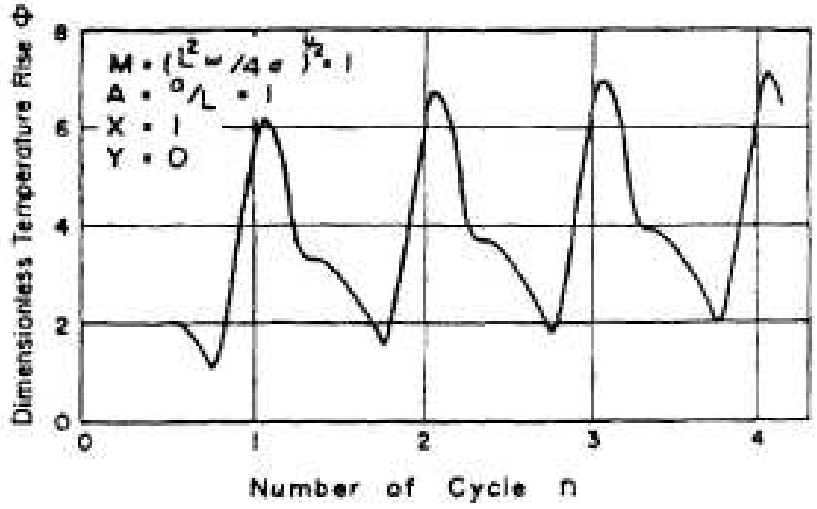

Figure 41b. Transient temperature rise at contact tip - published results [17].

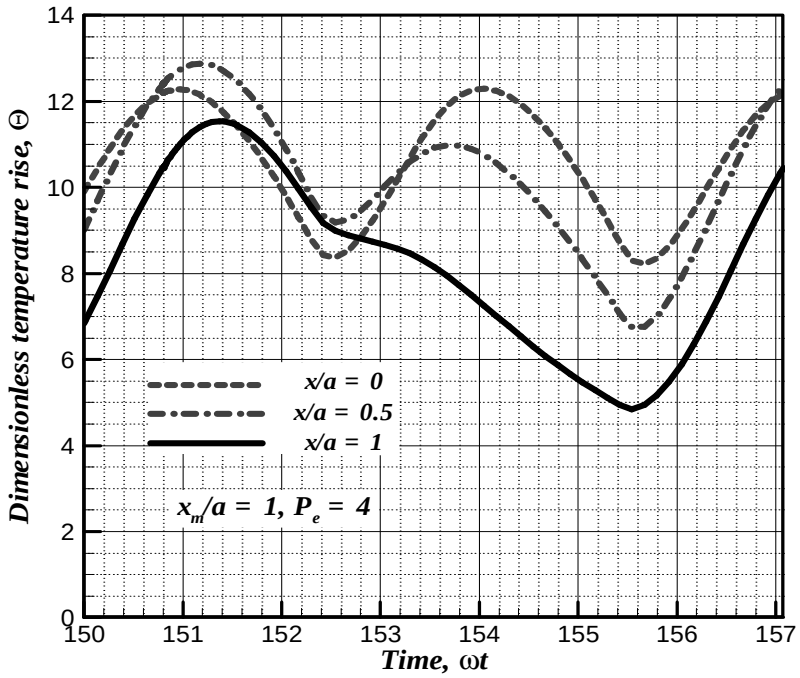

Figure 42a. Temperature rise variation at steady state – present model [17].

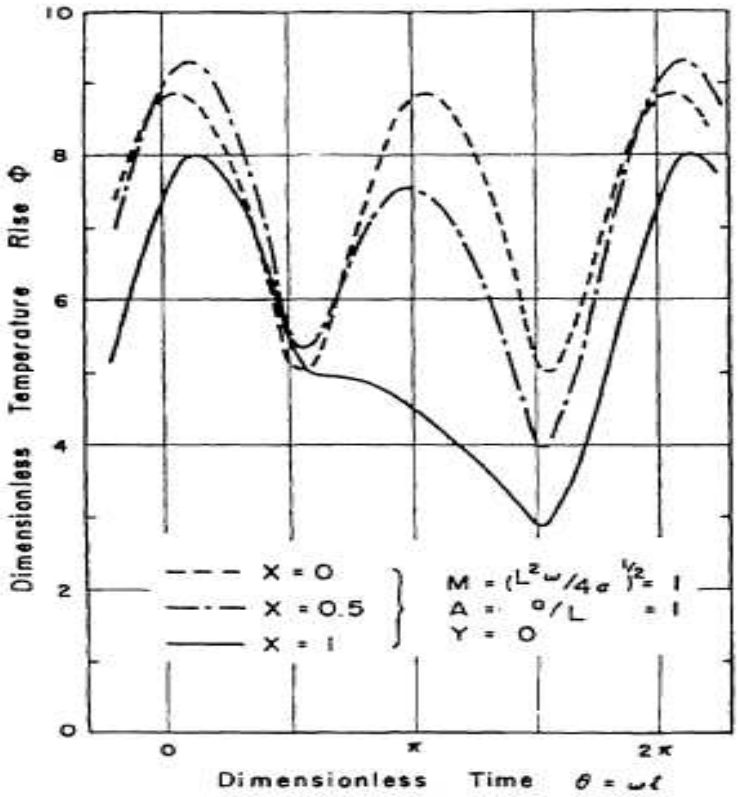

Figure 42b. Temperature rise variation at steady state – published results [17].

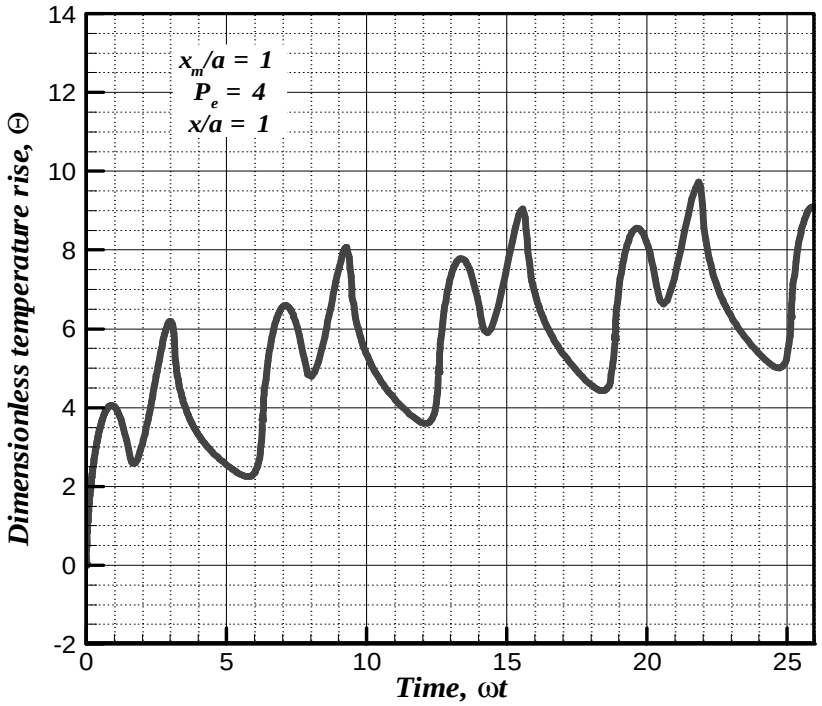

Figure 43. Transient temperature variation (data from [17])

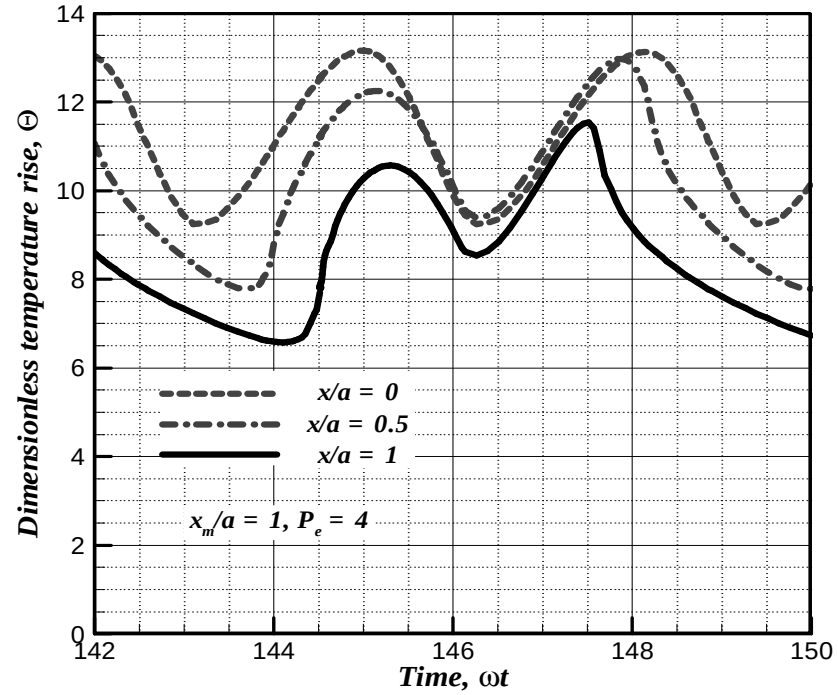

Figure 44. Temperature variation at steady state (data from [17])

Example 2. Fretting Contact Temperature

The fretting is characterized by small amplitude reciprocating contact [25]. In some of the published literature seeking solutions to surface temperatures in fretting contact, a simple analytical solution is obtainable by ignoring the varying position of the slider (i.e., the pin in the pin-on-disk experiment), and assuming that the slider takes no heat. In addition, the contact region is assumed to be small enough for conducting medium to be treated as a half-space [25]. The authors in [25] obtained a solution that considers adiabatic condition at points on the boundary that are outside the contact, according to available results found in Carslaw and Jaeger [23]. They presented a simple analysis for the surface temperature developed in a small-amplitude fretting, with circular contact spot of radius r, frequency ω, and heat flux $q = q_m \left|\sin\left(\omega t\right)\right|$, where $q_m = \mu_c p_m x_m \omega$ is the maximum heat flux, and x_{m} the amplitude. They introduced a dimensionless parameter, $\gamma = r\sqrt{\omega/\kappa}$, and expressed the surface temperature rise as a sum of a steady state and periodic parts. For the circular contact spot, the temperature rise is given by steady state and periodic components as follows:

$$\Theta_s^{'} = \frac{2\gamma}{\pi} \tag{71a}$$

$$\Theta_p^{'} = \frac{4}{\pi\sqrt{2}} \sum_{m=1}^{\infty} \frac{\cos\left(2m\Omega\tau - \pi/4\right) - \exp\left(-\gamma\sqrt{m}\right)\cos\left(2m\Omega\tau - \pi/4 - \gamma\sqrt{m}\right)}{\sqrt{m}\left(4m^2 - 1\right)} \tag{71b}$$

For a uniformly heated *square contact of side 2a*, the maximum surface temperature at steady state is given by the result for a *circular contact spot* with an equivalent radius related the square contact side by

$$r = \left(2/\pi\right)\ln\left(1+\sqrt{2}\right)\left(2a\right). \tag{72}$$

The dimensionless variables characterizing the solution are:

$$\tau' = \omega t\,,\; x = rX'\,,\; \Theta' = \left(\frac{\gamma k_r}{r q_r}\right)\Delta T\,,\; \gamma = r\sqrt{\omega/\kappa}\,. \tag{73}$$

In terms of the present model variables, we have

$$\Theta'/\Theta = \left(\frac{\gamma k_r}{r q_r}\right)\times\frac{q_r}{h_r} = \frac{\gamma}{r}\frac{k_r}{h_r} = \frac{\gamma}{R}\frac{k_r}{a h_r} = \frac{\gamma}{R B_{ir}} \rightarrow \Theta' = \frac{\gamma}{R B_{ir}}\Theta \tag{74a}$$

$$\gamma^2 = r^2\frac{\omega}{\kappa_r} = R^2\frac{a^2\omega}{\kappa_r} = R^2 P_e \rightarrow R = \gamma/\sqrt{P_e}\,. \tag{74b}$$

Notice that specifying the dimensionless number γ alone provides freedom to choose the amplitude ratio. Under fretting conditions this ratio must be small (γ < 1). Calculations using the present model show good agreement with results reported by Greenwood et al. [25] for the case $\gamma = 0.5$, a = 0.1 cm, 50 Hz, and a steel material. The plots in Figures 45(a) show the dimensionless heat flux, the periodic and steady state temperature rise for one cycle obtained from the present model. Also shown, Figures 45 (b), is a plot of the published results for the periodic temperature component given by Equation (71b) in [25] for comparison in the case of $\gamma = 0.5$. There is good agreement between the computed solution using the present model and the published one. The solution was computed using the finite element method on the finite domain shown in Figure 46, where the far boundaries are chosen at a distance equal to 20 times the contact width. The contour plot shows the resulting steady state temperature distribution within the conducting body. Figure 46 also shows that the mesh is adapted to be very fine, in order to resolve the Newton-Raphson error requirement ($\leq 10^{-5}$) at points in the vicinity of the contact where the temperature gradients are very high and change rapidly with time. This adaptation is part of all the finite element solutions carried out using the present model.

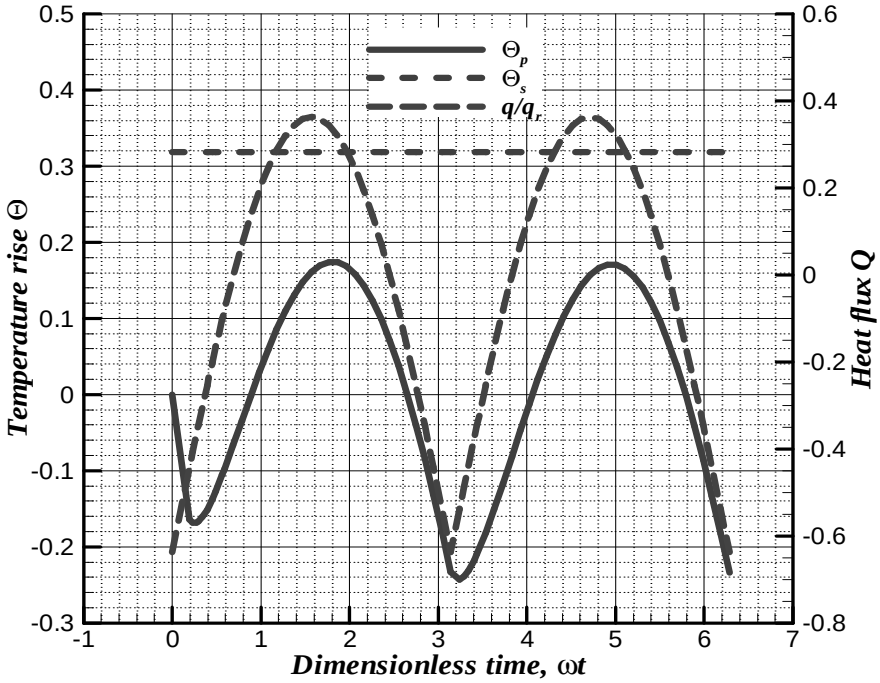

Figure 45a. Fretting contact temperature: present model $\gamma = 0.5$ [25]

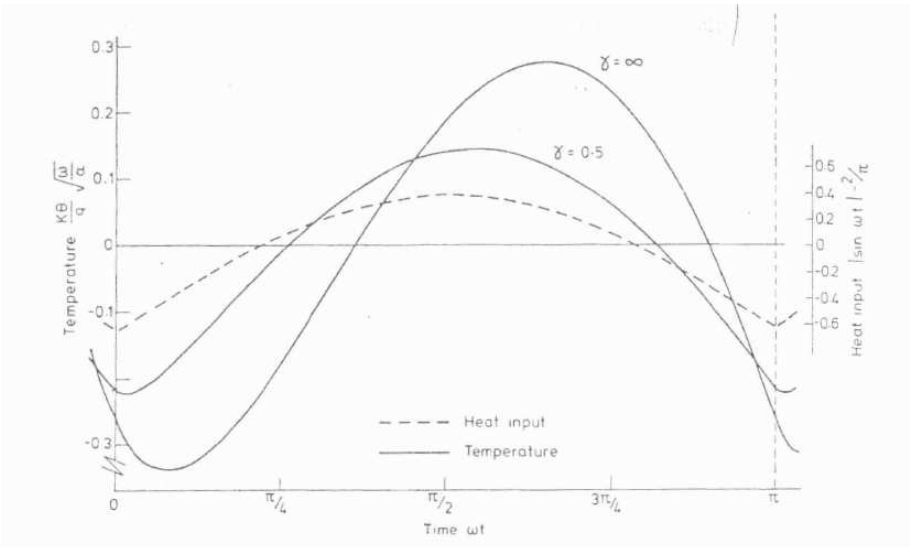

Figure 45b. Fretting contact temperature: published results $\gamma = 0.5$ [25]

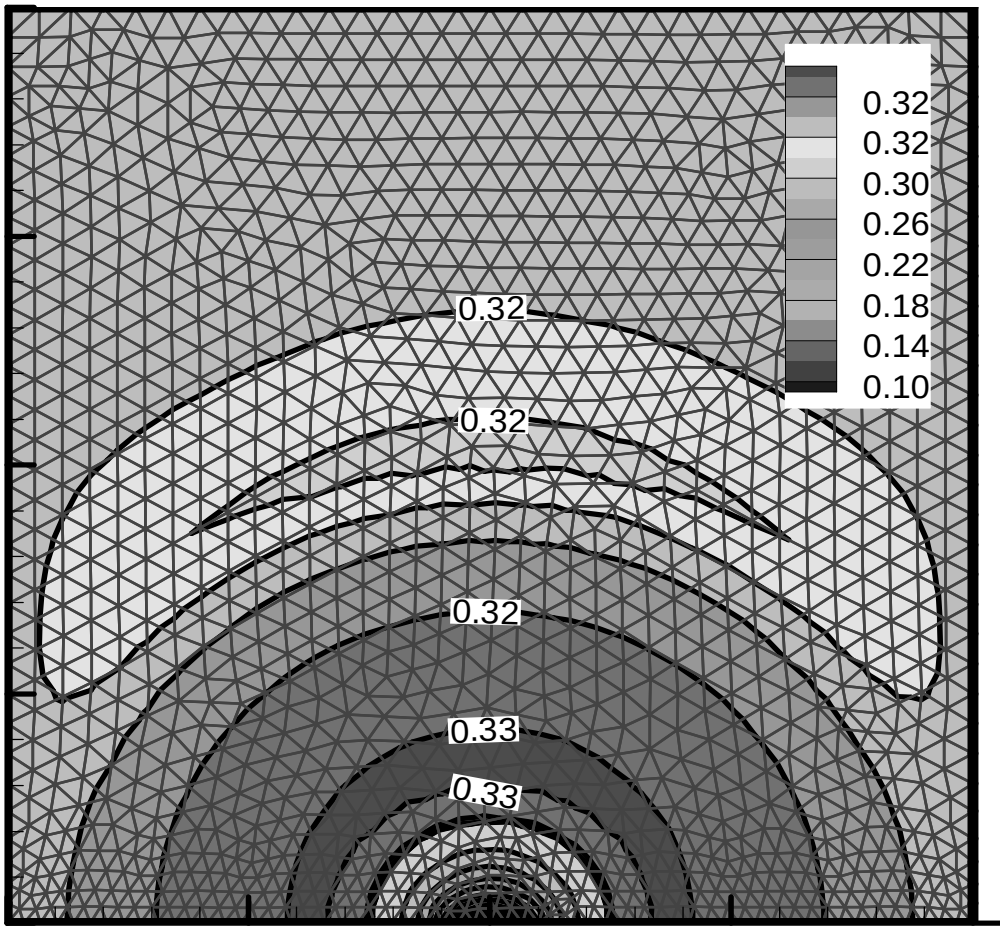

Oscillating Heat Source
Small amplitude: $x_m/a << 1$

Figure 46. Finite element domain, steady state temperature [25]

Example 3. Moving Heat Flux on Flat

Krishnamurthy [36] used the Duhamel's theorem and the superposition principle to construct the temperature solution for a case of a uniform heat flux oscillating back and forth at constant speed on the surface of a block as shown in Figure 38(b). The analytical solution was implemented using the finite element discretization. The rectangular flat was 0.3 m by 0.1 m, and the heat flux width was 0.1 m and magnitude 50 kW, oscillating at the constant speed of 1.2m. Figures 47 (a, b), obtained using the present model and the published results, show the surface temperature rise at selected locations on the heated surface. The computed results

compare well with the reported ones in [36]. Figure 48 shows the problem configuration, the finite element mesh, and the temperature rise within the conducting body at steady state.

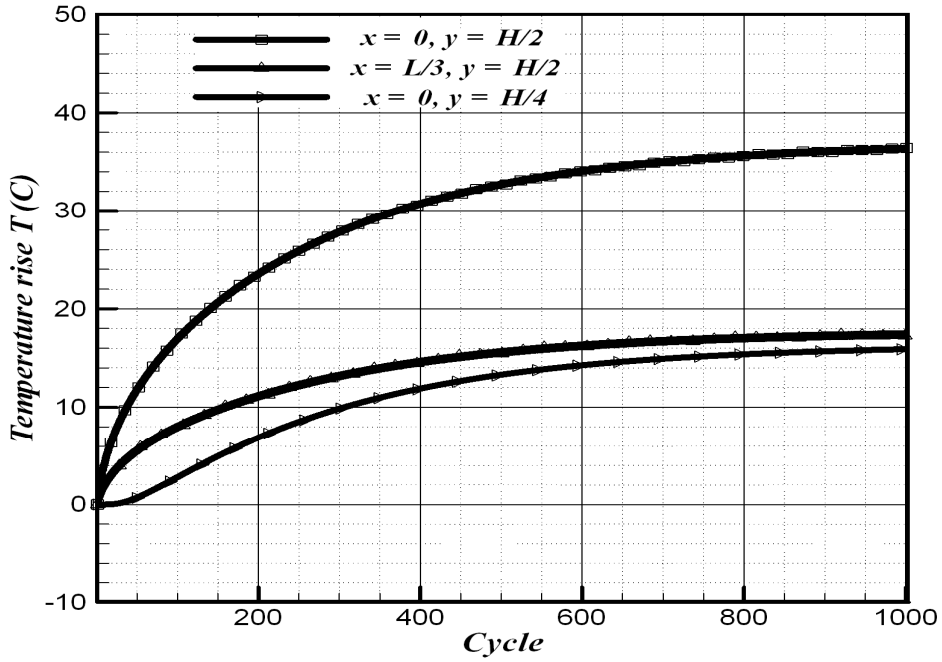

Figure 47a. Transient surface temperature rise at selected locations - present model [36].

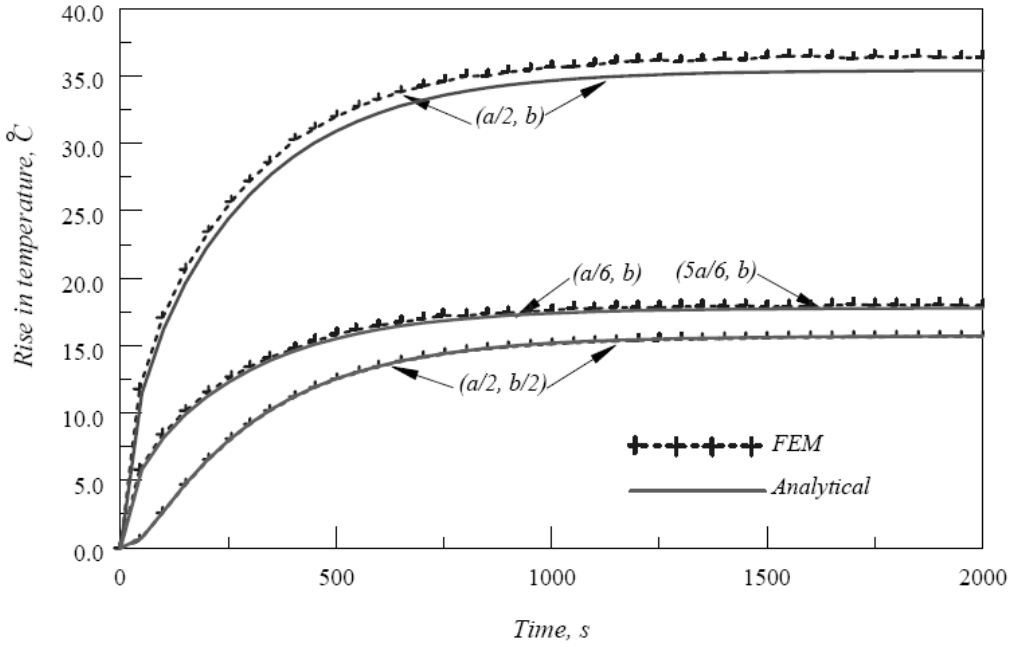

Figure 47b. Transient surface temperature rise at selected locations - published results [36].

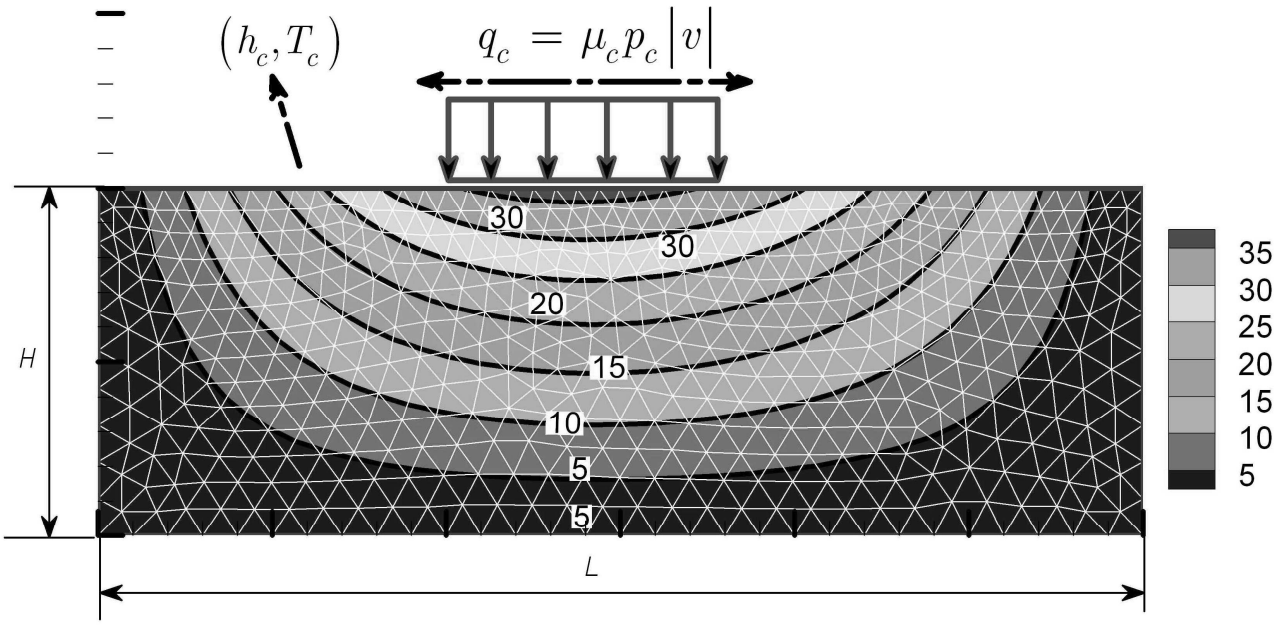

Figure 48. Thermal problem configuration and FE mesh for Example 3.

Example 4. Moving Heat Flux on Shaft Surface

Hazlett and Khonsari [6] considered a shaft of radius $r_s = 25.5$ mm made of steel material. A heat flux of magnitude 539.216 kW, a width of 36 degrees, and rotating unidirectionally at a constant speed of N = 250 rpm, is applied on the surface of the shaft. Convective cooling at ambient temperature and a heat transfer coefficient h=80 W/m.K is applied to the surface at locations that are not heated. Figure 49 shows a schematic of the thermal problem and the temperature rise within the shaft after 10 seconds (about 41.6 cycles).

The resulting temperature rise at three selected locations, $r = r_s,\ 0.9r_s,\ 0.8r_s$ at $\theta = \pi/2$, are plotted in Figure 50. The corresponding published results taken from [6] are shown in Figures 51-53. There is good agreement between the present and reported results.

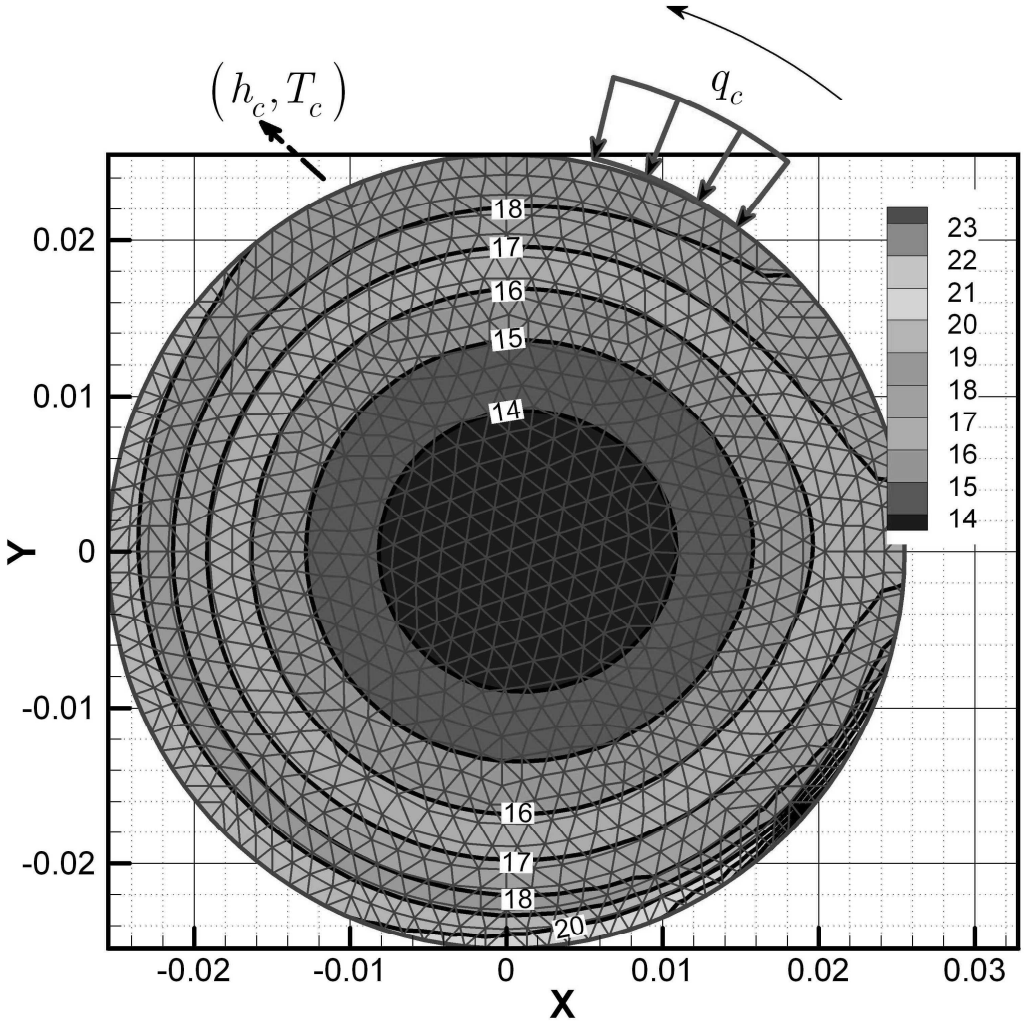

Figure 49. Thermal problem configuration and mesh pattern for Example 4 [6].

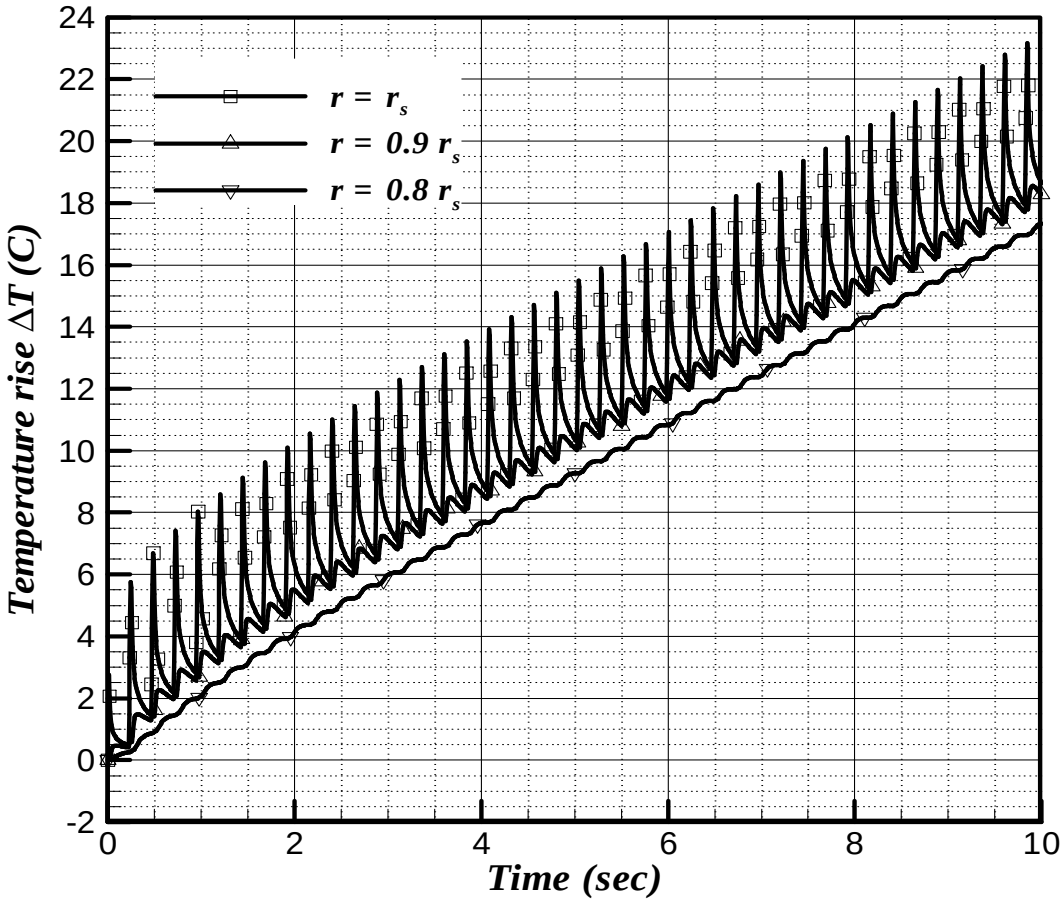

Figure 50. Transient surface temperature rise at selected location on shaft [6].

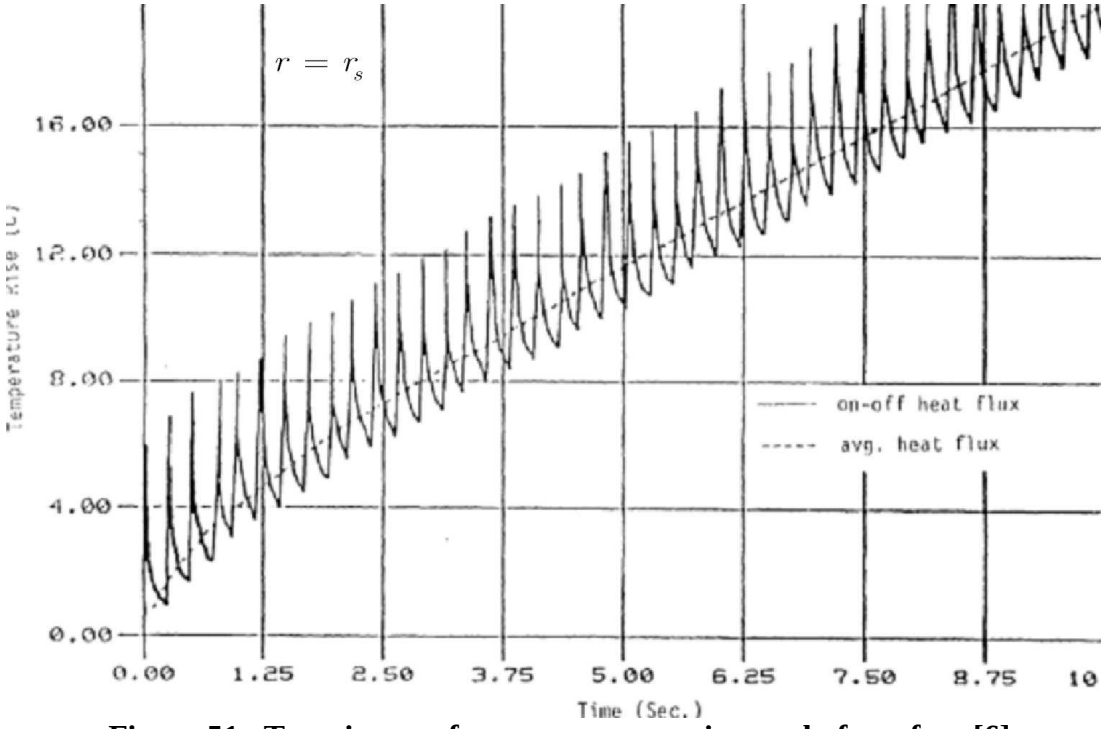

Figure 51. Transient surface temperature rise on shaft surface [6].

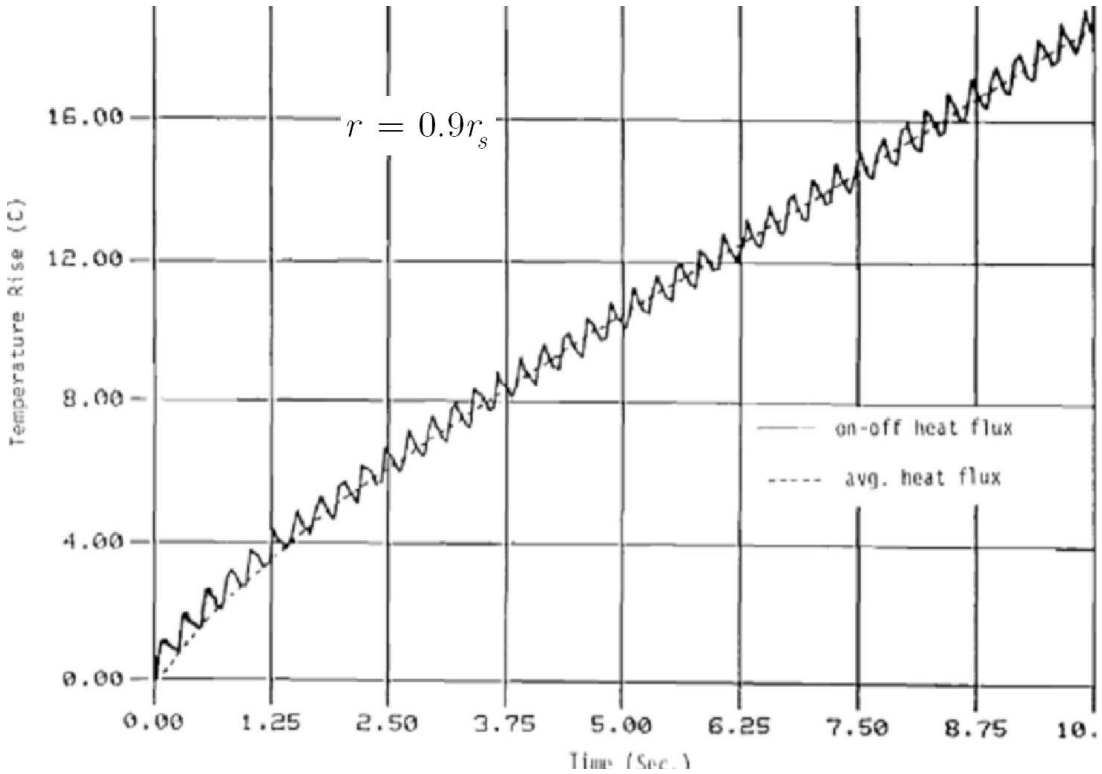

Figure 52. Transient surface temperature rise at $r = 0.9r_s$ [6].

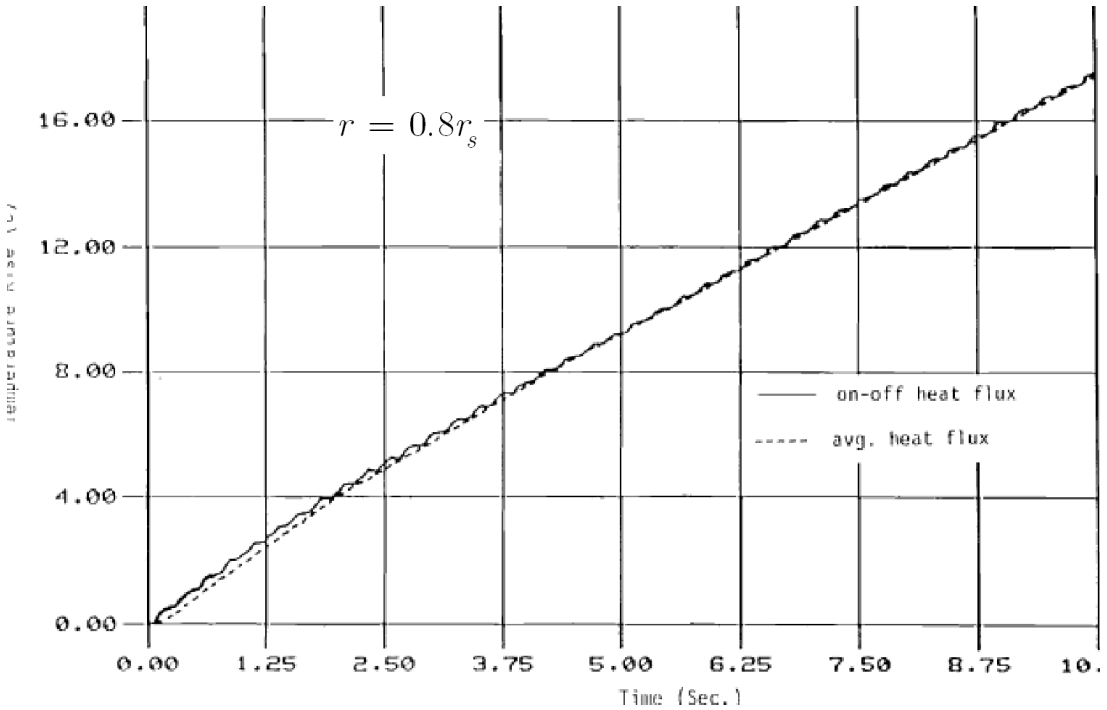

Figure 53. Transient surface temperature rise at $r = 0.8r_s$ [6].

Chapter 8. Application to the Pin-Bushing Problem

In the pin-bushing configuration, we consider an elastic cylindrical pin of radius r_s, pressed by an applied load w_a against the bounding inner wall of an annular bushing of inner radius r_b and length L_c, while rotating at a given angular velocity $\dot{\phi}(t)$ around its axis. The bushing is seated within a housing whose outer surface is exposed to surrounding heat transfer conditions, see Figure 54. As a result of the applied load, a contact region S_c is formed with half-angle of contact α, and a normal traction $p_c(\theta,t)$ develops at the interface. Coulomb friction is assumed throughout the analysis, $\tau_c = \mu_c p_c(\theta,t)$, during the sliding phase. As a result of sliding friction within the contact region, heat is generated, leading to surface temperature rise emanating at the contact interface. It is assumed that all parts materials are elastic, isotropic and thermally conducting.

In the modeling of the pin-bushing joint, it is assumed that either the pin or housing can rotate at constant or oscillatory speed. Brief descriptions of the motion profile were given earlier for both oscillatory and harmonic and unidirectional motion, see Figures 25-27. Some details are presented next in the realm of the pin-bushing joint. Only the thermal problem is considered in order to study the effects of key parameters on the surface temperature rise. The heat flux computation relies on classic contact model solutions, which are described in this chapter.

Constant Speed Motion

For a constant-speed oscillation, the velocity and position functions may be expressed over one period interval as:

$$\dot{\phi} = \pm\omega,\ \phi = \phi_0 \pm \omega t :: 0 \le t \le \mathrm{T} \tag{75a}$$

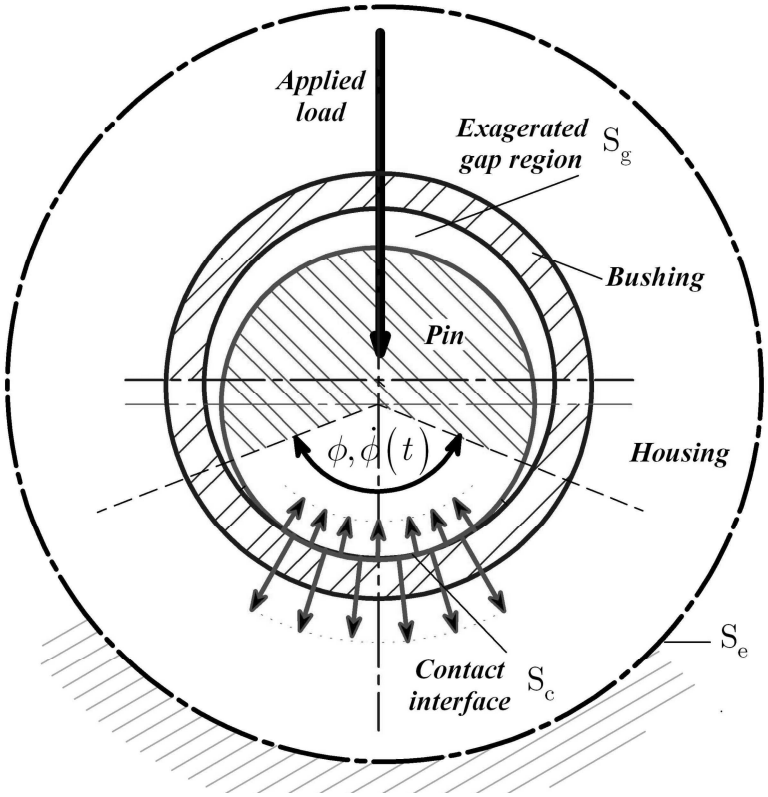

Figure 54. Schematic of the pin-bushing problem.

The rotational speed is $\omega = 2\pi \mathrm{N}/60$ where N is a specified rotational speed in rpm for constant speed oscillation. The position and speed amplitudes are related to the period as follows:

$$\omega \mathrm{T} = 4\phi_m \tag{75b}$$

Thus, $\phi - \phi_0 = \phi_m \Phi(\omega t)$ where after using (75b),

$$\Phi(\omega t) = \pm\left(\omega/\phi_m\right) t \;::\; 0 \le t \le \mathrm{T} \tag{75c}$$

The frequency of oscillation is given by the familiar relation:

$$\omega = 2\pi/\mathrm{T} = \left(\pi/2\right)\left(\omega/\phi_m\right). \tag{75d}$$

For instance, the velocity and position functions may be defined on the time interval $0 \le \omega t \le 2\pi$ by

$$\dot{\phi} = \omega \begin{cases} 1 & 0 \le \omega t \le \pi/2 \\ -1 & \pi/2 \le \omega t \le 3\pi/2 \\ 1 & 3\pi/2 \le \omega t \le 2\pi \end{cases} \tag{75e}$$

$$\phi - \phi_0 = \phi_m \begin{cases} 0 + \left(\omega/\phi_m\right)t & 0 \le \omega t \le \pi/2 \\ 2 - \left(\omega/\phi_m\right)t & \pi/2 \le \omega t \le 3\pi/2 \\ -4 + \left(\omega/\phi_m\right)t & 3\pi/2 \le \omega t \le 2\pi \end{cases} \tag{75f}$$

Therefore,

$$\Phi\left(\omega t\right) = \begin{cases} 0 + \left(\omega/\phi_m\right)t & 0 \le \omega t \le \pi/2 \\ 2 - \left(\omega/\phi_m\right)t & \pi/2 \le \omega t \le 3\pi/2 \\ -4 + \left(\omega/\phi_m\right)t & 3\pi/2 \le \omega t \le 2\pi \end{cases} \tag{75g}$$

$$\dot{\Phi}\left(\omega t\right) = 1/\phi_m \begin{cases} 1 & 0 \le \omega t \le \pi/2 \\ -1 & \pi/2 \le \omega t \le 3\pi/2 \\ 1 & 3\pi/2 \le \omega t \le 2\pi \end{cases} \tag{75h}$$

Harmonic Speed Motion

For a harmonic motion, the amplitude and frequency are specified. Assuming a sinusoidal time function, $\Phi\left(\omega t\right) = \sin(\omega t)$, we may write:

$$\phi - \phi_0 = \phi_m \Phi(\omega t) = \phi_m \sin(\omega t) \tag{76a}$$

$$\dot{\phi} = d\phi/dt = \phi_m \omega \, d\Phi/d(\omega t) = \omega \phi_m \dot{\Phi}(\omega t) = \phi_m \omega \cos(\omega t) \tag{76b}$$

$$\omega = 2\pi/\mathrm{T} \tag{76c}$$

If it is desired that both square and harmonic motions have the same amplitude and period, then set equal periods to we obtain the equivalent harmonic frequency in terms of constant speed parameters. Recall that for constant speed motion, (75b) gives:

$$\mathrm{T} = 4\phi_m/\omega_c \tag{76d}$$

Thus,

$$2\pi/\omega_h = 4\phi_m/\omega_c \rightarrow \omega_h = 2\pi\omega_c/(4\phi_m) \tag{76e}$$

Thus, for an equivalent harmonic position of same amplitude and period, the constant velocity must be lower than the harmonic velocity amplitude by a factor of $\pi/2$, as seen from Equation (76e). In this case, the harmonic position function circumscribes the triangular position function, but the velocity amplitudes are related by (76e), see Figures 55-56. This relationship also ensures the same mean heat input per cycle.

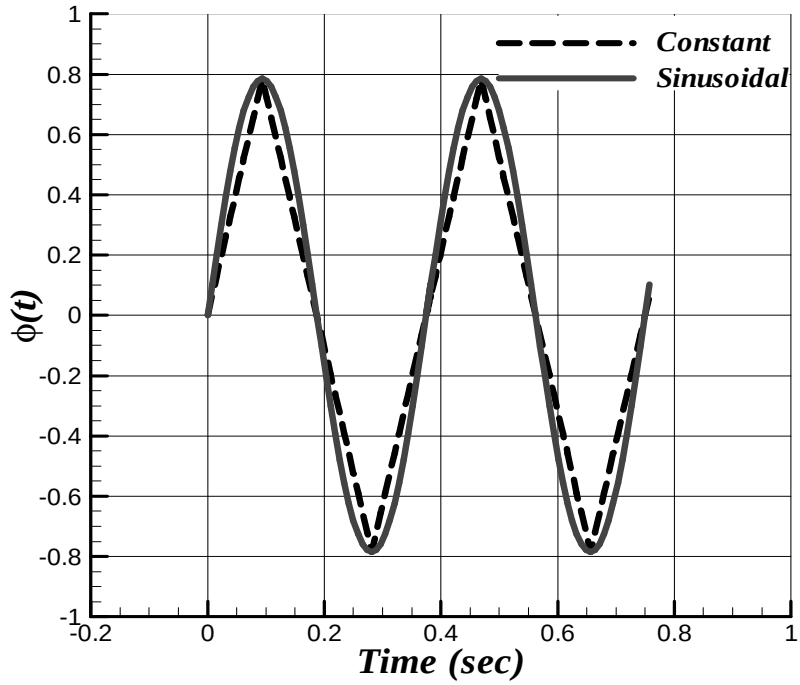

Figure 55. Constant versus sinusoidal rotational motion - angular position.

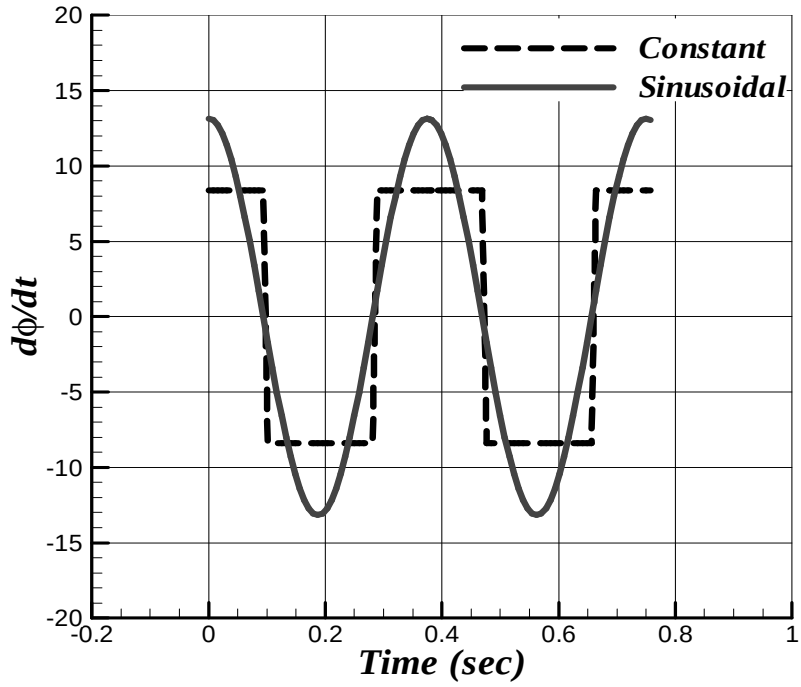

Figure 56. Constant versus sinusoidal rotational motion - angular speed.

Governing Equations

The equations governing the temperature change have been given earlier for a general configuration. They are rewritten here with the reference parameters defined in Table 2.

Table 2. Reference parameters for pin-bushing

Reference time	$t_r = 1/\omega$ (ω = rotational frequency)
Reference length	$s_r = r_s$ (pin radius)
Reference heat transfer coefficient	$h_r = h_e$ (surroundings)
Reference pressure	$p_r = p_l = w_a/(2r_sL_c)$ (projected load)
Reference speed	$v_r = r_s\omega$ (maximum value)

The temperature field $T\left(t,\mathbf{r}\right)$ in the conducting media (pin, bushing, housing), assumed to be a function of time and coordinates, is governed, in Cartesian coordinates, by the following equation:

$$\rho c\frac{\partial T}{\partial t}+m\rho c\mathbf{v}\bullet\nabla T=\nabla\bullet\left(k\nabla T\right)+q_b\left(\mathbf{r},T\right),\ t>0\,,\ \mathbf{r}=\left(x,y\right) \tag{77a}$$

where $\mathbf{v}=\dot{\phi}(t)\begin{bmatrix}-y & x\end{bmatrix}^T$ is the sliding velocity vector. In polar cylindrical coordinates the governing equation reads:

$$\rho c\frac{\partial T}{\partial t}+m\rho c\dot{\phi}(t)\frac{\partial T}{\partial\theta}=\nabla\bullet\left(k\nabla T\right)+q_b\left(\mathbf{r},T\right),\ t>0\,,\ \mathbf{r}=\left(r,\theta\right) \tag{77b}$$

The source term $q_b\left(\mathbf{r},T\right)$ was described earlier in the general formulation.

Boundary Conditions

The boundary conditions involve mixed heating due to friction and convection at the sliding interface, and convective cooling at the surface of the housing exposed to the surrounding air. In addition the coupling condition of temperature continuity is enforced at the contact interface. Convective heat transfer coefficients with the surroundings and within the gap interface are estimated using known empirical relations [38]. At the gap interface both convection and radiation heat exchange, between the walls, are considered. On the surface of the housing exposed to the surroundings, the boundary condition is:

$$k\frac{\partial T}{\partial n}+h_e(T-T_e)=0\ \text{on}\ \mathrm{S_e} \tag{78}$$

At the sliding interface, the mixed boundary condition is

$$k\frac{\partial T}{\partial n}+h\Delta T=q\ \text{on interface}\ \mathrm{S_c}\cup\mathrm{S_g} \tag{79}$$

where ΔT is the local temperature difference of the two surfaces. The frictional heat flux input q_c and convective heat transfer coefficient h are defined over the interface as follows:

$$q = \begin{cases} \mu_c p_c(\theta)\left|v\right| & \text{on } \mathrm{S_c} \\ 0 & \text{on } \mathrm{S_g} \end{cases} \tag{80}$$

$$h = \begin{cases} 0 & \text{on } \mathrm{S_c} \\ h_g(T,\theta) & \text{on } \mathrm{S_g} \end{cases} \tag{81}$$

where p_c is the contact pressure, and v is the linear sliding speed given by:

$$v(t) = r_s\dot{\phi}(t) = v_m\phi_m\dot{\Phi}(\omega t) \tag{82}$$

where $v_m = r_s\omega$ is the maximum linear sliding speed for harmonic motion. The gap heat transfer coefficient $h_g(T,\theta)$ represents the effects of convection and radiation at the interface, and estimated using empirical relations for a cylinder. Continuity of the solution field will be enforced at contact points.

Dimensionless Equations

We now normalize the problem and develop the relevant dimensionless equations. Using the above reference parameters, we define the dimensionless time and space variables conveniently as follows:

$$\tau = \omega t\,,\ x = r_s X,\ y = r_s Y,\ z = r_s Z \tag{83}$$

The above transformation of time and space allows both time periods and the polar coordinate to be normalized to within a value of 2π, and the contact interface to be at a unit radius. Based on (83), the resulting reference speed is $v_r = v_m$. That is, the velocity is normalized with respect to its maximum value at the contact interface. Recalling (76), we have

$$\dot{\phi} = \omega\phi_m\dot{\Phi}\left(\tau\right),\ v = r_s\dot{\phi}\left(t\right) = v_m\phi_m\dot{\Phi}\left(\tau\right) \tag{84a}$$

The dimensionless sliding velocity is given by:

$$V(\tau) = \frac{v}{v_m} = \frac{\dot{\phi}}{\omega} = \phi_m \dot{\Phi}(\tau) \tag{84b}$$

The dimensionless contact pressure and heat flux are given by:

$$p_c = p_l P_c \tag{85}$$

$$q_c = q_r Q_c,\ q_r = p_l v_m \tag{86}$$

The dimensionless temperature rise is given by:

$$\Theta = h_e \Delta T \big/ q_r \tag{87}$$

The dimensionless boundary condition at the sliding interface reads:

$$K\frac{\partial \Theta}{\partial n} + Bi\Delta\Theta = Bi_e Q :: \text{on } \mathrm{S_c} \cup \mathrm{S_g} \tag{88}$$

$$K = k \big/ k_r,\ Bi = h r_s \big/ k_r,\ Bi_e = h_e r_s \big/ k_r \tag{89}$$

where the reference thermal conductivity is that of the moving part. The dimensionless heating and cooling fluxes at the interface are described by

$$Q = \begin{cases} Q_c & \left|\theta - \phi_c\right| \le \alpha \\ 0 & Otherwise \end{cases},\ B_i = \begin{cases} 0 & \left|\theta - \phi_c\right| \le \alpha \\ B_{ig} & Otherwise \end{cases} \tag{90a}$$

$$Q_c = q_c \big/ q_r = \mu_c P_c \left|V(\tau)\right|,\ Bi_g = h_g r_s \big/ k_r \tag{90b}$$

$$\hat{\lambda}_i = \frac{1}{2\pi\alpha}\int_0^{2\pi}\int_0^{2\pi}\left|\frac{Q_i}{Q_c}\right| d\tau d\theta,\quad i = 1,2 \tag{91}$$

The heat equation in dimensionless form is:

$$P_e \frac{K}{\Lambda}\frac{\partial \Theta}{\partial \tau} + mP_e \frac{K}{\Lambda}\phi_m \dot{\Phi}\left(\tau\right)\frac{\partial \Theta}{\partial \theta} = \nabla\bullet\left(K\nabla\Theta\right) + B_{ie}Q_b \tag{92}$$

where

$$Q_b = \frac{r_s q_b}{q_r} = -\frac{2h_e r_s}{L q_r}\Delta T = -\frac{L_r}{A_r}\Theta \tag{93}$$

$$\Lambda = \kappa \big/ \kappa_r \,,\; P_e = r_s^{\,2}\omega \big/ \kappa_r \tag{94}$$

$$A_r = L_c \big/ D \,,\; L_r = L_c \big/ L \tag{95}$$

The length ratios A_r, L_r are the bushing aspect ratio and the length ratio and represent ratios relative to the directions perpendicular to the sliding direction. The dimensionless cooling boundary condition at the outer surface is

$$K\frac{\partial \Theta}{\partial n} + B_{ie}\Theta = 0 \;\; :: \text{on } \mathrm{S_e} \tag{96}$$

Steady State Condition

The steady state surface temperature at the interface is described by the equilibrium of frictional heat generated and heat convected away from the pin and bushing surfaces. In the present study, a steady state condition is assumed once the average value of the maximum surface temperature, computed between consecutive cycles, ceases to change by no more than a given tolerance ε << 1. That is, if τ_n and τ_{n-1} (n > 1) are the current and the previous cycles. That is,

$$\left| \frac{1}{\tau_n}\int_0^{\tau_n} \Theta_{\max}(\tau)d\tau - \frac{1}{\tau_{n-1}}\int_0^{\tau_{n-1}} \Theta_{\max}(\tau)d\tau \right| \le \varepsilon \tag{97a}$$

$$\Theta_{\max}(\tau) = \underset{\theta=0..2\pi}{\mathrm{Max}} \left[\Theta_{(s)}\left(\theta,\tau\right), \Theta_{(b)}\left(\theta,\tau\right) \right] \tag{98a}$$

This condition is used as a stopping criterion for computations. The maximum temperature rise is assumed to occur at the interface of the contacting bodies. Notice that the steady state condition is based on a mean value or a peak value during each cycle. In oscillatory contacts, the temperature at steady state is actually a periodic function of time that oscillates about a constant mean value.

Chapter 9. Line Contact Model

Two classical contact theories are considered in the analysis of the pin-bushing problem. The Hertzian and conformal contact theories for line contact. The Hertzian line contact theory was used in a first attempt to solve the problem. However, the conformal contact theory is thought to represent the pin-bushing cylindrical contact more accurately.

Hertzian Line Contact Solution

The Hertzian contact pressure for line contact, idealized in Figure 57, is given by Khonsari and Hua [39]

$$p_c = p_m \sqrt{1 - \frac{x'^2}{a^2}} :: -a \le x' \le a \tag{99}$$

where p_m is the maximum Hertzian line contact pressure, and a is the line contact radius, defined as

$$p_m = \sqrt{\frac{w_a E_c}{\pi L_c r_c}},\ a = \sqrt{\frac{4 W_a r_c}{\pi E_c L_c}} \tag{100}$$

where r_c, E_c are the relative radius of curvature and the effective elasticity modulus, respectively, defined by

$$1/r_c = 1/r_s - 1/r_b\,, \tag{101}$$

$$1/E_c = \left(1 - \nu_s^{\,2}\right)/E_s + \left(1 - \nu_b^{\,2}\right)/E_b \tag{102}$$

The mean Hertzian contact pressure for line contact is given by

$$p_a = \frac{w_a}{2 a L_c} = \frac{\pi}{4} p_m. \tag{103}$$

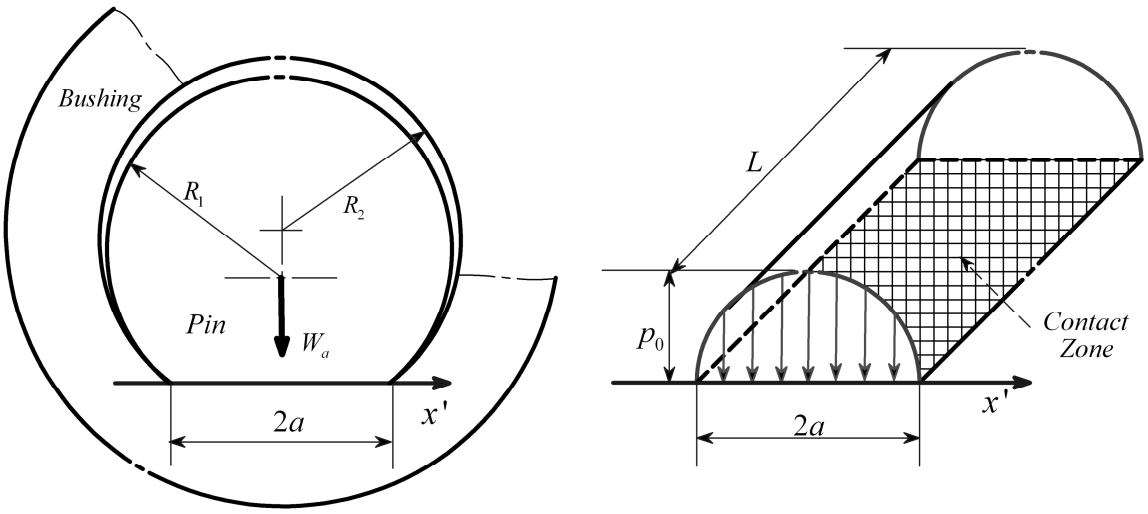

Figure 57. Idealized Hertzian line contact.

Define the dimensionless relative contact radius of curvature, $R_c = r_c / r_s$, and the dimensionless semi-contact width, $\alpha = a / r_s$. Note that the dimensionless relative contact radius of curvature may be expressed in terms of the clearance ratio, $C_r = C / r_s$, as follows:

$$R_c = r_c / r_s = \left(1 + C_r\right) / C_r \tag{104}$$

The contact coordinate x', shown in Figure 57, may be written in terms of polar angle and center of oscillation as

$$x' = r_s \left(\theta - \theta_c\right) \tag{105}$$

where θ is the polar angle, and θ_c is the center of the oscillation span. Therefore, equations (99)–(100) become:

$$p_c = p_m \sqrt{1 - \left(\frac{\theta - \theta_c}{\alpha}\right)^2} \tag{106a}$$

$$p_m = \sqrt{p_l\left(\frac{2E_c}{\pi}\right)\frac{C_r}{1+C_r}}, \tag{106b}$$

$$\alpha = \sqrt{p_l\left(\frac{8}{\pi E_c}\right)\frac{1+C_r}{C_r}}, \tag{106c}$$

Using (103), the mean contact pressure expression becomes

$$p_a = \frac{p_l}{\alpha} = \frac{\pi}{4}p_m \tag{107}$$

Taking the ratio of the two equations in (106-b,c) gives an alternate definition of the maximum contact pressure:

$$p_m = \left(\frac{E_c}{2}\right)\frac{C_r\alpha}{1+C_r} \tag{108}$$

Substituting (108) into the first of (106b) gives the following relationship:

$$\frac{2p_l}{E_c} = \frac{\pi}{4}\frac{C_r\alpha^2}{1+C_r} \tag{109}$$

This is a design relation that combines the elastic material properties, the projected load, the clearance ratio, and the dimensionless contact width. The dimensionless maximum and mean contact pressures are obtained directly using (106b) and (107):

$$P_m = \frac{p_m}{p_l} = \sqrt{\left(\frac{2}{\pi}\right)\left(\frac{E_c}{p_l}\right)\frac{C_r}{1+C_r}},\ P_a = \frac{p_a}{p_l} = \frac{1}{\alpha} = \frac{\pi}{4}P_m \tag{110}$$

An alternate form of the dimensionless maximum contact pressure can be written, based on equation (108), as follows:

$$P_m = \left(\frac{E_c}{2p_l}\right)\frac{C_r\alpha}{1+C_r} \tag{111}$$

Using (106a) and (111), the dimensionless Hertzian pressure is:

$$P_c = \frac{p_c}{p_l} = P_m\sqrt{1-\left(\frac{\theta-\theta_c}{\alpha}\right)^2} = \left(\frac{E_c}{2p_l}\right)\frac{C_r\alpha}{1+C_r}\sqrt{1-\left(\frac{\theta-\theta_c}{\alpha}\right)^2} \tag{112}$$

Note that the Hertzian formula for the contact pressure is based on an applied load line passing through the contact center where $\phi = \theta_c$. However, if the bushing is the moving part the component of load changes with the position of the contact. From geometry, the effective normal load varies with the contact position as follows

$$w_e(t) = w_a\left|\cos\left(\phi-\theta_c\right)\right| = w_a\left|\cos\left(\phi_m\Phi\right)\right| \tag{113}$$

The effective frictional stress and heat flux at any contact position must be computed based on this effective normal component of the load. Recalling that the linear sliding speed as a function of time is $v(t) = r_s\dot{\phi} = v_m\phi_m\dot{\Phi}(\omega t)$, the frictional heat flux distribution is given by

$$q_c = \mu_c v p_c = \mu_c p_l P_m\sqrt{1-\left(\frac{\theta-\theta_c}{\alpha}\right)^2}\, v_m\phi_m\left|\dot{\Phi}\right|\left|\cos\left(\phi_m\Phi\right)\right| = q_r Q_c \tag{114a}$$

where the reference heat flux and the dimensionless heat flux distribution are defined as:

$$q_r = p_l v_m \tag{114b}$$

$$Q_c = \mu_c\left(\frac{E_c}{2p_l}\right)\frac{C_r\alpha}{1+C_r}\sqrt{1-\left(\frac{\theta-\theta_c}{\alpha}\right)^2}\,\phi_m\left|\dot{\Phi}\right|\left|\cos\left(\phi_m\Phi\right)\right| \tag{114c}$$

Note that the dimensionless contact pressure and heat flux may also be written as follows:

$$P_c = \frac{4}{\pi\alpha}\sqrt{1-\left(\frac{\theta-\theta_c}{\alpha}\right)^2},\ Q_c = \mu_c\sqrt{1-\left(\frac{\theta-\theta_c}{\alpha}\right)^2}\,\frac{4\phi_m}{\pi\alpha}\left|\dot{\Phi}\right|\left|\cos\left(\phi_m\Phi\right)\right| \tag{115}$$

In Equation (115), the ratio of the amplitude to the contact width, $\beta = \phi_m\big/\alpha$, shows up explicitly as a pertinent dimensionless design parameter [16]. In this chapter, the heat flux is

computed using (114) and the dimensionless semi-contact α width is selected as an independent input parameter in place of the ratio β. The β-ratio effect is derived from other results.

Based on the thermal problem formulation and the boundary conditions in dimensionless form using the Hertzian line contact theory, if the material properties are constant, then the dimensionless surface temperature rise may be characterized by four independent dimensionless operating parameters; they are: the Peclet number P_e, the Biot number at the interface B_{ig}, the dimensionless oscillation amplitude ϕ_m, and the dimensionless semi-contact angle α. The functional form of the normalized temperature rise and the normalized heating and cooling flux at the interface is:

$$\Theta = \Theta\left(\theta, \phi, P_e, B_i, \phi_m, \alpha\right) \tag{116a}$$

$$Q = q/q_r = \begin{cases} B_{ie} Q_c(\theta, \phi, \phi_m, \alpha) & \text{on } \mathrm{S_c} \\ -B_i \Delta\Theta\left(\theta, \phi, P_e, B_{ig}, \phi_m, \alpha\right) & \text{on } \mathrm{S_g} \end{cases} :: 0 \le \theta \le 2\pi \tag{116b}$$

The results for surface temperatures obtained from such a dimensionless model are applicable to pin-bushing joints with a wide range of sizes and applied loads according to Equation (109) and within the selected operating range of the dimensionless input parameters considered in the numerical solution.

Conformal Line Contact Solution

When the contact surfaces are curved and closely conforming, having contact dimensions nearly equal to their radii, the Hertzian analysis is no longer valid. The surfaces make contact over an area whose size is comparable with the significant dimensions of the two bodies; the contact stresses then become part of the general stress distribution throughout the bodies and cannot be separated from it. Therefore, some of the assumptions made in Hertzian analysis no longer apply and alternative solutions must be found. According to Johnson [40], the contact between

conforming solids cannot be represented well by a solution in half spaces. This is due to the large contact width. In the case of a pin-bushing assembly, the contact arc subtends an angle $\pm\alpha$ this is not small; see Figure 58.

The solution to the problem of the conformal contact of a long elastic cylinder contacting the inner wall of a cylindrical bushing was first attempted by Steuermann. He represented the gap between the cylinder and cylindrical seat by a power series and formulated the displacements in terms of integrals of the line influence functions. He used finite difference methods to solve the integral equation for the contact pressure distribution. This approach is more accurate than the classic solution of Hertz because higher-order terms in the description of the profile are taken into consideration. A widely accepted standard for the analytical study of conformal contact of cylindrical bodies was conducted and confirmed experimentally by Persson [41].

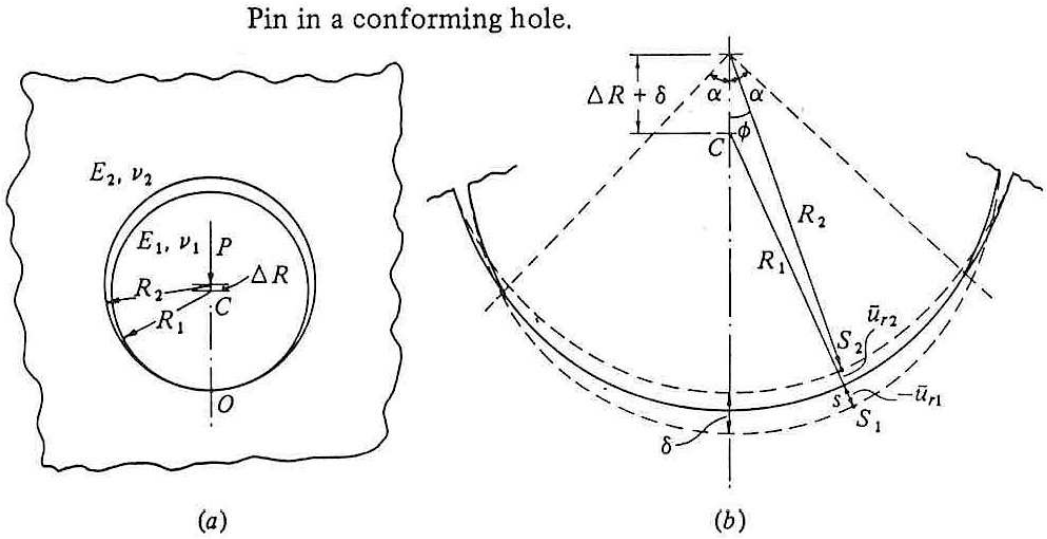

ΔR = clearance, P = Load per unit length.

Figure 58. Conformal line contact for a pin in an annular bushing. [40]

Persson derived a contact criterion identical with that of Steuermann but proceeded to solve the equation in a different way. He assumed that the contact surface was cylindrical and

formulated the contact criterion as an integral-differential equation from which he determined the analytical contact pressure distribution for a plane stress model; i.e., the analysis pertains to a circular disc in a circular hole in an infinite thin plate. Persson derived an analytical solution to the problem of a loaded disc interfaced with a circular hole in an infinite plate. A small clearance was assumed. The solution is applicable to plane stress and contacting bodies with identical materials. Figure 59, taken from the book by Johnson [40], shows a comparison between the three theories.

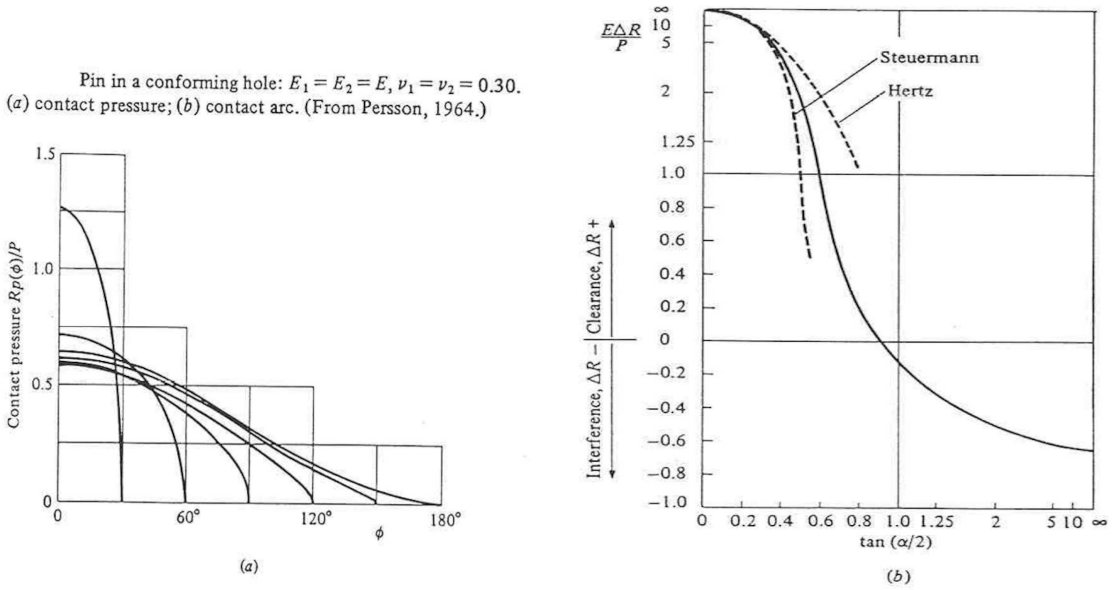

ΔR = clearance, P = Load per unit length.

Figure 59. Comparison of three classic contact theories.[40]

Hou and Hills [42] extended the theory to conformal contact of dissimilar materials and derived the necessary equations in terms of material property ratio between the Young's modulus of the contacting bodies. The resulting pressure distribution $p_c(\bullet)$ and contact half-width α are given in terms of transformed variables (ξ, β) by the following relations:

$$\frac{r_b p_c\left(\xi\right)}{2r_s p_l} = \frac{2\sqrt{\beta^2-\xi^2}}{\pi\sqrt{1+\beta^2}\left(1+\xi^2\right)} + \frac{f_c(\beta,\xi)}{2\pi\beta^2\left(1+\beta^2\right)} \tag{117}$$

$$f_c(\beta,\xi) = \ln\left[\frac{\sqrt{1+\beta^2}+\sqrt{\beta^2-\xi^2}}{\sqrt{1+\beta^2}-\sqrt{\beta^2-\xi^2}}\right] \tag{118}$$

$$\frac{2\beta^4+2\beta^2-1}{\beta^2\left(\beta^2+1\right)} = g_c\left(\beta\right) \tag{119}$$

$$g_c\left(\beta\right) = \frac{2\left(1+E_p\right)-\nu_p E_p}{1+E_p} - \frac{\pi E_1 C}{D p_l\left(1+E_p\right)} + \frac{2}{1+E_p}\frac{r_b}{2r_s p_l}\int_{-\beta}^{\beta}\frac{p_c\left(\xi\right)d\xi}{1+\xi^2} \tag{120}$$

The contact half-angle α and the polar angle θ are related to the above transformed variables as follows:

$$\beta = \tan\left(\alpha/2\right),\ \xi = \tan\left(\theta/2\right),\ -\beta \le \xi \le \beta \tag{121}$$

In the above equations the projected load was defined is $p_l = w_a/\left(2r_s L_c\right)$, and elastic material parameters are introduced as:

$$E_p = E/E_r\ ,\ \nu_p = 1-\nu_1-\left(\frac{1-\nu_2}{E_p}\right) \tag{122}$$

Equations (117) and (118) give the contact pressure profile on the inner wall $r_b = r_s + C$ of the bushing, while Equation (119) and (120) provide the necessary equations to compute the contact width. The formulation by Hou and Hills [42] was based on the assumption of small clearance and compatibility relations of the radial displacement and strain at the interface of the pin and the hole. Moreover, the formulation is valid only within the elastic state. Notice that the pressure profile given by (117) and (118) is independent of the combination of elastic material properties. On the other hand, the contact extent is greatly influenced by the material parameters as seen from equation (119) and (120). In contrast to the classical Hertz

theory, material mismatch between the contacting bodies leads to different contact width in conformal contacts.

The dimensionless contact parameters are given by the following set of dimensionless equations based on conformal contact theory.

$$P_c = \frac{2}{\left(1+C_r\right)}\left[\frac{2\sqrt{\beta^2-\xi^2}}{\pi\sqrt{1+\beta^2}\left(1+\xi^2\right)}+\frac{f_c(\beta,\xi)}{2\pi\beta^2\left(1+\beta^2\right)}\right] \tag{123}$$

$$f_c(\beta,\xi) = \ln\left[\frac{\sqrt{1+\beta^2}+\sqrt{\beta^2-\xi^2}}{\sqrt{1+\beta^2}-\sqrt{\beta^2-\xi^2}}\right] \tag{124}$$

$$\frac{2\beta^4+2\beta^2-1}{\beta^2\left(\beta^2+1\right)} = g_c\left(\beta\right) \tag{125}$$

$$g_c\left(\beta\right) = \frac{2\left(1+E_p\right)-\nu_p E_p}{1+E_p} - \frac{\pi M_s C_r}{2\left(1+E_p\right)} + \frac{2}{1+E_p}\frac{\left(1+C_r\right)}{2}\int_{-\beta}^{\beta}\frac{P_c\left(\xi\right)d\xi}{1+\xi^2} \tag{126}$$

The dimensionless modulus of elasticity M_s of the pin is defined as: $E_s = p_l M_s$. The frictional heat flux distribution is given by

$$q_c = \mu_c v p_c = \mu_c p_l v_m P_c \phi_m \left|\dot{\Phi}\right|\left|\cos\left(\phi_m\Phi\right)\right| = q_r Q_c \tag{127a}$$

where

$$q_r = p_l v_m \tag{127b}$$

$$Q_c = \mu_c \frac{2}{\left(1+C_r\right)}\left[\frac{2\sqrt{\beta^2-\xi^2}}{\pi\sqrt{1+\beta^2}\left(1+\xi^2\right)}+\frac{f_c(\beta,\xi)}{2\pi\beta^2\left(1+\beta^2\right)}\right]\phi_m\left|\dot{\Phi}\right|\left|\cos\left(\phi_m\Phi\right)\right| \tag{127c}$$

Based on this formulation of the contact model, using the conformal line contact theory, the dimensionless surface temperature rise may be characterized by the same dimensionless operating parameters that were described using the Hertzian contact solution under the same set of conditions and assumptions. It is noteworthy that if no restrictions are made on the material properties, geometry, and operating conditions, then there are many pertinent bulk parameters, considered independent, that influence the surface temperature rise, based on either of the contact models that were described. A complete analysis of the surface temperature rise must necessarily consider a mixed set of dimensionless and dimensional key parameters if they are to be specified independently. In the following chapter, an analysis of the surface temperature rise is carried out using the Hertzian contact model. Computations and analysis based on the conformal contact model will be presented in subsequent chapters.

Chapter 10 – Simulation and Analysis of Surface Temperature in Oscillatory Sliding Line Contact in Pin-Bushing Joints

In this chapter, a series of results is presented for the effect of dimensionless parameters P_e, B_i, ϕ_m, α on the maximum steady state dimensionless surface temperature rise [43]. In this initial attempt to study the surface temperature in a pin-bushing pair, a simplified model is considered by ignoring the housing and axial effects. The outer surface of the bushing is now assumed to be exposed to the surroundings with a convective cooling boundary condition. Constant velocity oscillatory motion is considered, and the bushing is the moving part in this study. Thus the heat flux is moving with respect to the pin. The finite difference method is used to discretize the thermal problem and associated boundary conditions. The ambient Biot number and clearance ratio are assumed to be fixed at B_{ie} = 0.01954, C_r = 5 x 10^{-3}. Simulations are carried out by varying one independent parameter at a time. Table 3 shows the range of dimensionless input data considered in simulations. The first two columns show the range of values for each independent parameter. The fixed parameter values are indicated in the third column of Table 3.

Table 3. Dimensionless input parameters.

	Low	High	Fixed
P_e	π/100	40π	6π
B_i / B_{ie}	0	2	1/5
ϕ_m	π/96	π/3	π/6
α	π/24	π/3	π/12

The displacement of oscillation $\phi(\omega t)$ that locates the center of the moving frictional heat flux is measured from the position $\theta_c = 3\pi/2$ of the coordinate system. It is assumed that the initial position of the heat flux is $\phi_0 = \theta_c$. Plots of the angular displacement $\phi(\omega t)$ and dimensionless speed $V = \phi_m \dot{\Phi}(\omega t)$ versus dimensionless time are shown in Figure 60 for two oscillation cycles. A plot of the dimensionless heat flux is shown in Figure 61.

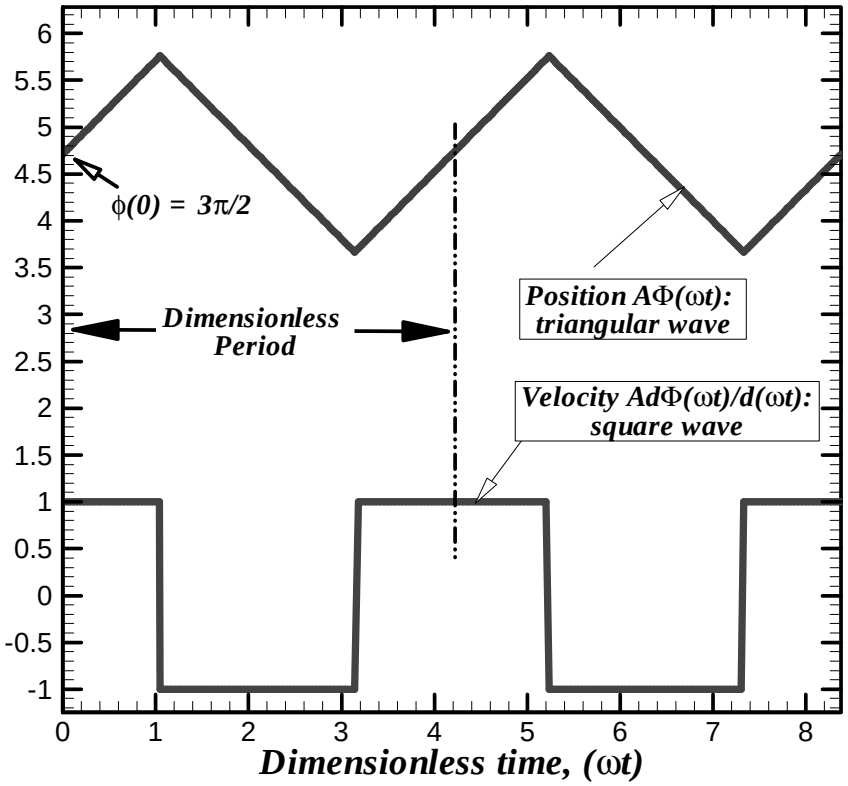

Figure 60. Dimensionless motion: (ϕ_m = π/3, ϕ_c = 3π/2).

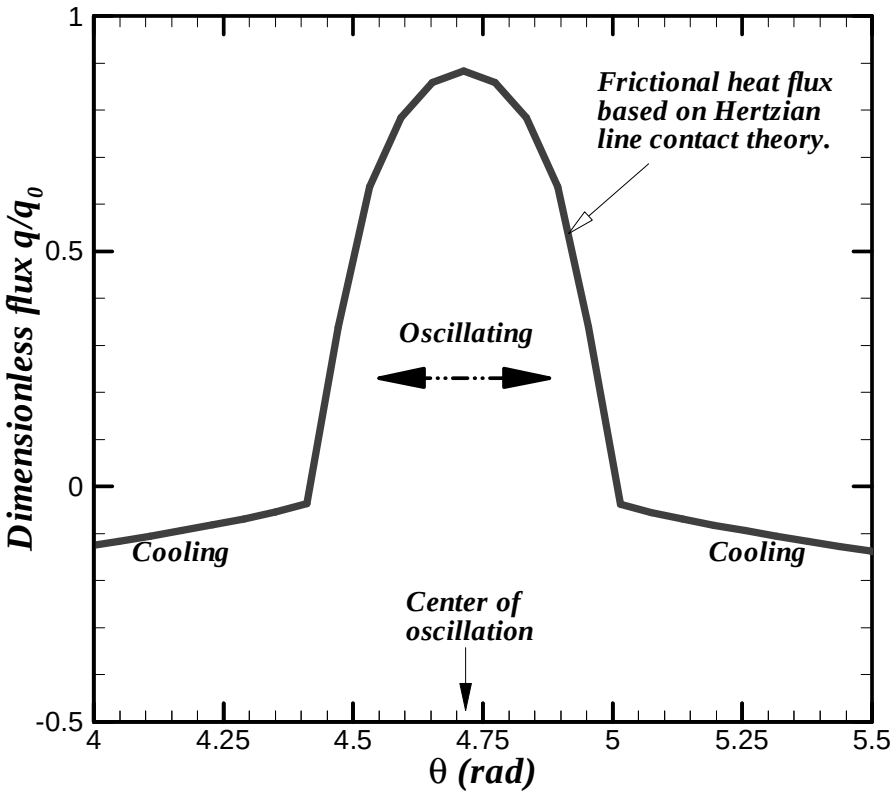

Figure 61. Dimensionless heat flux: ($B_i = B_{ie}$, $\phi_m = \pi/3$, $\alpha = \pi/12$, $\phi_c = 3\pi/2$.).

The Finite-Difference Method

The spatial derivatives in polar coordinates (r,θ) are discretized to reduce the partial differential equations (PDEs) into a set of ordinary differential equations (ODEs) in time. The thermal dimensionless material properties and convective velocity will be denoted K, D, C and $V(\tau)$, respectively. The spatial derivatives of the dimensionless temperature rise, in the two dimensional PDEs are approximated, at the internal grid points as follows [44]:

$$\left[\frac{1}{r}\frac{\partial}{\partial r}\left(rK\frac{\partial \Theta}{\partial r}\right)\right]_P \approx \frac{1}{r_P \Delta r_P}\left[r_n K_n \frac{\Theta_N(t)-\Theta_P(t)}{\Delta r_n} - r_s K_s \frac{\Theta_P(\tau)-\Theta_S(\tau)}{\Delta r_s}\right] \tag{128a}$$

$$\left[\frac{1}{r}\frac{\partial}{\partial\theta}\left(\frac{K}{r}\frac{\partial\Theta}{\partial\theta}\right)\right]_P \approx \frac{1}{r_P\Delta\theta_P}\left[\frac{K_e}{r_P}\frac{\Theta_E(\tau)-\Theta_P(\tau)}{\Delta\theta_e}-\frac{K_w}{r_P}\frac{\Theta_P(\tau)-\Theta_W(\tau)}{\Delta\theta_w}\right] \tag{128b}$$

where node *P* is the solution point, *E, W, N, S* denote the nodes to the east, west, north and south of node *P*, and e, *w, n, s* denote interpolation points at the halfway borders from node *P*. Central differencing was applied to the first derivatives at the halfway boundaries of all internal nodes to get the complete formula. Upwinding is applied to properly approximate the convective-terms:

$$\left[DCV\frac{\partial\Theta}{\partial\theta}\right]_P \approx \left[\!\left[DCV(\tau),0\right]\!\right]\left(\frac{\Theta_P(\tau)-\Theta_W(\tau)}{\Delta\theta_w}\right)-\left[\!\left[-DCV(\tau),0\right]\!\right]\left(\frac{\Theta_E(\tau)-\Theta_P(\tau)}{\Delta\theta_e}\right) \tag{129a}$$

where

$$\left[\!\left[\pm DCV\left(\tau\right),0\right]\!\right] = Max\left(\pm DCV\left(\tau\right),0\right) \tag{129b}$$

Discretization at the boundaries and interface are also formulated similarly. The bracketed notation $\left[\!\left[\bullet\right]\!\right]$ in Equation (129) is used to indicate that field value at an interface, upstream or downstream to the solution point, is equal to the field value at the grid point on the upwind side of the interface [44]. Upwinding is essential to improve numerical stability when convective terms are present and the speed (the Peclet number) is high. Mathematically, upwinding is equivalent to adding a diffusive term into the PDE, thus introducing artificial viscosity that serves to suppress numerical oscillation. The difference approximations reduce the PDEs in $\Theta(r,\theta,\tau)$ to a set of ODEs in $\Theta_P\left(t\right)$ (function of time only). Integration of the reduced ODEs is carried out using a fifth order Runge-Kutta scheme, with adaptive time stepping. This method is capable of solving the general ODE in the form

$$d\Theta_{i,j}(\tau)\big/d\tau = \mathrm{f}\left(\Theta_{i,j}\left(\bullet\right),\tau\right),\ t>0\text{, given }\Theta_{i,j}\left(\tau=0\right) \tag{130}$$

The function $\mathrm{f}\left(T_{i,j},t\right)$ can be nonlinear, and may include sign-switching terms, such as found in process models with oscillating motion. Time stepping allows for a minimum of four time steps per quarter cycle, and for the sweep interval to be at most 1/3 of the semi-contact width, whichever is smaller. The contact zone is discretized with enough grid points to represent the parabolic Hertzian profile accurately. The radial direction is discretized non-uniformly with finer grid near the interface where the temperature gradients are high. Figure 62 shows one of the grid patterns used in simulations. This grid pattern corresponds to the case ϕ_m = π/8, α = π/12. A relative error tolerance of $\varepsilon = 10^{-5}$ is used in solving the transient set of equations.

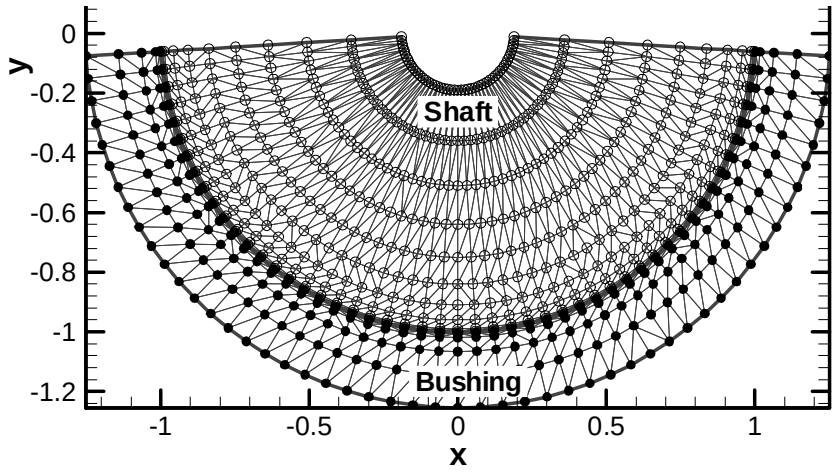

Figure 62. Finite difference grid pattern - ($\phi_m = \pi/8,\ \alpha = \pi/12$).

Effect of the Peclet Number

The effect of the Peclet number on the dimensionless maximum cyclic surface temperature is illustrated in Figure 63 (a). Larger Peclet numbers result in lower steady state dimensionless surface temperatures, but a larger number of cycles are required to reach steady state. The behavior at low Peclet numbers is best revealed on a log-log scale as shown in Figure 63 (b). From inspection of Figure 63 (b), the steady state maximum surface temperature rise is

proportional to P_e^{-n} for $0 < n < 1$, for intermediate to large Peclet numbers. The exponent n depends on the values of the fixed parameters. At low Peclet numbers (< 0.1 as shown), the dimensionless maximum cyclic surface temperature approaches a constant value. This is because the temperature distribution approaches that of a stationary case. At higher Peclet numbers, all heat is convected away in the sliding direction and conduction in the normal direction becomes smaller. This explains why the surface temperature decreases at higher speeds. This behavior is consistent in trend with that reported by Tian et al. [16]. The authors in [16] considered a point heat source moving rectilinearly at a sinusoidal speed, and defined their Peclet number with respect to the contact width. Curve fit relationships for the dimensionless maximum steady state surface temperature rise and the number-of-cycles to steady state are as follows:

$$\Theta_{\max}(P_e) = c_0 + c_1\left(1 + 2c_1^2 c_2 P_e\right)^{-1/2},\ N_c = c_3 + c_4 P_e^{c_5} \tag{131a}$$

c_0 = 0.0398, c_1 = 0.0146, c_2 = 138.31, c_3 = 165, c_4 = 281, c_5 = 0.79 (131b)

These relationships are valid for the fixed parameters $B_i = B_{ie}/5$, $\phi_m = \pi/6$, $\alpha = \pi/12$ ($\beta = \phi_m / \alpha = 2$), and range of Peclet numbers given in Table 3.

Effect of the Biot Number

The effect of the interfacial Biot number on the steady state maximum surface temperature rise is depicted in Figure 64. The Biot number represents the ratio of convection to heat conduction within the gap. The figure reveals that increasing the Biot number results in a reduction in the maximum surface temperature and a decrease in the number of cycles to steady state. For the range of Biot numbers considered here, the reduction in the dimensionless

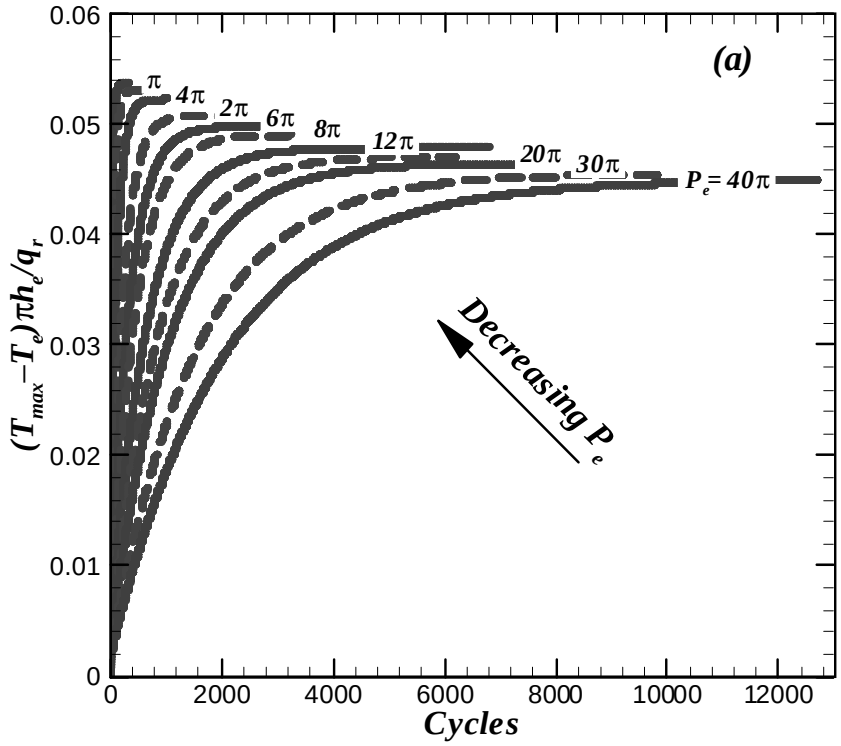

(a) Cyclic variations

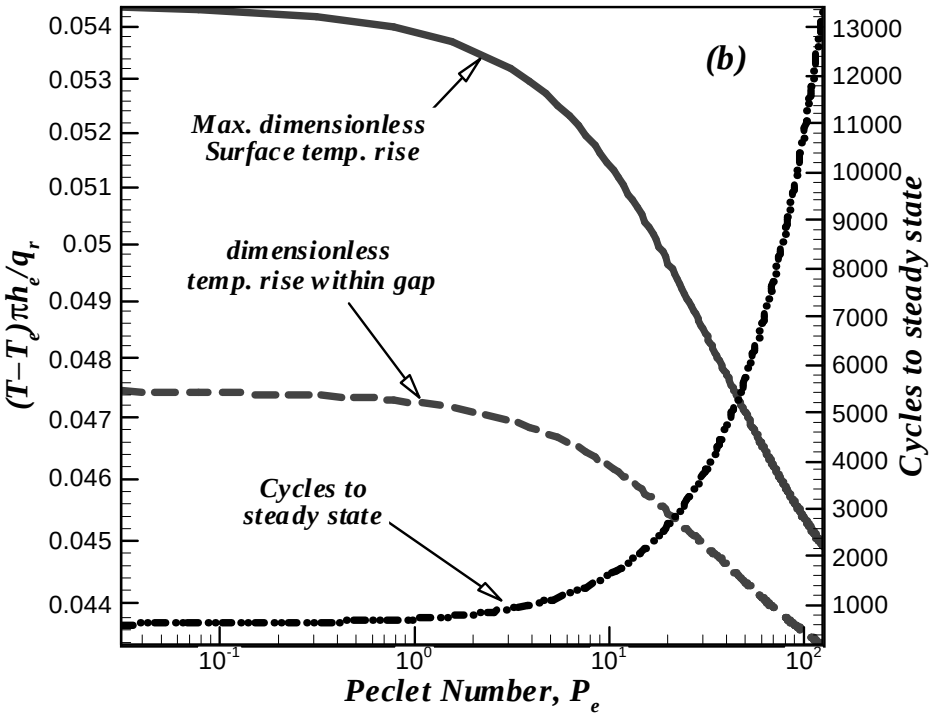

(b) Steady state versus Peclet number

Figure 63. Effect of the Peclet Number.

maximum surface temperature rise is about 1%, and the number-of-cycles to steady state decreased by about 2.5%. The interfacial Biot number plays a minor role in predicting the steady state maximum surface temperature rise. Curve fit relations for the dimensionless steady state maximum surface temperature rise and the number-of-cycles to steady state are as follows:

$$\Theta_{\max}(B_i) = c_0 + c_1 B_i\,,\; N_c = c_2 + c_3 B_i \tag{132a}$$

$$c_0 = 0.05,\; c_1 = -0.027,\; c_2 = 2677,\; c_3 = -932 \tag{132b}$$

Equations (132) are valid for the fixed parameters $P_e = 6\pi$, $\phi_m = \pi/6$, $\alpha = \pi/12$ ($\beta = 2$), and range of Biot numbers as given in Table 3.

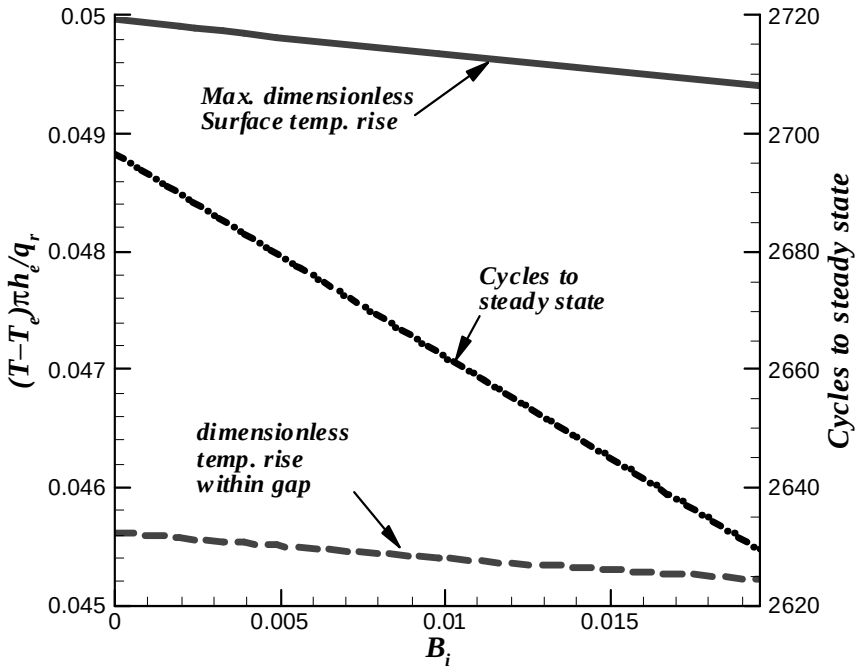

Figure 64. Effect of the Biot Number.

Effect of the Oscillation Amplitude

Figure 65 (a) illustrates the effect of the dimensionless oscillation amplitude ϕ_m on the cyclic maximum surface temperature rise ratio at fixed semi-contact width $\alpha = \pi/12$. Increasing

the amplitude yields a lower surface temperature rise and a monotonically decreasing number-of-cycles to steady state as shown in Figure 65 (b). For constant speed motion, the frequency of oscillation for constant speed, $f = \omega/(4\phi_m)$, decreases with the oscillation amplitude. The ratio $\beta = \phi_m/\alpha$ increases with the amplitude for a fixed semi-contact width, and spans the range of $\beta = 1/2$ to 4 as ϕ_m increases. Thus increasing the oscillation amplitude, ϕ_m, or decreasing the frequency *f*, has a reducing effect on the maximum steady state surface temperature. Physically, this can be attributed to a larger period of oscillation (lower frequency) giving more time for heat to be diffused away from the surface during each cycle, and to a larger surface area becoming exposed to the convective cooling effect within the gap. At low amplitudes (or when operating at high frequencies) the cyclic variation in the steady state maximum surface temperature rise becomes less pronounced. The maximum surface temperature rise appears to tend to a constant value. This is typical of a fretting behavior.

Curve fit relationships for the dimensionless steady state maximum surface temperature rise and number-of-cycles to steady state are as follows:

$$\Theta_{\max}(\phi_m) = c_0 + c_1\phi_m + c_2{\phi_m}^2,\ N_c = e^{c_3}{\phi_m}^{c_4} \tag{133a}$$

$c_0 = 0.051$, $c_1 = 0.00076$, $c_2 = 0.0048$, $c_3 = 7.33$, c4 = 0.854 (133b)

These relationships are valid for the fixed parameters $P_e = 6\pi$, $B_i = B_{ie}/5$, $\alpha = \pi/12$, and range of oscillation amplitudes as given in Table 3. For processes that involve fretting, oscillation amplitudes are generally very small, i.e., $\phi_{m.} << \alpha$. In a constant-speed oscillatory frictional process, this corresponds to small β-ratios and high oscillation frequencies. In an analytical treatment of fretting surface temperatures, Greenwood et al. [25] considered a distributed planar heat source at the contact whose position was assumed to be stationary. In [25], the authors

considered planar contact geometry (circular, square, and Hertzian stationary heat flux oscillating at constant frequency). The relevant parameter controlling the periodic solution was defined as $\gamma = a\sqrt{\omega/\kappa}$, where a is the radius of contact and ω is the frequency. It was observed in [25] that the periodic variation in the maximum surface temperature rise becomes unimportant for large contact or low frequency. In the constant-speed oscillatory problem, both of these conditions correspond to small amplitudes. A series of computations was carried out to simulate fretting with the present model. Results are plotted in Figure 65 (b). For small oscillation amplitudes, the dimensionless steady state maximum surface temperature rise asymptotically approaches a constant value of 0.051. This value corresponds to zero amplitude; see Equation (133). This asymptotic steady sate value is independent of the oscillation amplitude and time. Numerical results of the present work show the same trend as that derived analytically in [25], as depicted in Figure 65 (b).

Effect of the Dimensionless Contact Width

Figure 66 shows plots of the cyclic variation of the maximum surface temperature for selected values of the dimensionless semi-contact width α at a fixed amplitude ϕ_m = π/6 (constant oscillation frequency). Figure 66 clearly shows that the maximum surface temperature increases with increasing contact width, or equivalently with decreasing β-ratio. Note that the β-ratio spans the range of β = ½ to 4 for decreasing α. The number-of-cycles to steady state decreases with the semi-contact width. Physically, both such variations in the maximum surface temperature and time-to-steady-state are due to the combined effects and varying intensities of heating, cooling and diffusion of heat as α varies. For small values of the semi-contact width, according to Equation (115), the heating flux decreases. The larger surface area within the oscillation span receives heat only periodically as the heat flux oscillates and passes through the same point. This results in a

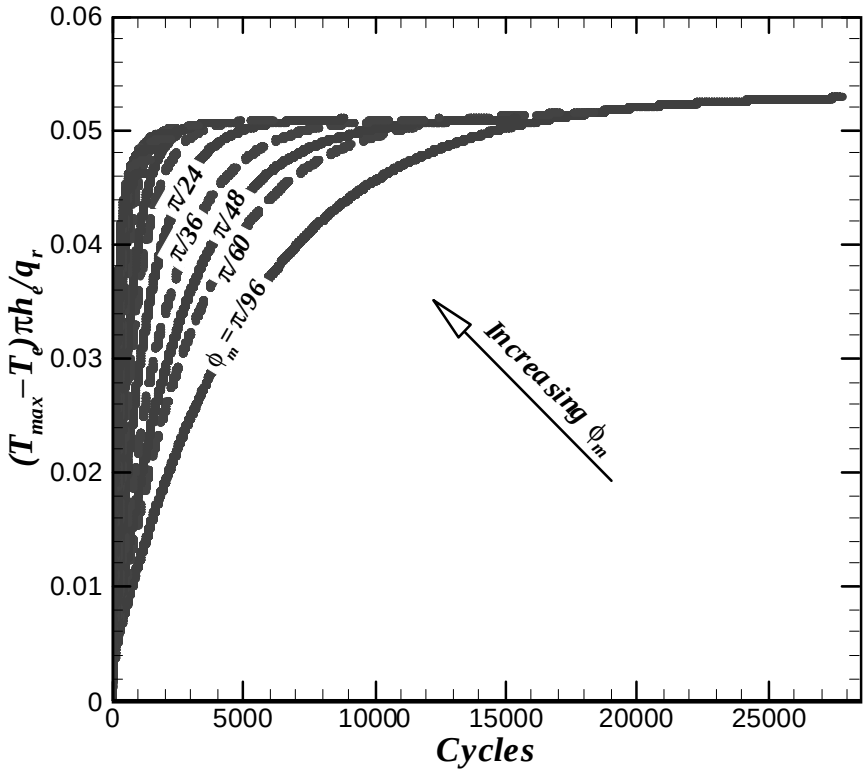

(a) Cyclic variations

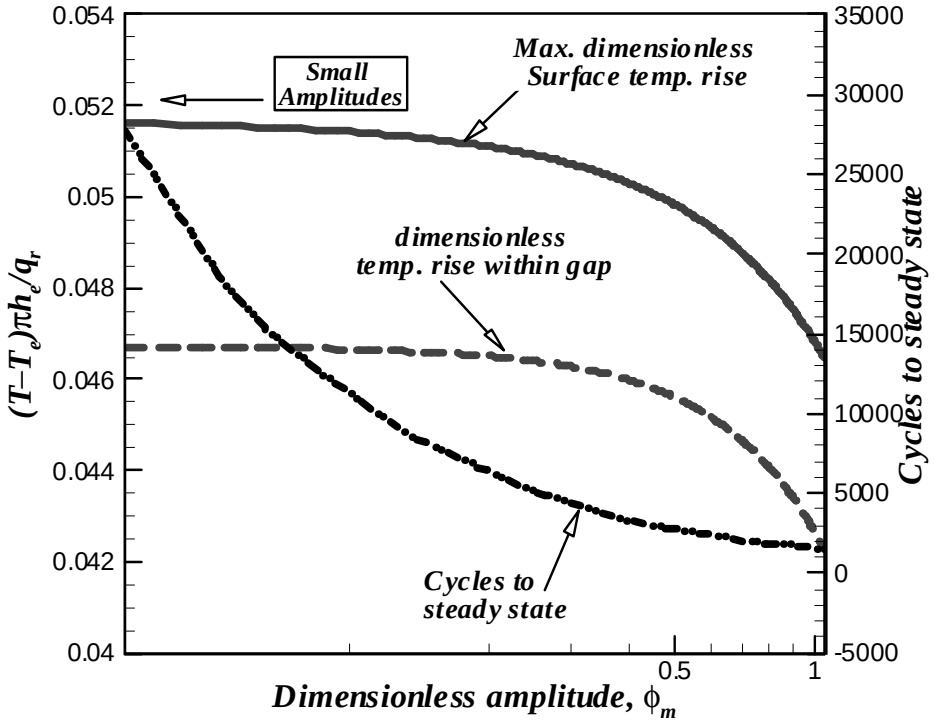

(b) Steady state versus amplitude

Figure 65. Effect of the dimensionless oscillation amplitude.

lower surface temperature rise. Since the gap temperature tends to be closer the surface temperature, the cooling effect at the interface is insignificant and a longer time-to-steady-state results. As the contact width increases, the dimensionless frictional heat flux becomes larger, and the surface temperature rise is therefore larger. However, the surface temperature difference at the interface tends to become larger as seen in the Figure 66 (a). This cooling effect at the interface tends to have a decreasing effect on the number of cycles to steady state.

Curve fit relationships for the dimensionless maximum steady state surface temperature rise and the number-of-cycles to steady state are as follows:

$$\Theta_{\max}(\alpha) = c_0 + c_1\alpha + c_2\alpha^2 \tag{134a}$$

$$N_c = \exp\left(c_3 \ln\alpha + c_4\right) \tag{134b}$$

c_0 = 0.00727, c_1 = 0.06, c_2 = 0.062, (134c)

c_3 = 0.1586, c_4 = 7.7767 (134d)

These relationships are valid for the fixed parameters $P_e = 6\pi$, $B_i = B_{ie}/5$, $\phi_m = \pi/6$, and range of semi-contact widths listed in Table 3.

Application Examples

In order to gain some insight into the model utility, it is appropriate to focus on the dimensional quantities. The maximum steady state surface temperature may be expressed as follows:

$$\Delta T_{\max} = \frac{\mu_c E_c \kappa P_e}{2\pi k B_{ie}}\left(\frac{C_r}{1+C_r}\right)\Theta_{\max}\left(\theta_{\max}, \phi, P_e, B_i, \phi_m, \alpha\right) \tag{135}$$

where the maximum dimensionless solution and its location are determined numerically. The definitions of the Peclet number $P_e = v_m r_s / \kappa$, and ambient Biot number, $B_{ie} = h_e r_s / k$, have been employed in the conversion. The *dimensionless* surface temperature rise is negligibly

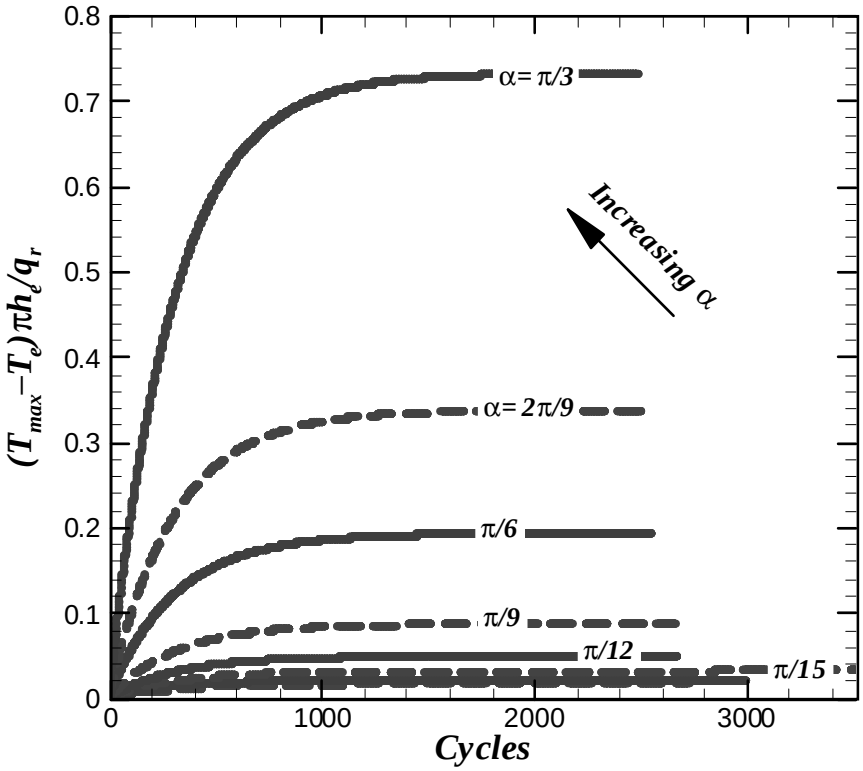

(a) Cyclic variations

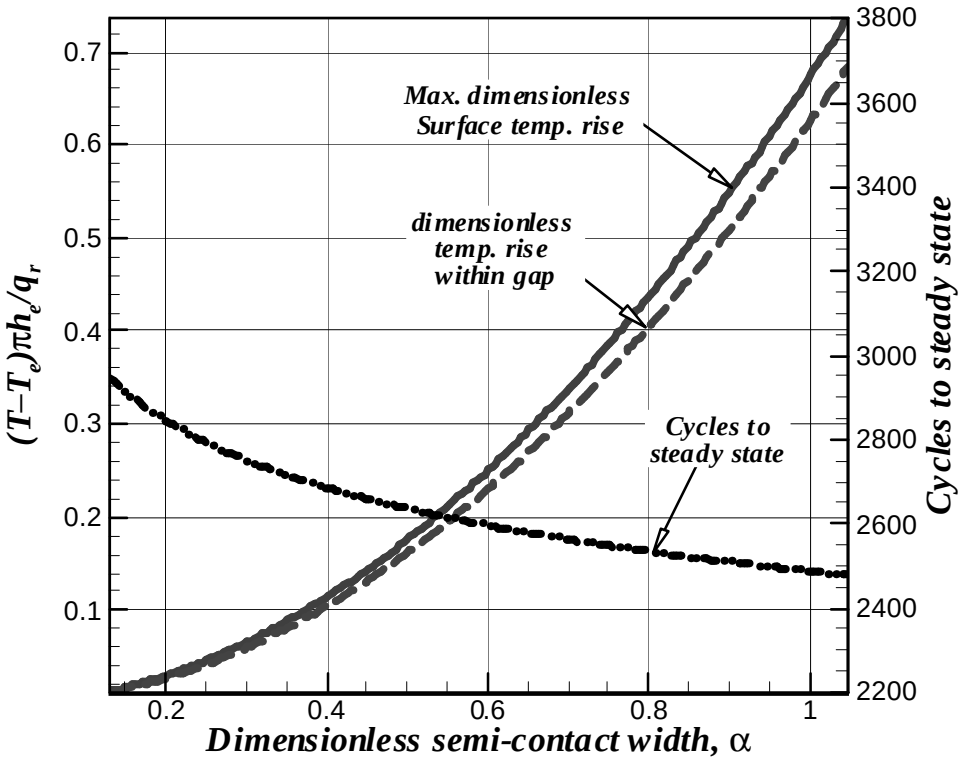

(b) Steady state versus semi-contact width

Figure 66. Effect of the dimensionless semi-contact width.

affected by small clearance ratios, C_r. However, as seen from Equation (135), this parameter plays an important role in determining the severity of the *actual* surface temperature rise. The surface temperature rise is proportional to the clearance ratio for small C_r values.

Based on observations made earlier, the actual maximum surface temperature rise is proportional to $P_e^{0.95}$. Thus, larger clearance ratios and higher Peclet numbers (sliding speeds) yield larger surface temperatures.

For design purposes, Equation (109) must be used in conjunction with Equation (135). Equation (109) is rewritten here as

$$p_l = \left(\frac{w_a}{2 r_s L_c} \right) = \frac{\pi}{4} \frac{E_c}{2} \left(\frac{C_r}{1 + C_r} \right) \alpha^2 \tag{136}$$

For instance, the clearance ratio, C_r, and/or the projected load, p_l, can be chosen to satisfy desired operating and geometric parameters such as the dimensionless variables P_e, B_i, ϕ_m, α, μ_c, B_{ie}, and desired limits on the maximum surface temperature rise, ΔT_{max}. Alternatively, if a desired projected load is specified, one may determine the limiting sliding speed knowing the clearance ratio and the parameters B_i, ϕ_m, α, μ_c, B_{ie}. Examples are provided in the following sections to show the model utility. The material properties assumed in the examples are listed in Table 4.

Table 4. Materials properties at 20 oC.

Thermal conductivity	k_s, k_b (W/m-K)	52
Specific heat	c_s, c_b (W/kg-K)	460
Thermal Diffusivity	κ_s, κ_b (m^2/s)	10^{-5}
Young's modulus	E_s, E_b (GPa)	201
Poisson's ratio	ν_s, ν_b	0.3
Friction coefficient	μ_c	0.1

Example 1. Clearance Ratio and Projected Load

Given the Peclet number P_e = 6π and the oscillation amplitude ϕ_m = π/6, it is desired to determine the clearance ratios and applied loads that yield a steady state maximum surface temperature rise of ΔT_{max} = 500 °C for a semi-contact width of α = π/12. Using Figure 63, the dimensionless steady state surface temperature rise is $\Theta_{\max}$ = 0.421, and the number of cycles to steady state is N_c = 2485. The curve-fit formula, Equation (134), gives $\Theta_{\max}(\pi / 4) \approx 0.422$, $N_c = e^{7.77}\left(\pi / 4\right)^{-0.22} \approx$ 2500. Using Equation (135), the required clearance ratio is given by

$$\frac{1}{C_r} = \frac{\mu_c E_c \kappa}{2\pi k \Delta T_{\max}} \frac{P_e \Theta_{\max}}{B_{ie}} - 1 = \frac{(0.1)(114.6\text{x}10^9)(10^{-5})}{2\pi(52)(500)} \frac{6\pi(0.421)}{(0.01954)} - 1 \approx 284$$

Thus, $C_r \leq 3.5 \text{ x } 10^{-3}$. Using Equation (136), the maximum allowable projected load is

$$p_l = \left(\frac{w_a}{2 r_s L_c}\right) = \frac{\pi}{4}\frac{E_c}{2}\left(\frac{C_r}{1+C_r}\right)\alpha^2 = \frac{\pi}{4}\frac{(114.6\text{x}10^9)}{2}\left(\frac{\pi}{4}\right)^2\left(\frac{3.5\text{x}10^{-3}}{1+3.5\text{x}10^{-3}}\right) \approx 97 \text{ MPa.}$$

This result is applicable to any applied load and any pin size such that the clearance ratio and projected loads are taken below the calculated limits.

Example 2. Sliding Speed

Given the oscillation amplitude ϕ_m = π/6, the semi-contact width α = π/12, and the clearance ratio $C_r = 3.5 \text{ x } 10^{-3}$, it is desired to determine the maximum sliding speed and pin size that yield a steady state maximum surface temperature rise of ΔT_{max} = 500 °C with an applied load of w_a = 30 kN. Using Equation (135), one may compute the product

$$P_e \Theta_{\max} = \left(\frac{1}{C_r} + 1\right)\frac{2\pi k B_{ie}}{\mu_c E_c \kappa} \Delta T_{\max} = 7.936$$

The Peclet number is determined using the simple curve fit form of $\Theta_{\max}(P_e)$, Equation (131). Thus, $P_e\Theta_{\max} = c_0 P_e + c_1 P_e \left(1 + 2c_1{}^2 c_2 P_e\right)^{-1/2}$ = 7.936 yields P_e = 173.65. Using Equation (116), the projected load is, $p_l = \left(\frac{w_a}{2r_s L_c}\right) = \frac{\pi}{4}\frac{E_c}{2}\alpha^2\left(\frac{C_r}{1+C_r}\right) \approx 10.83$ MPa. Since the load is given, this gives the pin size as follows $2r_sL_c$ = 2771 mm^2. Assuming a contact length of L_c = 25.4 mm, one obtains the pin radius $r_s \approx$ 54.5 mm. The maximum sliding speed is $v_m = \kappa P_e / r_s$=32 mm/s. This gives the value of the oscillating speed amplitude, which would yield the critical temperature rise. The number of cycle to this critical value may be estimated using the simple curve fit formula $N_c \approx$ 16686 cycles to steady state.

Concluding Remarks

A two-dimensional mathematical model has been developed for the transient dimensionless surface temperature behavior in sliding bodies with oscillatory sliding velocity and Hertzian line contact frictional interface. The set of partial differential equations with switching coefficients has been discretized and solved numerically using the Runge-Kutta method with adaptive time stepping.

Results show that, for moderate to large Peclet numbers, the dimensionless maximum steady state surface temperature varies as P_e^n, $0 < n < 1$, while the number of cycles to steady state varies with the Peclet number as P_e^m, $0 < m < 1$. The coefficients and exponents, m and n, of the curve-fit relationships are generally functions of other dimensionless parameters. For very low Peclet numbers, the dimensionless maximum steady state surface temperature approaches a constant value that is independent of the Peclet number. This behavior has also been reported in [16].

The maximum steady state surface temperature and the number of cycles-to-steady-state are reduced linearly as the Biot number is increased.

Increasing the oscillation amplitudes at fixed semi-contact width (i.e., larger ratios $\beta = \phi_m / \alpha$) yields lower steady state maximum surface temperatures and lower number-of cycles-to-steady-state. Small oscillation amplitude frictional processes tend to approach a common steady state surface temperature. This behavior is consistent with the analytical solution derived in [25]. A larger semi-contact width with fixed oscillation amplitude (i.e., lower ratios $\beta = \phi_m / \alpha$) yields a greater maximum steady state surface temperature. This trend is parabolic in form.

Chapter 11. Pin-Bushing Thermal Model Verification

In the test rig, the pin is oscillating, while the bushing is stationary. As a result, the contact zone is stationary (unlike the case treated earlier where the bushing was the moving part) and is located symmetrically at the point of application of the applied load. A two-dimensional schematic representing the experiment is as presented in Figure 67. A simplified representation used in simulation is shown in Figure 68. The dimension shown in these figures are in inches. The model includes the floating block that encloses the housing. In the test rig, a stationary precision bearing is used to support and align the housing within the floating block. The outer boundary is assumed to be exposed to ambient convective cooling at room temperature and h_e ~ 80 W/m^2-C. This heat transfer coefficient is estimated as outlined in the appendix. At the sliding interface between the pin and the bushing, frictional heating is applied at the contact and continuity is imposed. Outside the contact region (within the gap region), an equivalent convective cooling boundary condition is applied, where the heat transfer coefficient is a combination of convection due the enclosed air within the clearance and radiation exchange. Details of estimating this heat transfer coefficient within the gap interface are given in the appendix.

The finite element method is used to solve the thermal problem. A description of the finite element discretization is given next, followed by a presentation of the numerical results and comparison with experimental data. The thermal dimensionless material properties and speed will be denoted K, D, C for thermal conductivity, density, and heat capacity, and $V(\tau)$, respectively. These dimensionless quantities were defined in the dimensionless model formulation in Chapter 6.

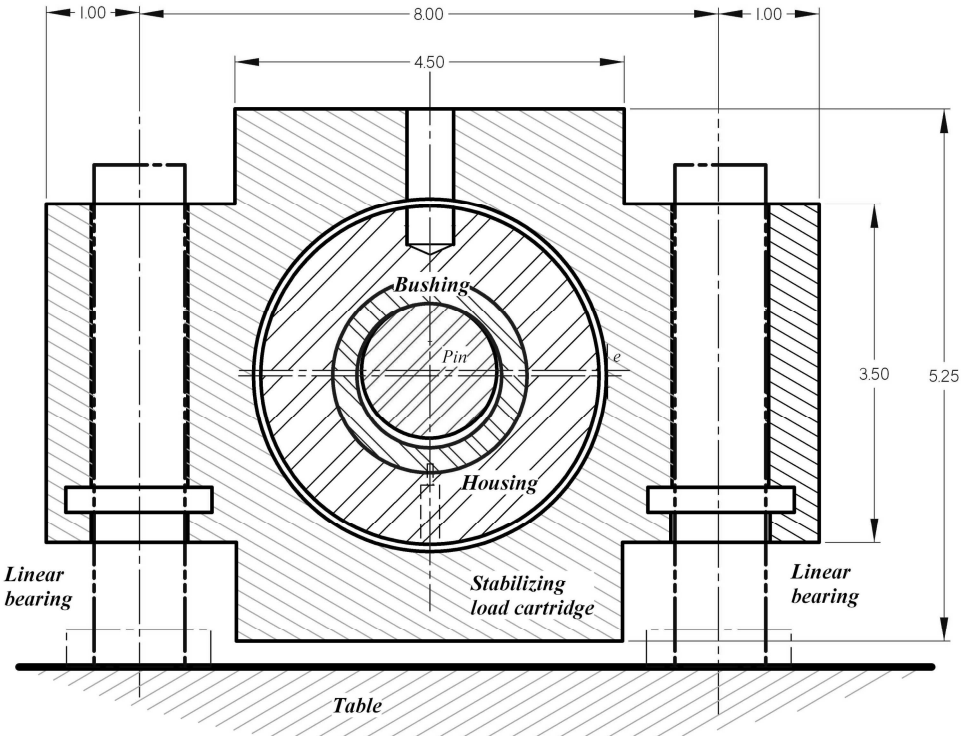

Figure 67. Schematic of the experimental model.

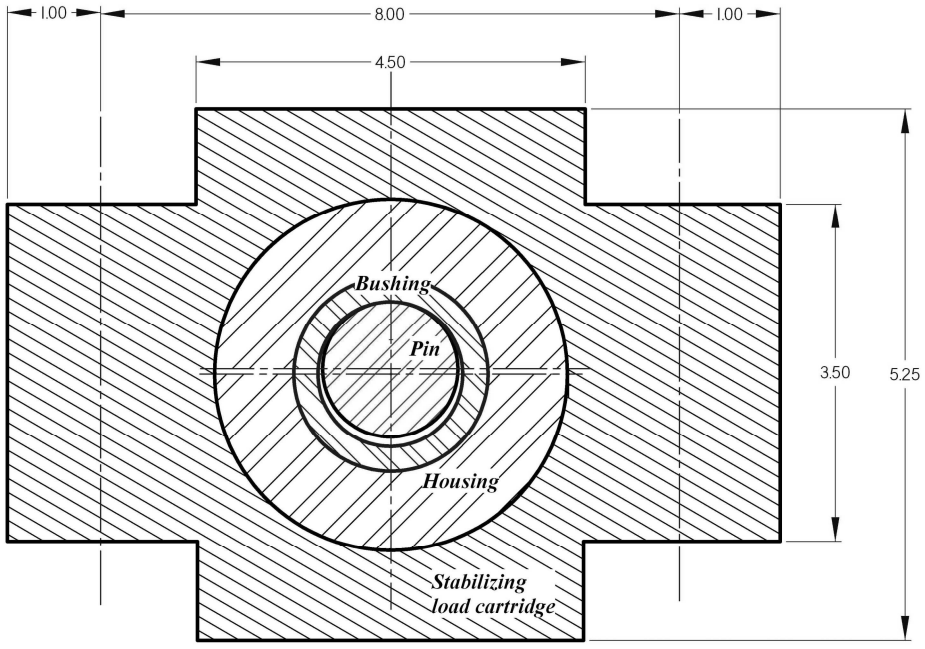

Figure 68. Simplified experimental model.

The Finite Element Method

A finite element computational model was used to solve the dimensionless thermal model equations. Recalling the transient heat equation:

$$DC\frac{\partial\Theta}{\partial\tau}+mDCV\left(\tau\right)\frac{\partial\Theta}{\partial\theta}=\nabla\bullet\left(K\nabla\Theta\right)+Q_b\left(\Theta\right) \tag{137}$$

Equation (137) is first discretized in time using an implicit finite difference scheme as follows:

$$\begin{aligned} &DC\Theta_{(\tau)}+d\tau\lambda mDCV\frac{\partial\Theta_{(\tau)}}{\partial\theta}-d\tau\lambda\nabla\bullet\left(K\nabla\Theta_{(\tau)}\right)\\ &=DC\Theta_{(\tau_0)}-d\tau\left(1-\lambda\right)mDCV\frac{\partial\Theta_{(\tau_0)}}{\partial\theta}\\ &\qquad+d\tau\left(1-\lambda\right)\nabla\bullet\left(K\nabla\Theta_{(\tau_0)}\right)+d\tau Q_b\left(\Theta_{(\tau)}\right)\end{aligned} \tag{138}$$

where $\Theta_{(\tau)}\left(\rho,\theta\right)$ is the temperature distribution at time step τ, and the parameter $0\le\lambda\le1$ is a weight parameter; in particular $\lambda=1/2$ produces the Crank-Nicholson scheme. The vector $\Theta_{(\tau)}$ holds the updated temperature distribution at current time step *t*, while $\Theta_{(\tau_0)}$ holds the old one. Notice that the time-discretized heat equation can now be written in the form

$$\mathcal{L}\left(\Theta_{(\tau)}\right)=\mathcal{f}\left(\Theta_{(\tau)},\Theta_{(\tau_0)}\right) \tag{139a}$$

where

$$\mathcal{L}\left(\Theta_{(\tau)}\right)=DC\Theta_{(\tau)}+d\tau\lambda mDCV\frac{\partial\Theta_{(\tau)}}{\partial\theta}-d\tau\lambda\nabla\bullet\left(K\nabla\Theta_{(\tau)}\right) \tag{139b}$$

$$\begin{aligned}\mathcal{f}=\;&DC\Theta_{(\tau_0)}-d\tau\left(1-\lambda\right)mDCV\frac{\partial\Theta_{(\tau_0)}}{\partial\theta}\\ &+d\tau\left(1-\lambda\right)\nabla\bullet\left(K\nabla\Theta_{(\tau_0)}\right)+d\tau Q_b\left(\Theta_{(\tau)}\right)\end{aligned} \tag{139c}$$

That is, $\mathcal{L}$ is a linear operator and $\mathcal{f}\left(\bullet\right)$ is a forcing function that depends on the solution and its derivatives. To apply the Galerkin criterion to the heat equation, we assume the

approximate solution

$$\Theta_{(\tau)}(r,\theta) \approx S_k(r,\theta)\hat{\Theta}_k(\tau): \quad \text{(Summation convention holds)} \tag{140}$$

The initial boundary-value problem is satisfied in the Galerkin sense provided that

$$\int_{\Re} S_j(r,\theta)\left(\mathcal{L}(\Theta_{(\tau)}) - \mathcal{f}\right) d\Re = 0: \quad \textit{For all } S_j(r,\theta)\textit{, j=1, 2, 3 ... } N_e \text{ nodes} \tag{141}$$

where $S_j(r,\theta)$ are test functions equal to the shape functions in this case. The shape functions $S_j(r,\theta)$ are assumed to be continuous and identically zero outside elements containing the *j*-th node. $\Re$ is the element domain. When the Galerkin criterion is applied within the local element domain, it yields an element matrix equation. The essential and natural boundary conditions are applied only to those elements that fall on the boundary points of the mesh. The element matrix equations are then assembled in order to obtain an augmented linear system of equations that can be solved for the unknown nodal values of the dependent variable, here the temperature. Notice that the linear operator $\mathcal{L}$ can be written in the form:

$$\mathcal{L} = \mathcal{L}_1 + \nabla\mathcal{L}_2 \tag{142}$$

Here, $\mathcal{L}_1$ and $\mathcal{L}_2$ are first order operators and $\mathcal{L}_2$ may be a vector or tensor valued to allow for the reduction operation when the gradient operator is applied. From inspection of equation (119) it follows that:

$$\mathcal{L}_1(\hat{\Theta}) = DC\hat{\Theta} + d\tau\lambda mDCV\frac{\partial\hat{\Theta}}{\partial\theta} \text{ :: a scalar quantity.} \tag{143a}$$

$$\mathcal{L}_2(\hat{\Theta}) = -d\tau\lambda\left(K\nabla\hat{\Theta}\right) \text{ :: a vector quantity.} \tag{143b}$$

The Galerkin's criterion, equation (141), is developed using integration by parts and the divergence theorem. Therefore,

$$\int_{\Re} S_j(r,\theta)\mathcal{L}_1(\hat{\Theta})d\Re + \int_{\Gamma} S_j(r,\theta)\,\mathbf{n}\bullet\mathcal{L}_2(\hat{\Theta})d\Gamma - \int_{\Re} \mathcal{L}_2(\hat{\Theta})\bullet\nabla S_j d\Re = \int_{\Re} \mathcal{f} S_j(r,\theta)d\Re \tag{144}$$

where Γ represents the boundary of the element domain $\Re$, and $\mathbf{n}$ is the outward normal vector to Γ. More specifically, equation (144) becomes

$$\int_{\Re^e} S_j\left[DC\hat{\Theta} + d\tau\lambda\left(mDCA\dot{\Phi}\frac{\partial\hat{\Theta}}{\partial\theta}\right)\right]d\Re + d\tau\lambda\int_{\Re^e}\left(K\nabla\hat{\Theta}\right)\bullet\nabla S_j d\Re$$

$$-d\tau\lambda\int_{\Gamma^e} S_j\,\mathbf{n}\bullet\left(K\nabla\hat{\Theta}\right)d\Gamma = \int_{\Re^e}\mathcal{f} S_j d\Re \tag{145}$$

For all $S_j(r,\theta)$, j=1, 2, 3 ... N_e nodes, all elements *e*.

The boundary integral in (145) involves the frictional heat flux at the sliding interface, and convective heat transfer by cooling at the boundaries. This mixed boundary condition is written as:

$$\mathbf{n}\bullet\left(K\nabla\hat{\Theta}\right) + \mathcal{B}i\Delta\hat{\Theta} = \mathcal{Z} \tag{146}$$

Using (146), the boundary integral becomes:

$$\int_{\Gamma} S_j\,\mathbf{n}\bullet\mathcal{L}_2(\hat{\Theta})d\Gamma = -d\tau\lambda\int_{\Gamma^e} S_j\,\mathbf{n}\bullet\left(K\nabla\hat{\Theta}\right)d\Gamma = -d\tau\lambda\int_{\Gamma^e} S_j\left[-\mathcal{B}i\Delta\hat{\Theta} + \mathcal{Z}\right]d\Gamma \tag{147}$$

Upon applying the finite element approximation to equation (125), one obtains the element matrix equation:

$$\left[\mathrm{A}^e_{jk}\right]\left\{\hat{\Theta}^e_k\right\} = \left\{F^e_j\right\} :: j,k = 1...N_e,\ N_e = \text{number of nodes in element } e. \tag{148a}$$

where $\left\{\hat{\Theta}^e_k; k = 1...N_e\right\}$ is the vector of unknown nodal variables, and

$$\left[\mathrm{A}^{e}_{jk} \right] = \int_{\Re^e} S_j \left[DCS_k + d\tau\lambda \left(mDCV \frac{\partial S_k}{\partial \theta} \right) \right] d\Re$$

$$+ d\tau\lambda \int_{\Re^e} \nabla S_j \bullet \left(K \nabla S_k \right) d\Re + d\tau\lambda \int_{\Gamma^e} S_j Bi \Delta S_k d\Gamma \tag{148b}$$

$$\left\{ F^{e}_{j} \right\} = \int_{\Re^e} \mathcal{f} S_j(r,z) d\Re + d\tau\lambda \int_{\Gamma^e} S_j \mathcal{Z} d\Gamma \tag{148c}$$

The finite element procedure involves the assembly of such element equations and the boundary conditions into one system matrix equation. The boundary integrals that involve a known integrand are implemented by substituting directly the known values for the integrands. This becomes part of the right hand side of the system matrix equation, as shown by the last term in equation (145). If the boundary integral involves an unknown variable, then it is implemented by explicitly imposing the boundary condition as an alternate equation at the boundary. The system equation was solved iteratively.

Numerical Results

The measured coefficient of friction (COF) and temperatures were curve-fit for use in simulations and easy comparison. The behavior and curve fit profile of the COF was presented and discussed in detail in Chapter 3 based on two typical experiments for coated and uncoated stainless steel bushings. In the next paragraphs, the discussion is focused on the surface temperature rise at four selected locations on the bushing mid-plane on its outer wall. Figure 69 shows the finite element grid pattern of the pin and bushing used in simulations. Triangular quadratic finite elements are used in all computations. The small circles indicate the four selected locations corresponding to the thermocouple placement.

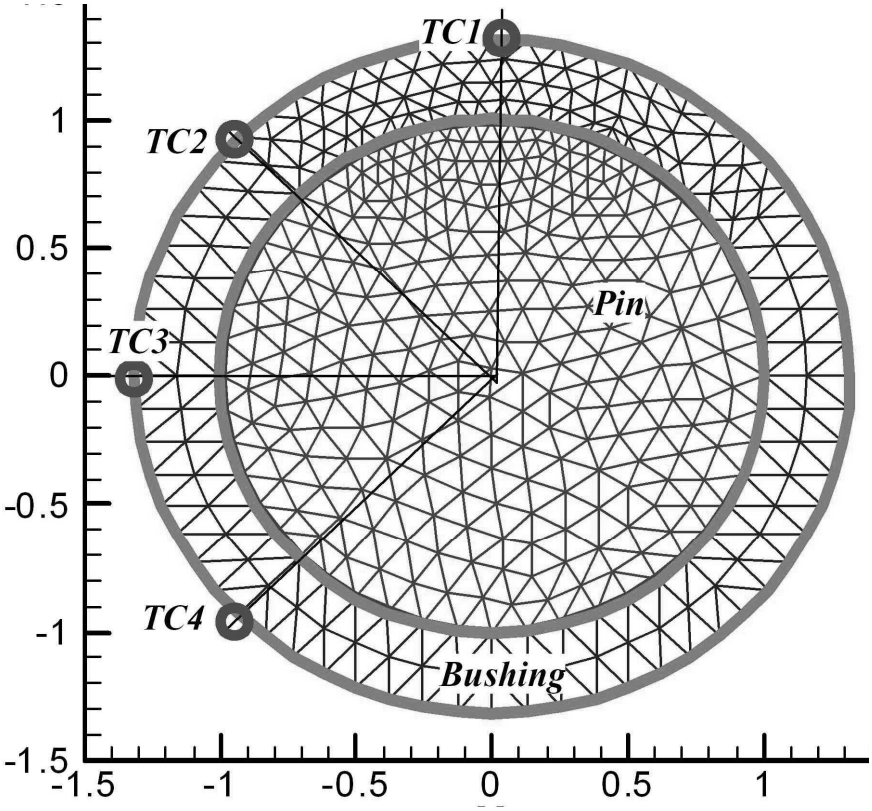

Figure 69. Dimensionless pin-bushing grid pattern used in simulations

Figures 70–71 show the computed temperatures at the four selected thermocouple locations for the production-bushing and plain-bushing test cases, respectively, under the same operating conditions of load, speed, and amplitude of oscillation. The computations appear to depict the behavior that was observed in the experimental data. However, the error at steady state is large. Figures 72-75 (plain bushing) and 76-79 (production bushing) show the computed temperature rise histories, plotted along with the measured temperatures at the selected thermocouple locations. The computational model exhibits a lower time constant and steady state is reached rather rapidly compared to the experiment. The plots show only a portion of the data up to 6000 cycles. Beyond this point, there is no change in the computed temperatures. The measured temperatures will continue to rise as depicted in the figures.

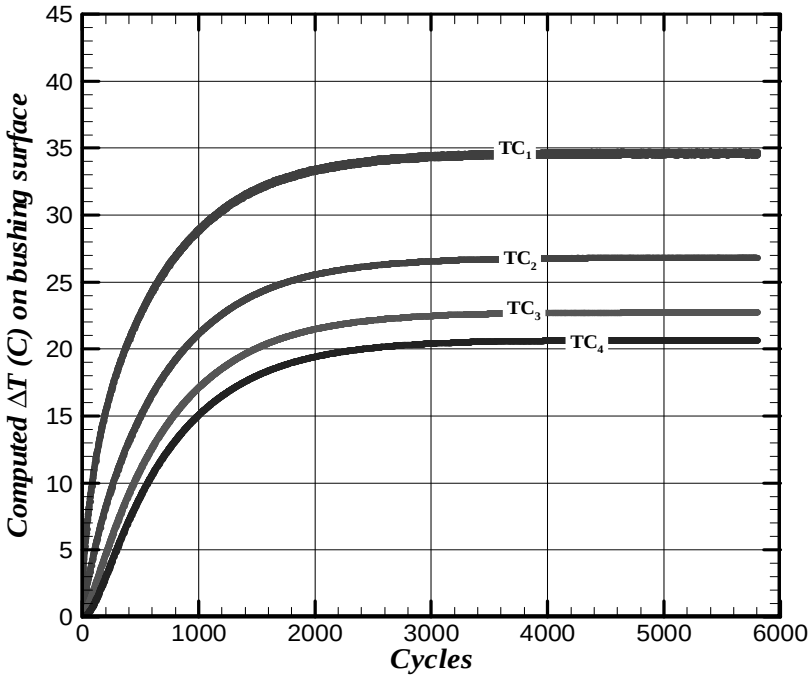

Figure 70.Computed temperature rise history: production bushing - compare to Figure 14

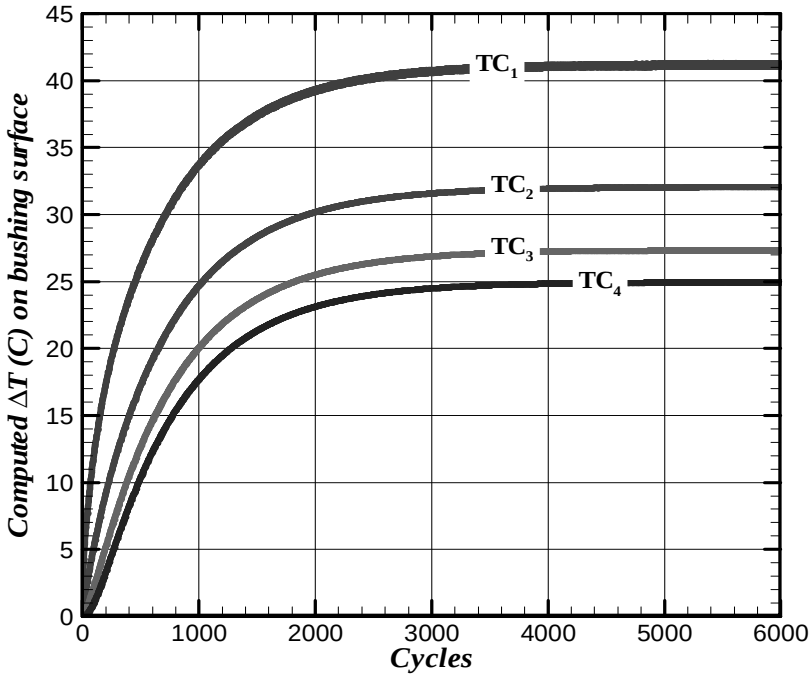

Figure 71. Computed temperature rise history: plain bushing - compare to Figure 15.

Inspection of the measured versus the computed temperature rise curves immediately shows discrepancy in the rise-time and steady state values. The time constant of the test rig response is larger than the computed model response. That is, a steady-state condition is reached rather rapidly in the computational model, with a lower steady-state value. Plots of the error histories, $E_T = \left(T_m - T_c\right)$, is shown in Figure 80 and 81, for the production and plain pin-bushing pairs. The subscripts (*m*) and (*c*) indicate the measured and computed temperatures, respectively. There is no clear pattern for the errors with respect to the thermocouple location. A method of reducing this error is recommended in Chapter 13 and detailed in the appendix. Preliminary calculations show that the method is promising, but more work is needed to generalize it.

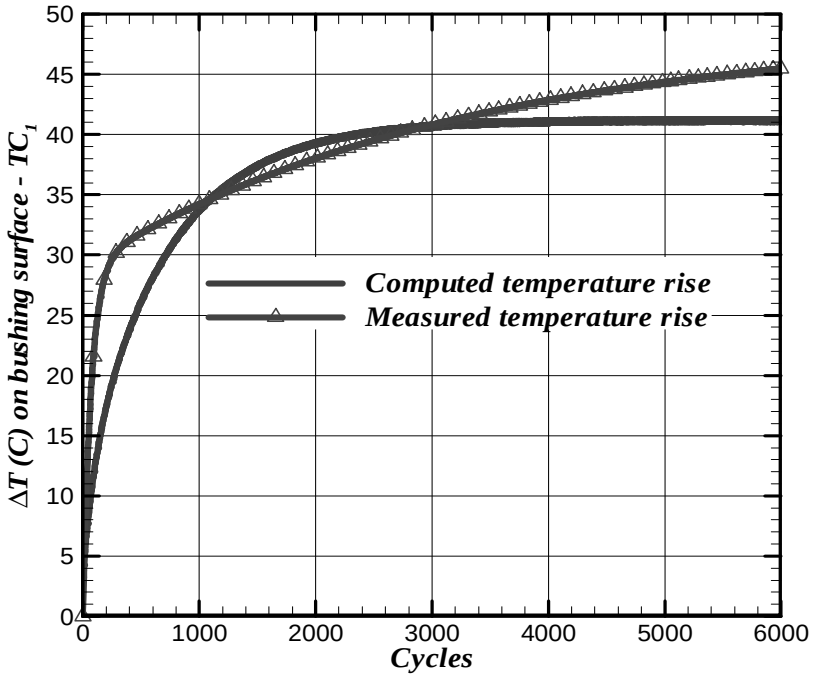

Figure 72. Comparison: plain bushing, thermocouple 1 — across contact

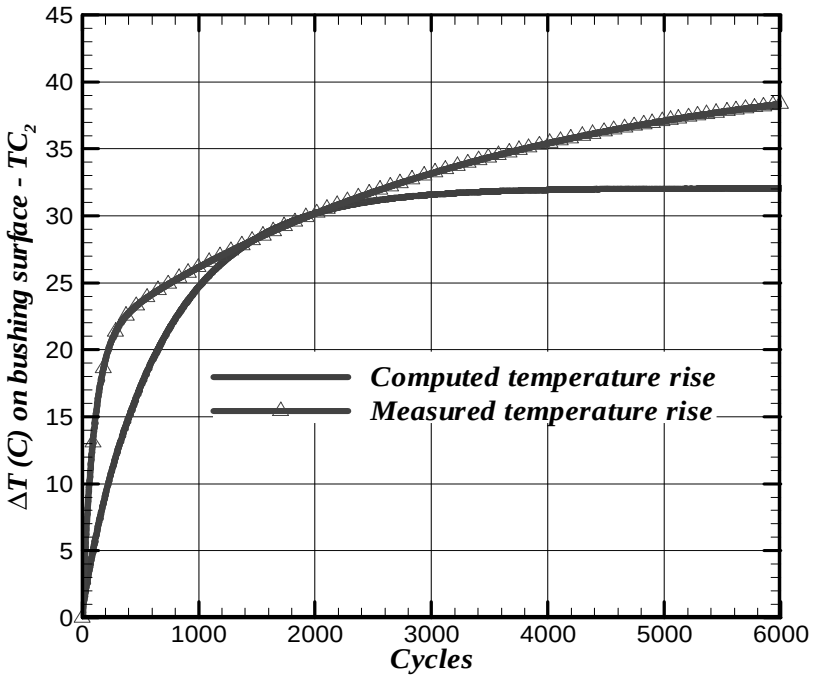

Figure 73. Comparison: plain bushing, thermocouple 2 — 45° from contact

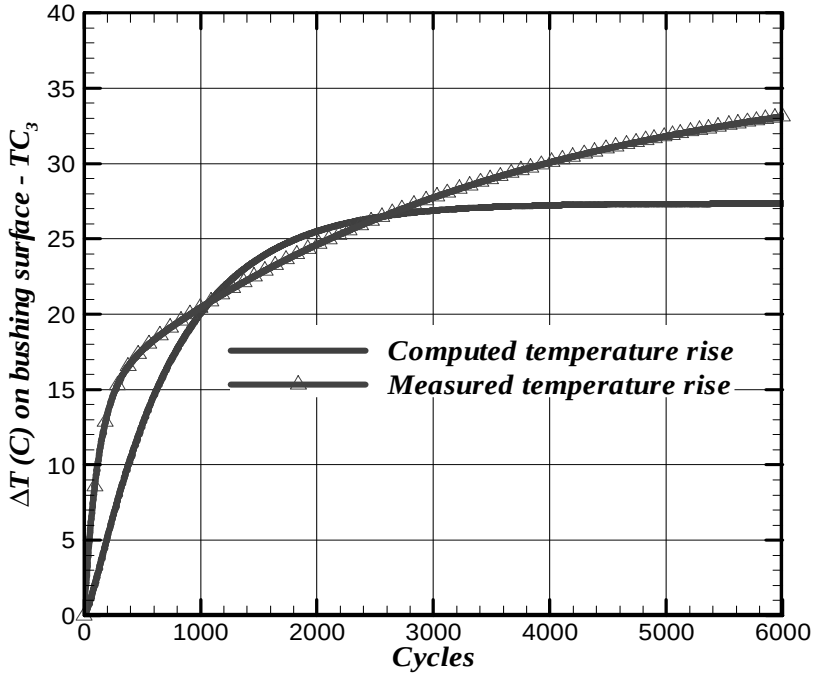

Figure 74. Comparison: plain bushing, thermocouple 3 — 90° from contact

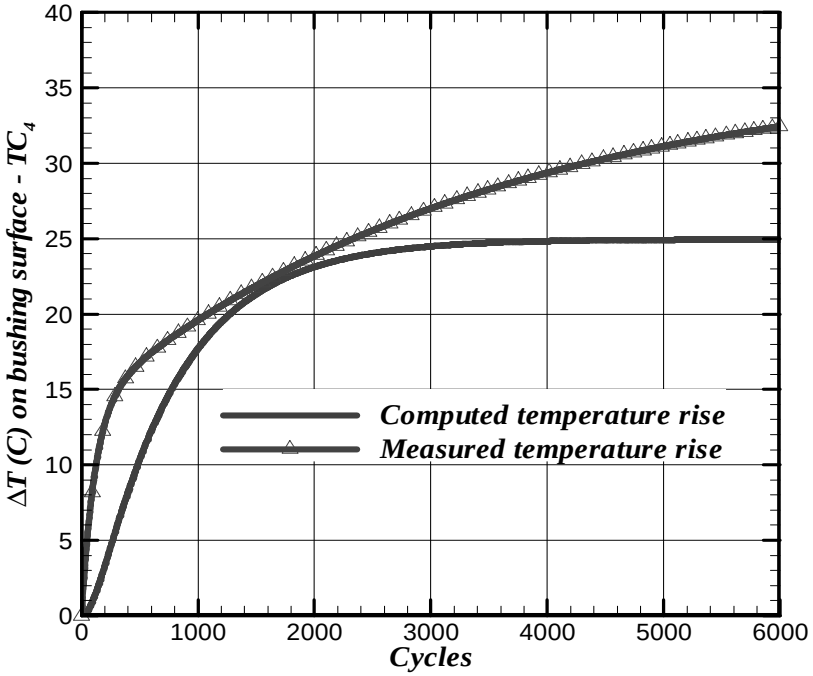

Figure 75. Comparison: plain bushing, thermocouple 4 — 135° from contact

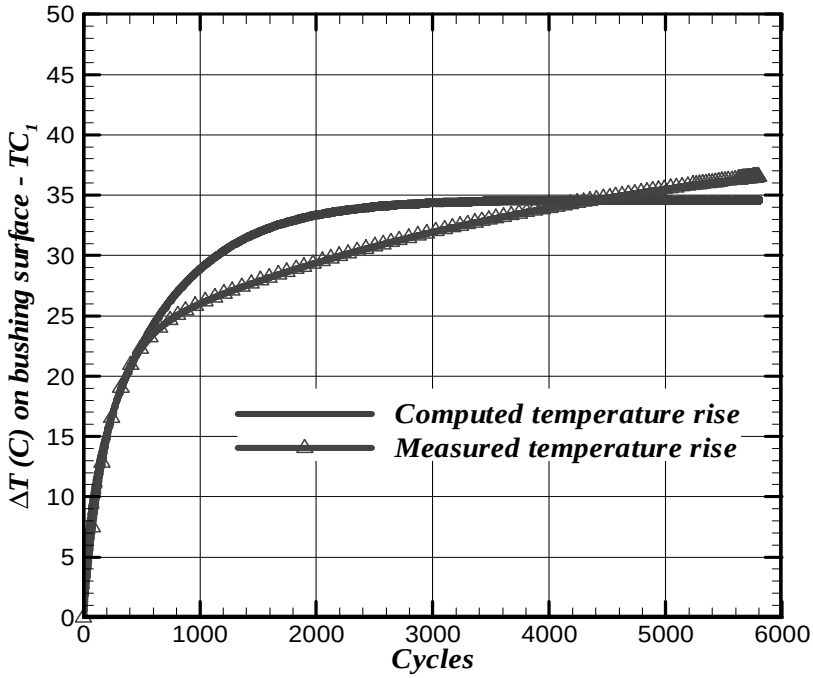

Figure 76. Comparison: production bushing, thermocouple 1 — across contact

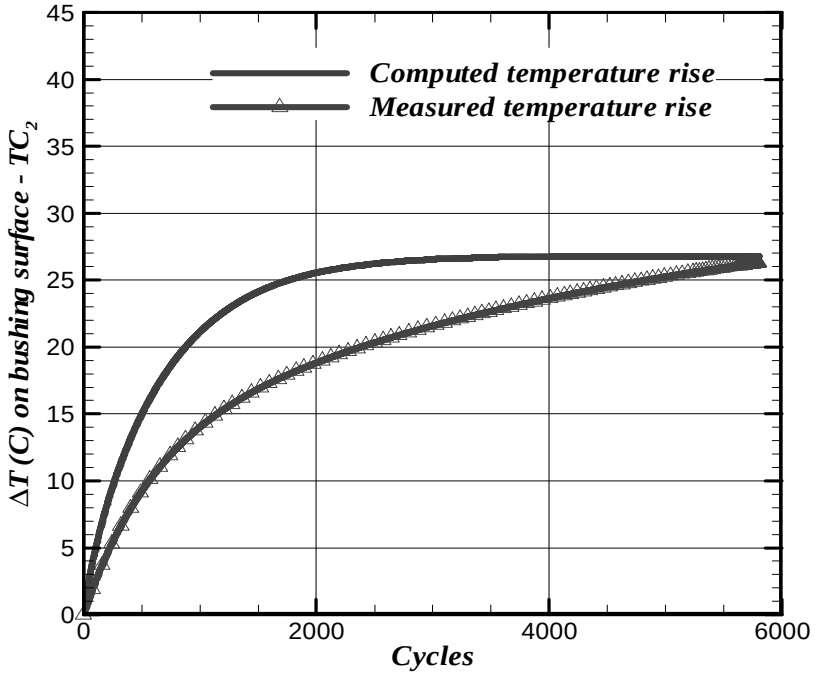

Figure 77. Comparison: production bushing, thermocouple 2 — 45° from contact

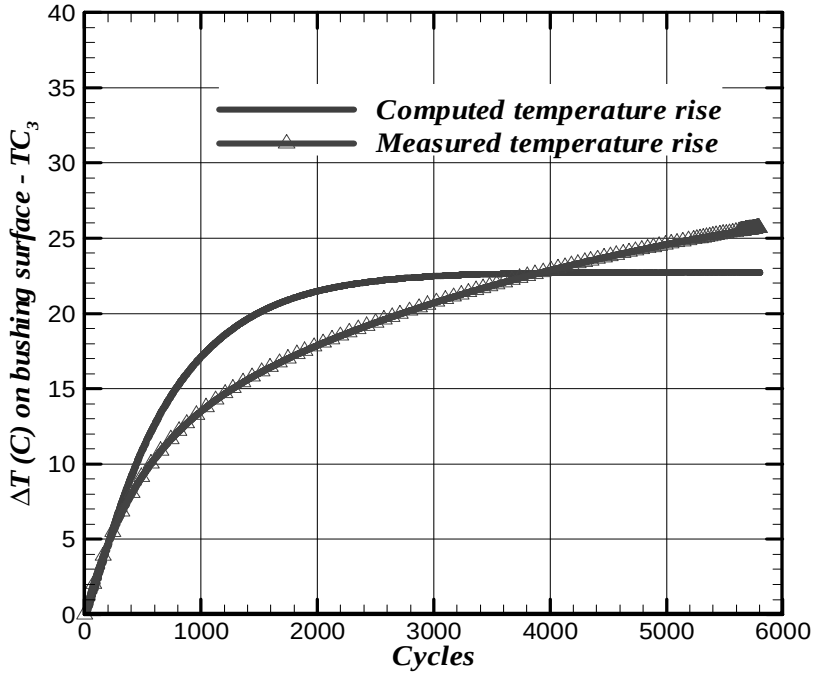

Figure 78. Comparison: production bushing, thermocouple 3 — 90o from contact

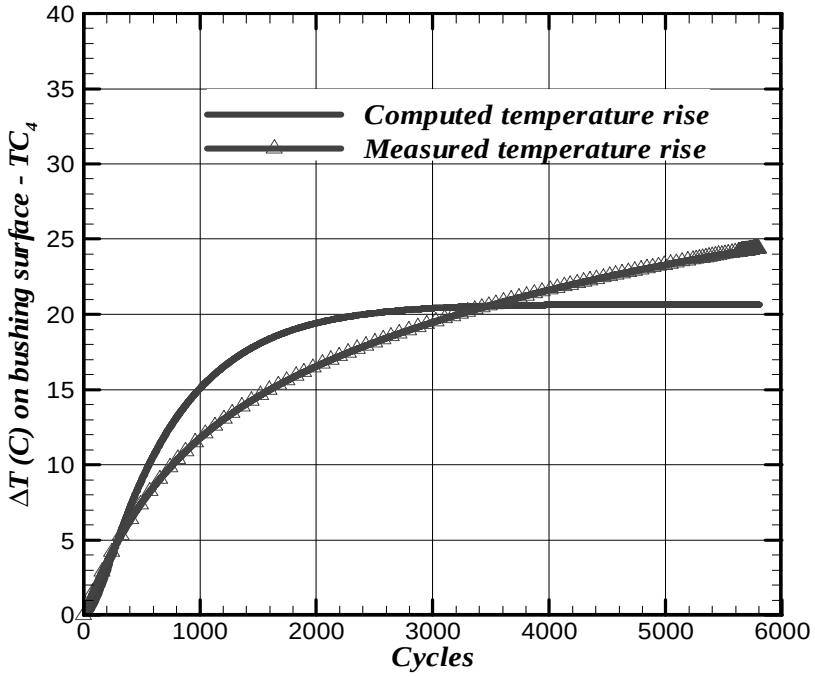

Figure 79. Comparison: production bushing, thermocouple 4 — 135o from contact

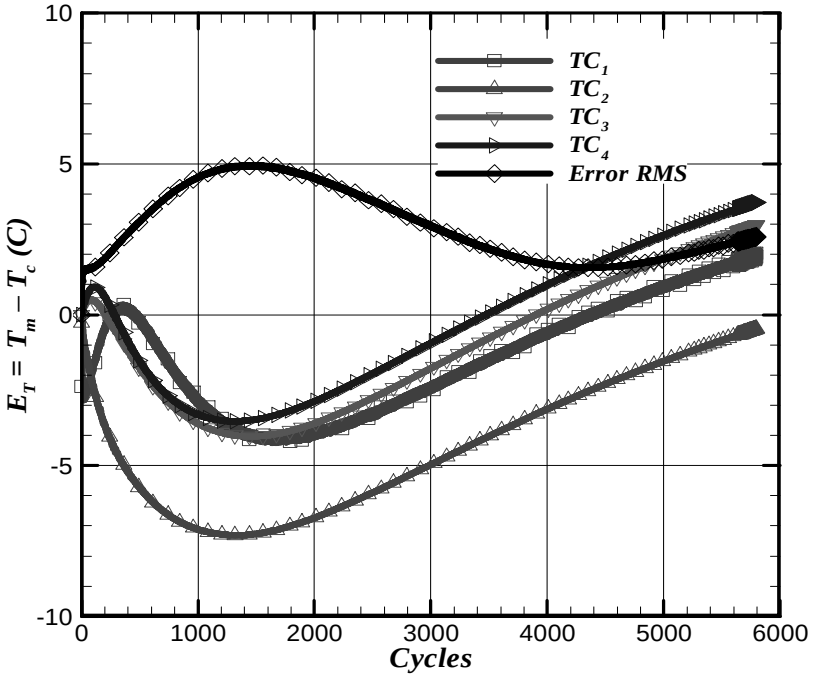

Figure 80. Error between computed and measured temperatures - production bushing.

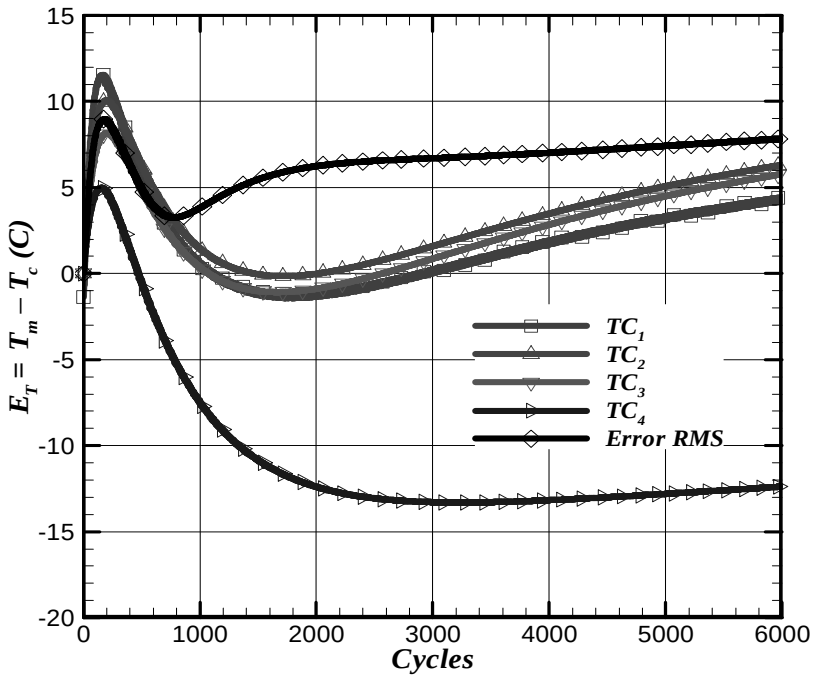

Figure 81. Error between computed and measured temperatures - plain bushing.

It is not trivial to point out the real causes of such discrepancies and an attempt is made to explain these based on a critique of the assumptions that were made. This will then be a basis for recommendations.

The boundary conditions of heating and cooling fluxes at the interface are the main determining parameters of the surface temperature and temperature distribution within the conducting media. The measured COF is assumed to represent the total frictional process at the contact. Combined with Hertzian theory, the heat flux was then computed. Although this may constitute a source of error, it is believed to be minor.

The assumption that a 2D section, presumably taken at the mid-plane of the pin-bushing pair, represents the actual 3D configuration in the test rig is believed to be a source of error. The averaging of the 3D problem along the axial direction provides an enhancement to a 2D representation, but does not take into account the real end-point heat transfer conditions, and possible misalignment and axial variation of the contact stress. That is, the source term in the

quasi-3D heat equation requires re-evaluation.

The heat exchange at the gap interface was assumed to be a combination of convection and radiation. An equivalent convection heat transfer coefficient was estimated using empirical relations at room temperature, and not allowed to vary. This does affect the transient behavior as well as the equilibrium condition in the computational model.

There is an implicit assumption in the formulation given in this dissertation, namely, that the contact between the pin and bushing, along the axial direction, is uniform and free of edge effects. This may not be true as the pin is mounted as a cantilever beam and will deflect when heavily loaded. Precautions were taken to minimize misalignment by means of ball bearings on which the housing rested and with the use of linear bearings on which the stabilizing cartridge could float vertically. Surface waviness in the pin and bushing is also a contributing factor to a non-continuous contact. The heat flux distribution along the contact length is greatly affected by misalignment. If for instance, the pin axis is wobbling around its undeflected axis of rotation, the heat flux input is led to be intermittent, and limited to smaller contact length.

It is observed that the computed temperature rise in the production pin-bushing pair exhibits a slower rise-time at the start of the transient stage than the measured one. While the opposite occurs in the case of the production pin-bushing pair. This may be attributed to the coating layer at the inner wall of production bushing blocking or delaying heat transfer into the bushing medium.

Verification of the experimental results (or theoretical results) presents a challenging problem because of a number of modeling issues. Mathematical modeling alone is not sufficient to completely describe the frictional mechanism and the underlying thermal dynamics in the pin-bushing assembly. Special experimentation must be designed to uncover key process characteristics, and eliminate uncertainties. In addition, Hertz theory is inadequate in representing

the pin-bushing contact configuration and an alternative theory is needed. Conformal contact theory is believed to be a better alternative especially when the contact angle subtends values that are larger than 20 degrees as was discussed in Chapter 9. Calculations in the next chapter make use of the conformal contact theory.

Chapter 12. Analysis of Variance of the Thermal Behavior in Conformal Pin-Bushing Contact Undergoing Oscillatory Sliding with Friction

The complexity of the interface temperature prediction is hampered by additional complications arising from variables such as contact stress, speed of relative motion, material shear strength, lubrication system, surface finish, loading conditions, heat dissipation, and other operating conditions. Laboratory tests and field experience reveal that the key parameters that influence interface temperature include the applied load, the rotational speed, the amplitude of oscillation, the radial clearance ratio (radial clearance to pin radius ratio), and busing aspect ratio (bearing length to pin diameter ratio). Detailed simulations under particular geometry and operating conditions are useful; however they do not provide overall evaluation of the cumulative effect of all the factors and their interactions. In order to understand the overall effects of various process parameters on the surface temperature rise and identify the key controlling variables, it is necessary to investigate the factors of influence and to assess their effects statistically.

A recent study by Wang et al. [45] considered five factors that characterized the steady state surface temperature rise at the contact interface of heavily loaded pin-bushing joints undergoing oscillatory sliding motion with friction, and relied on the Pearson's correlation coefficient. In that study, the parameters considered pertinent are: the applied load, the driving motor speed, the amplitude of oscillation, the pin-bushing clearance ratio, and the bushing aspect ratio. A range of such pertinent parameters was considered for the purpose of assessing their effects on the maximum steady state surface temperature rise.

In the present chapter, the work in [45] is extended to include a factorial analysis of variance. The goal of this chapter is to identify and quantitatively estimate such parameter effects

on a characteristic design response. The maximum interface temperature at steady state is used as the pertinent response. The assessment of parameter effects can be done by a factorial analysis of variance, which allows for the study of various factor effects simultaneously on simulated response data. The response is computed using the finite element method. This technique has been has been used by Zhang et al. [46] in the Numerical analysis and optimization of hemming processes based on the notion "Design and Analysis of Computer Experiments (DACE)" method of Sacks et al. [47]-[48], Mansouri et al.[49] in the thermal behavior in wet clutch engagement, and by numerous others.

A study of the influence of temperature on the tribological behavior in machinery components with friction requires prediction of the contact surface temperature. The surface temperature is controlled by a number of design factors such as operating conditions, geometric parameters, and materials properties. A correlation between the surface temperature and such design parameters would provide a basis for predicting performance and guarding against failure. Mansouri and Khonsari [43] developed a transient two-dimensional thermal model for predicting the temperature rise in two sliding bodies undergoing oscillatory relative motion. The thermal model is capable of predicting transient temperature distribution on the pin-bushing joints. The solution was computed numerically using the finite difference method and then using the finite element method. The finite element model will be used here to study the effect of selected key parameters on the surface temperature rise at steady state using a factorial analysis of variance.

The configuration of a typical pin-bushing joint was illustrated and the mathematical model for the thermal problem formulated in Chapter 8. A sustained oscillatory motion is assumed and expressed by the time function $\phi(t) = \phi_m \sin(\omega t)$, where the angular frequency is given by $\omega = 2\pi \mathrm{N}/60$, ϕ_m is the amplitude of oscillation, and N is the rotational speed of the DC

Motor. The external load, applied vertically to the pin, is considered to be constant for simplicity. The transient temperature distribution is governed by equation (77), where the temperature field $T\left(t,\mathbf{r}\right)$ is assumed to be a function of time and position $\mathbf{r}=\left(r,\theta\right)$. The pin rotates while the bushing is mounted on a stationary housing. The steady-state thermal problem is derived by setting time derivatives to zero. In addition, the sinusoidal speed and the heat flux are set at their mean values computed over one cycle of oscillation. The resulting governing equation reads:

$$k\nabla^2 T + q_b\left(\mathbf{r},T\right) = m\rho c\dot{\phi}_a \frac{\partial T}{\partial \theta} \tag{149}$$

Boundary Conditions

The boundary conditions involve heating due to friction and convection at the sliding interface, and convective cooling at the surface of the housing exposed to the surrounding air. In addition, coupling condition of temperature continuity at the contact interface is enforced. Convective heat transfer coefficients with the surroundings and within the gap interface are estimated using known empirical relations as detailed in the appendix. The boundary conditions given in Chapter 8 remain unchanged. The conformal contact model is used to compute the contact pressure and heat flux input, as described in detail in Chapter 6. The average value of the angular speed in zero and the convection term in the steady state equation vanishes. In the steady state problem, the heat flux is set to its mean value over one complete cycle, thus

$$\widehat{q}_c = \mu_c p_c(\theta)\left(2/\pi\right) v_m \phi_m \tag{150}$$

where $v_m = r_s\omega$ is the maximum linear sliding speed. Figure 82 illustrates the contact pressure for two cases of load and geometry; see Table 5 for input data for runs 7 and 16. A comparison to the classical Hertz theory is also shown. As the true contact angle increases, Hertz theory underestimates the contact width, and overestimates the maximum pressure, and the

pressure profile falls off more rapidly near the contact edges [42]-[43]. In addition, Hertz theory assumes that the contact width is small compared with the radius of the pin-bushing cavity whereas the conformal contact theory does not have this restriction.

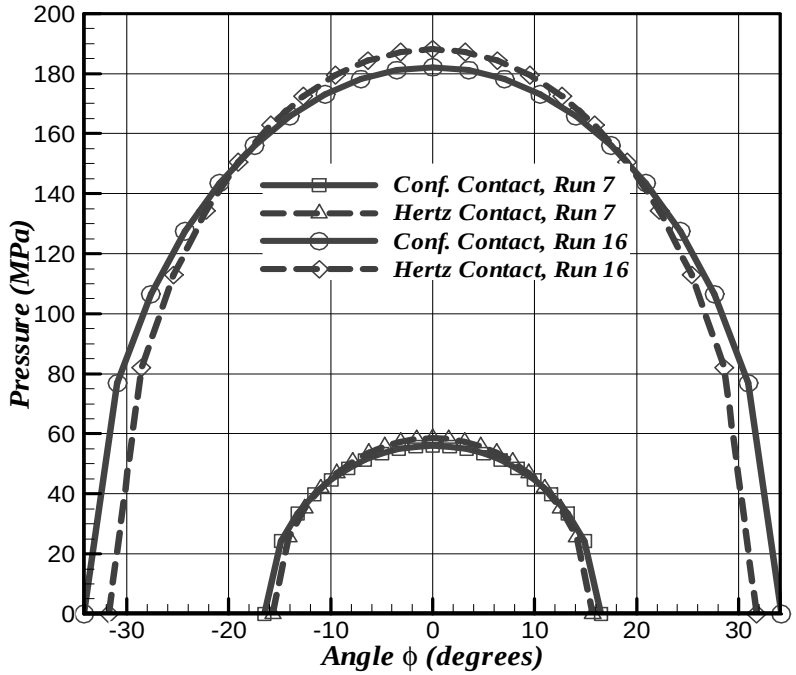

Figure 82. Conformal versus Hertz theories.

The Finite Element Solution

The solution is carried out using the finite element discretization in space, and the Newton Raphson method for solving the resulting nonlinear algebraic equations. Sharp changes in the solution gradients and material discontinuity are handled using adaptive meshing, see Figure 83. This is especially important at the contact interface.

Factorial Design

Laboratory experiments on a number of grease lubricated pin-bushing pairs under different loads and speeds revealed that the coefficient of friction is typically μ_c = 0.12. The

ambient temperature and heat transfer coefficient are set to room temperature T_e = 25 ^oC and h_e=100 W/m^2.K.

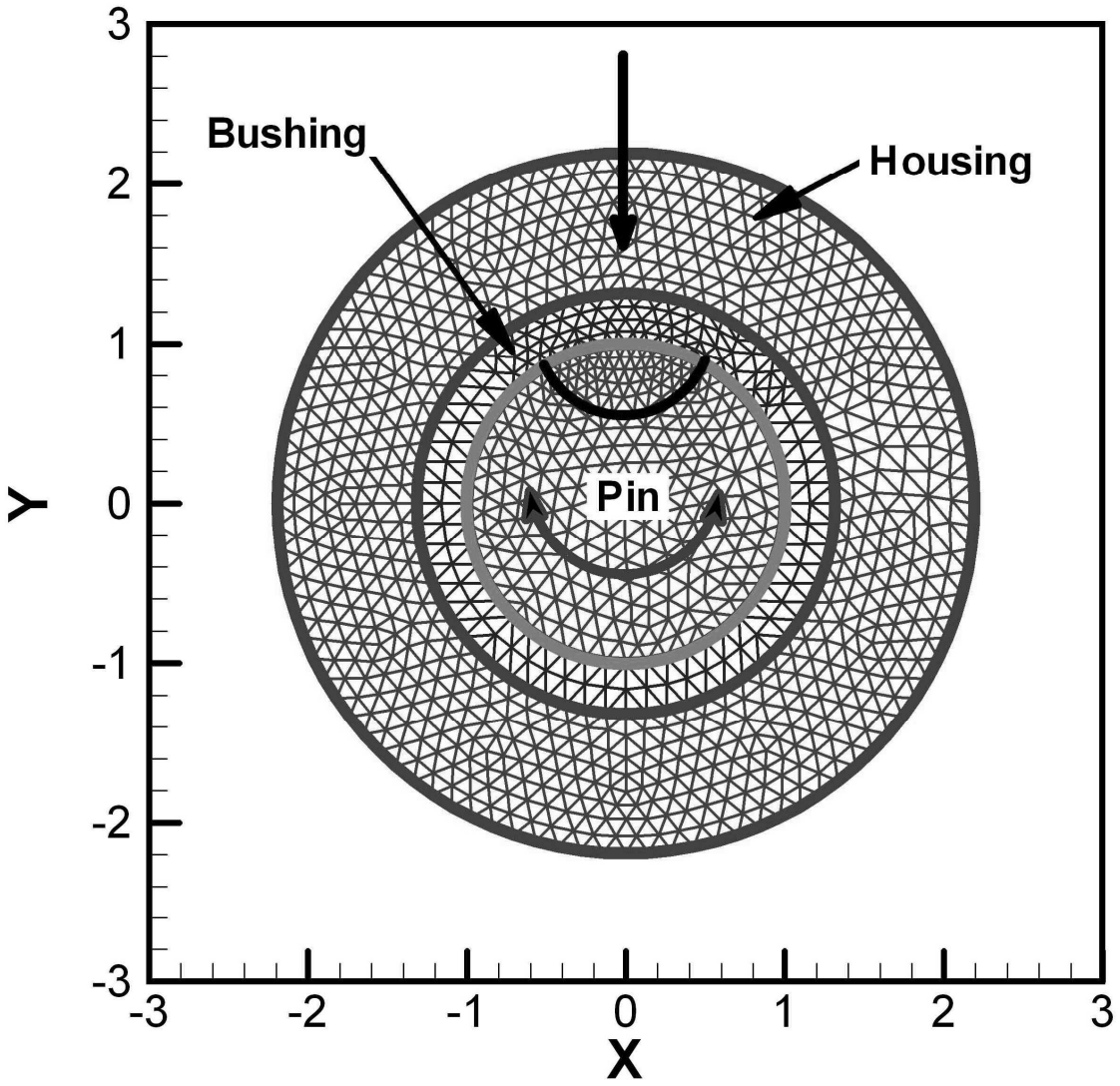

Figure 83. Typical finite element mesh for the pin-bushing.

The present study is limited to eight pin-bushing pairs whose geometric parameters are described by a clearance ratio, C_r, and aspect ratio, A_r, set at two levels $C_r = 0.00378,\ 0.00601$, $A_r = 0.72,\ 1.24$. The applied load, speed, and oscillation amplitude are set to low and high levels as follows: $w_a = 400,\ 2600$ kN, $\mathrm{N} = 0.25,\ 8$ rpm, $\phi_m = 6,\ 60$ degrees. Material properties are assumed to be independent of temperature.

Simulations were performed for a two-level half-fractional factorial design since the goal was to identify and rank the factors influencing the steady state maximum contact temperature rise. This calls for a set of $2^{(5-1)}$ =16 simulations (runs). Table 5 shows a listing of the factor level combinations and corresponding responses.

Table 5. Fractional factorial design matrix & response

Run No.	Applied Load (kN)	Rotational Speed (rpm)	Amplitude (deg °)	Clearance ratio (x 10^{-3})	Bushing Aspect ratio	Maximum Surface temp. rise (^{o}C)
1	L	L	L	L	H	0.246
2	H	L	L	L	L	1.525
3	L	H	L	L	L	12.106
4	H	H	L	L	H	32.858
5	L	L	H	L	L	3.777
6	H	L	H	L	H	10.273
7	L	H	H	L	H	78.788
8	H	H	H	L	L	487.864
9	L	L	L	H	L	0.4175
10	H	L	L	H	H	1.165
11	L	H	L	H	H	8.627
12	H	H	L	H	L	55.378
13	L	L	H	H	H	2.697
14	H	L	H	H	L	17.312
15	L	H	H	H	L	133.477
16	H	H	H	H	H	371.073
L	400	0.25	6	3.78	0.72	0.246
H	2600	8	60	6.01	1.24	487.86

The statistical effects of the selected factors on the temperature response are evaluated by the primary factor effects and their interactions. The main effect of a primary factor is defined as the change in response produced by a change in the factor level, and is used to compare the relative strength of the effects across factors. For instance, the effects of the applied load, speed, and oscillation amplitude, acting alone, are considered main effects in the pin-bushing experiment, and must be included in the analysis. It is quite conceivable that the difference in

response between the levels of one factor is not the same at all levels of other factors; this shows the presence of interactions between factors. For instance, the effect of the speed on the temperature response at low levels of the amplitude or the applied load may be quite different when the response is observed with the amplitude and/or the applied load set at their high levels. This indicates that there are interactions between the speed, the amplitude, and the applied load. This means that the main effects alone cannot explain the variation in the response, and those interactions effects must be considered in the analysis. Only main and two-factor interaction effects are considered in this study. This is in accordance to the sparsity-of-effects principle [50]. The sparsity-of-effects principle refers to the idea that only a few effects in a factorial experiment will be statistically significant. More specifically, the sparsity-of-effects principle states that a system is usually dominated by main (single factor) effects and low-order (two-factor) interactions. In other words, higher order interactions such as three-factor interactions are not likely to be significant rare. Under these assumptions, the response may be expressed by a linear regression model is of the form:

$$\widehat{y} = \big(\text{Overall mean}\big) + \big(\text{main effects}\big) + \big(\text{interation effects}\big) + \big(\text{error}\big).$$

Mathematically, this is written in general as follows:

$$\widehat{y} = \mu_0 + \sum_i c_i x_i + \sum_{i,j} c_{ij} x_i x_j + \varepsilon$$

where $\widehat{y}$ is the response mean, c_i, c_{ij} are coefficients to be determined, and x_i the primary factors. The summation indices in the above equation run over the range of main and interaction effects, respectively. The parameter μ_0 is estimated by the average of all responses, and the last term is an algebraic error term.

Factorial Analysis and Discussion

The factors and response data were analyzed to screen out insignificant factors, identify significant factors, and assess the existence of interaction. The insignificant factor effects are commonly screened out with the help of a normal plot of effects estimates, Figure 84. This is a plot of the values of the effects estimates versus their commutative normal probability. A confidence level of $\alpha = 0.05$ is considered for the analysis. The confidence interval for predicted values is the range in which the estimated mean response for a set of predictor values, factor levels is expected to fall. The interval is defined by lower and upper limits, calculated from the confidence level and the standard error of the fits. The statistical tool Minitab (Minitab Inc.) is used as an analysis and assessment tool. The factor labels assigned by the analysis tool (A, B, C, …) are convenient because they represent actual or coded values.

The following observations are made based on inspection of the normal plot of effects.

- Main effects due to the applied load **(A, w_a)**, speed **(B, N)**, and amplitude **(C, ϕ_m)** are most significant, followed by the aspect ratio **(E, A_r)** and clearance ratio **(D, C_r)**.
- Interactions effects between the applied load, the speed, the amplitude, the clearance ratio, and the aspect ratio are significant as they appear to fall off the zero-effect probability line as seen in Figure 85.

Analysis of variance helps to quantify the effects. Also, it is utilized to fit a reduced model for the prediction of the maximum steady state surface temperature rise. Table 6 presents a summary of such analysis [50]. Large model F-value implies the model term have significant effects. Small P-values ("Prob > F" less than 0.05) indicate that the terms are significant. In this case the applied load A, the driving speed B, the oscillation amplitude C, and the interactions AB, AC, BC, and DE are significant terms.

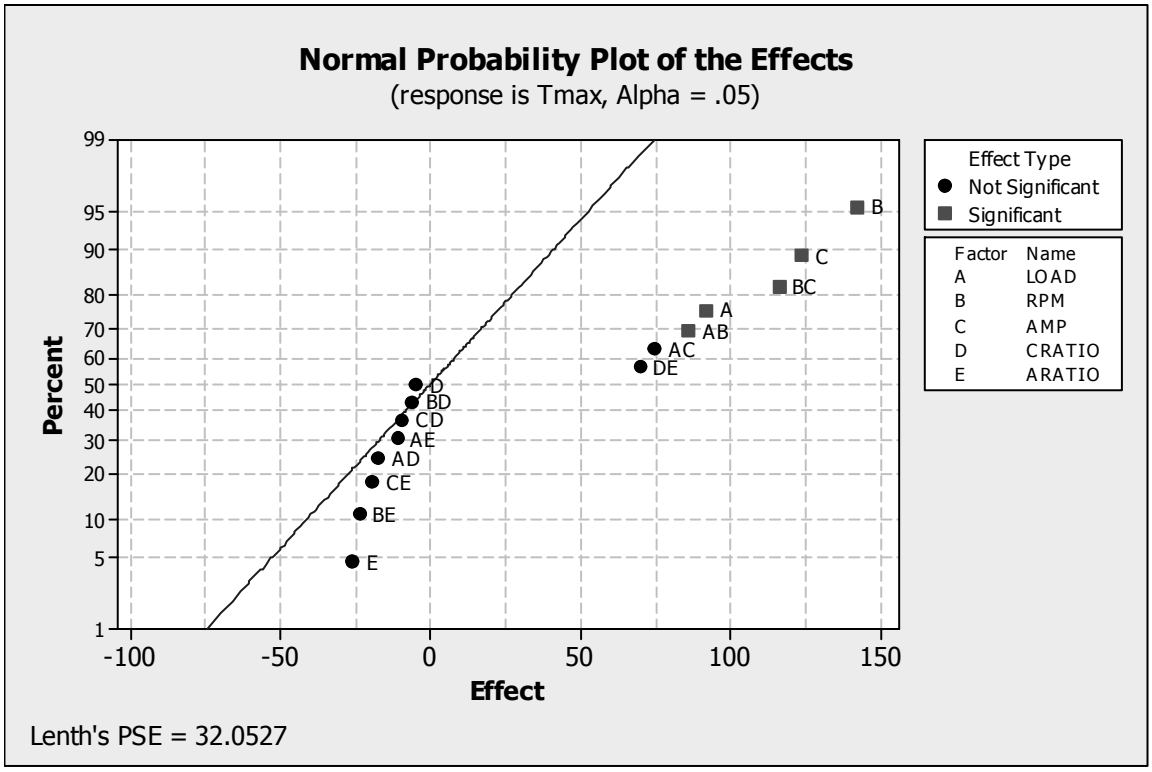

Figure 84. Normal plot of effects estimates

Table 6. Estimated Effects and Analysis of Variance

Term	Effect	F	P
Intercept		34.83	0.0002
Load (A, w_a)	98.39	34.80	0.0011
Speed (B, N)	149.15	83.60	<0.0001
Amplitude (C, ϕ_m)	129.78	63.11	0.0002
Clear. ratio (D, C_r)	-7.98	0.089	0.7755
Asp. ratio (E, A_r)	-29.61	2.72	0.1502
AB, w_aN	92.31	30.57	0.0015
AC, w_a ϕ_m	80.11	22.91	0.0030
BC, Nϕ_m	121.84	55.55	0.0003
DE, C_rA_r	75.11	20.08	0.0042

The relationships between the design/operating factors and the surface temperature response was evaluated in [45] using the Pearson's correlation coefficient. While that study gave assessment of main factor effects that are consistent with the present analysis, it did not assess interaction effects. By definition, the Pearson's correlation is a measure of a linear relationship between two variables. As revealed by the present analysis, some factors may not be significant

when acting alone, but have significant influence on the response when other factor levels are considered.

The main effects plots, illustrated in Figure 85, show that the applied load, rotational speed, and oscillation amplitude have an increasing effect on the surface temperature rise, while the clearance and aspect ratios have the opposite effect. The applied load, rotational speed, and oscillation angle are found to be the dominant factors that influence temperature rise; the clearance ratio and bushing aspect ratio have relatively lesser effects on the interface temperature rise. Obviously, the clearance ratio effect is the least significant. The reason is that the applied load and the oscillating sliding speed are the two major contributing factors to the frictional heat flux applied at the interface. The motor rotational speed and the amplitude angle are related to the sliding speed. The larger of the amplitude angle with the speed held constant, the higher of the sliding speed. The observation that the clearance shows little effect on the temperature rise is partly due to the small range of the clearance applied in the tribological system and the fact that clearance affects the distribution of the stress and area of contact in such a way as to increase the mean contact pressure and reduce the contact width. The net effect is a larger heat flux applied to a smaller area. From a practical viewpoint, it should be noted that large clearance would allow the lubricant to access the pin/bushing interface, thus reducing friction. Thermoelastic effects were not treated in this study, but it is believed that thermal expansion has a major influence on the clearance ratio, and therefore the surface temperature [51]. It is noteworthy that the range of clearance simulated in this study may be too restrictive to generalize the conclusion concerning the clearance ratio.

The relatively minor effect of the aspect ratio on the surface temperature response can be explained by its minor involvement in influencing the contact pressure in the line-contact model. A simplified contact model has been considered, which does not account for the nonlinear nature

of the mechanical and thermal contact interface and plays a major role in influencing the interface boundary conditions and therefore the response. If we consider only the primary factors effects then we would run the load, speed, and amplitude at their low levels and the aspect ratio at its high level in order to reduce the surface temperature rise. However, it is always necessary to examine the data for the presence of interactions and assess their importance.

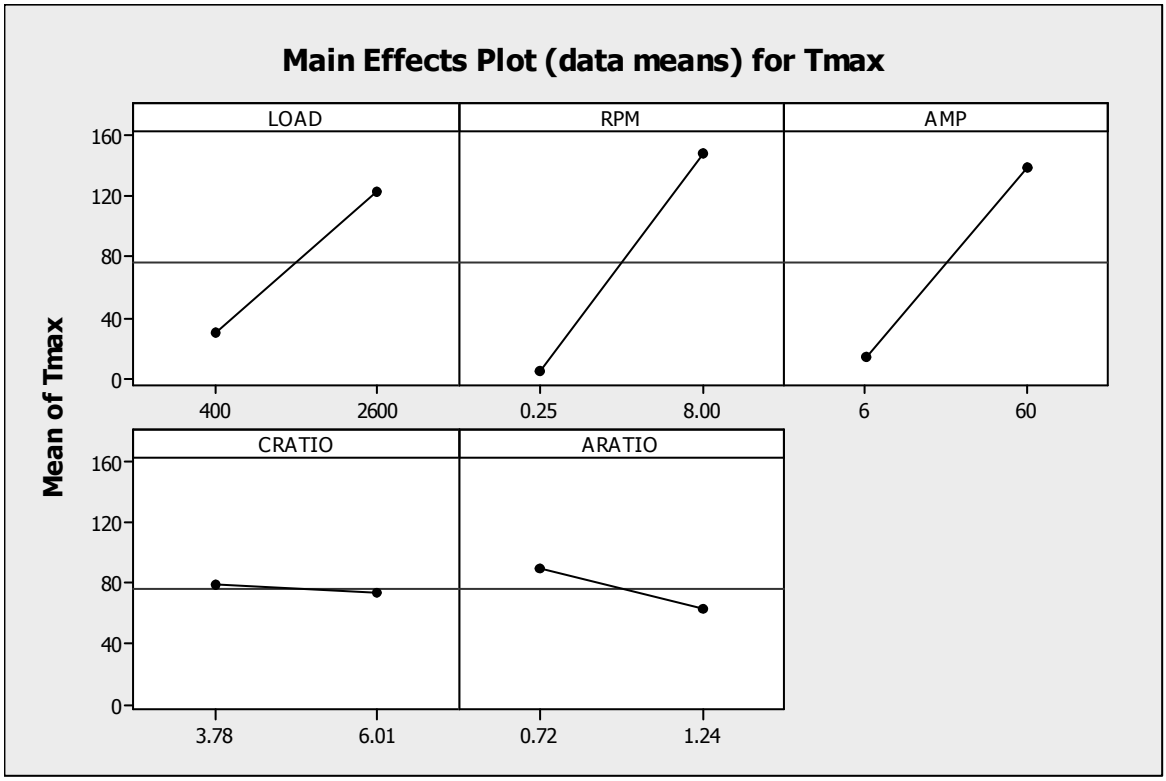

Figure 85. Main effect plots for the response mean.

The interactions plots, in Figure 86, indicate that the effects of load, speed, amplitude, the clearance ratio and aspect ratio are affected by the levels of the five factors. This is indicated by the non-parallel lines. Parallel lines in the two-factor interaction plots indicate the absence of interaction. The most significant interactions are those between the speed-amplitude interaction with a contribution of 17.6%, followed by the load-speed interaction with a contribution of 9%, the load-amplitude interaction at 7%, and lastly the clearance-aspect ratios interaction with 6%

contribution. The clearance and aspect ratios acting alone with all other factors fixed at the center, both have less than 1% contribution to the surface temperature rise. However, they had to be included in the analysis in order to keep model hierarchy. Interaction plots also show that severe operating conditions (high surface temperature) occur when the applied load, speed, and amplitude of oscillation are simultaneously set to their high levels. Interaction between the clearance and aspect ratios has a favorable effect when the two factors are both set at high levels.

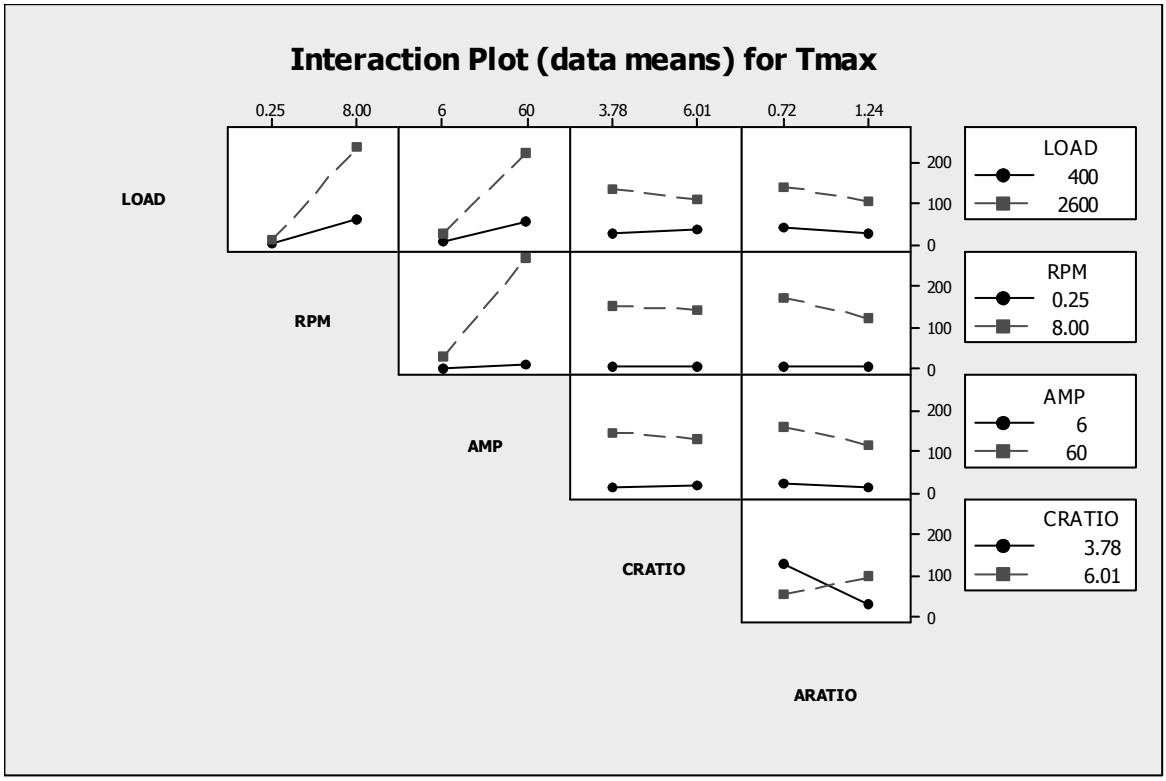

Figure 86. Interaction plots for the response mean

Table 7 presents estimated coefficients $\{c_i,\ i = 0,1,2,...15\}$ for a linear reduced model representing a factorial fit of the response data. Only the main and second-order interaction terms are considered, and all higher-order terms are neglected. The prediction model is written as follows:

Table 7. Coefficients of reduced model

Term	Normalized Coefficients	Actual Coefficients
Intercept	76.10	489.708
Load (A, w_a)	46.08	0.0116408
Speed (B, N)	71.42	-0.193309
Amplitude (C, ϕ_m)	62.06	0.212245
Clear. ratio (D, C_r)	-2.33	-101.833
Asp. ratio (E, A_r)	-12.88	-518.713
AB, w_aN	43.19	0.0101325
AC, $w_a\phi_m$	37.39	0.00125895
AD, w_aC_r	-8.62	-0.00702667
AE, w_aA_r	-5.46	-0.0190762
BC, Nϕ_m	58.22	0.556467
BD, NC_r	-3.05	-0.706373
BE, NA_r	-11.80	-11.7139
CD, ϕ_mC_r	-4.69	-0.155690
CE, ϕ_mA_r	-9.57	-1.36278
DE, C_rA_r	35.01	120.749

$$T_{\max}^{pred} = c_0 + c_1\mathrm{A} + c_2\mathrm{B} + c_3\mathrm{C} + c_4\mathrm{D} + c_5\mathrm{E} + c_6\mathrm{AB} + c_7\mathrm{AC} + c_8\mathrm{AD} + c_9\mathrm{AE} + c_{10}\mathrm{BC} + c_{11}\mathrm{BD} + c_{12}\mathrm{BE} + c_{13}\mathrm{CD} + c_{14}\mathrm{CE} + c_{15}\mathrm{DE} \quad (151)$$

The actual coefficients must be used with the following units: Load A (kN); rotational speed B (rpm); amplitude angle C (degrees); clearance ratio D ($x10^3$); and aspect ratio E. The coded (or normalized) coefficients given in Table 6 must be used with coded factor values; that is low levels (-1), high levels (+1), and zero at the center levels. The reduced model accuracy depends on how good the coefficients estimates are. Although predicted values may fall within the model prediction interval, the reduced model should be used with caution as it may underestimate or overestimate the response, and even yield non-physical values. It is important to realize that the model equation (151) is valid only within the range of factor data investigated. The correlation coefficient describing the prediction model goodness of fit is R^2 = 98.12% (adjusted value R^2 (adj) = 95.30%). To demonstrate the effectiveness of the prediction model, some examples are presented below.

Application Examples

The following examples demonstrate the utility of the prediction model (151) in design space. The goal is to choose the proper geometry (bushing clearance ratio, aspect ratio) or operating parameters (applied load, motor speed, etc.) in order to keep the operating surface temperature below a desired limit.

Example 1. Response Prediction

Predict the maximum steady state surface temperature rise at the interface of a pin-bushing pair whose material properties are those of steel, and geometry defined by a pin diameter of 160 mm, bushing diameter of 160.78 mm, bushing length = 156.8 mm, thus the pin-bushing clearance ratio is 4.895 x 10^{-3}, and the aspect ratio is 0.98. Assume that the load is 1500 kN, the motor speed is 4.125 rpm, and the amplitude of oscillation is 33 degree. The simulated surface temperature rise is $T_{\max}^{sim}$ = 79.35 ^{o}C, while the predicted value using equation (151) is $T_{\max}^{pred}$ = 76.10 ^{o}C, with a prediction error of ~ -4%.

Example 2. Aspect Ratio

Choose the bushing aspect-ratio for a heavily loaded pin-bushing pair such that the maximum steady state surface temperature rise remains below 150 ^{o}C. The applied load is 2000 kN, the speed is 4 rpm, the amplitude of oscillation is 45 degrees, and the clearance ratio is 4x10^{-3}. Using Equation (151) with the actual coefficients (Table 7), leads to the range $A_r \geq 1.065$ for the aspect ratio. The predicted response, using the above input parameters with $A_r = 1.1$ is $T_{\max}^{pred}$ ~ 113 ^{o}C. Simulation yields $T_{\max}^{sim}$ ~ 112 ^{o}C, which is within the desired range with an error of < 1%.

Example 3. Applied Load

Determine the maximum applied load that is to carried by a pin-bushing pair such that the maximum steady state surface temperature rise remains below 300 ^{o}C. The speed is 8 rpm, the amplitude of oscillation is 45 degrees, the bushing aspect ratio is 1.0 and the clearance ratio is $4x10^{-3}$. Using Equation (151) with the actual coefficients (Table 7), leads to the range $w_a \leq 2453$ kN for the applied load. The predicted response, using the above input parameters with $w_a = 2400$ is $T_{\max}^{pred}$ ~ 294 ^{o}C. Simulation yields $T_{\max}^{sim}$ ~ 276 ^{o}C, which is within the desired range with an error of ~ 6.5%.

Example 4. Rotational Speed

Determine the speed such that the maximum steady state surface temperature rise remains below 150 ^{o}C. Consider a pin-bushing pair designed to operate under an applied load of 1000 kN, oscillating at an amplitude of 45 degrees, with bushing clearance and aspect ratios of 4 x 10^{-3} and 0.75 respectively. Substituting above numbers into the model equation (151), gives the range $N \leq 5.7$ for the speed (rpm). The predicted response, using the above input parameters with $N = 4$ rpm is $T_{\max}^{pred}$ ~ 110.5 ^{o}C. Simulation yields $T_{\max}^{sim}$ ~ 118.4, which is within range with an error of ~ 6.6%.

The accuracy of the parameters determined in the design space such as in Examples 2 and 3 above depends strongly on their effect contribution to the response variable. Thus, if the effect contribution is significant in changing the model response, then the error in estimating design parameters is significantly reduced. In addition, the range of temperatures used in the design examples depends on the capacity of the factors and their interactions to exert change in the response variable as seen on the main and interaction plots. The reason for error is the added uncertainty involved in predicting a single response versus the mean response used in the

regression fit. For safe operation, a generous safety margin should be applied to avoid failures. It is believed that an experiment design with replicates, augmented with center points, would considerably improve the prediction model. Nevertheless, an error of 5% to 10% is thought to be reasonable for the analysis under consideration.

Concluding Remarks

A factorial design was used to investigate the temperature response at different operating conditions and geometric parameters. The factors of interest include the applied load, the driving motor rotational speed, the amplitude of oscillation angle, the clearance ratio, and the bushing aspect ratio. Analysis of variance was used to quantify the effects contributions. Our study indicates that the dominant factors affecting interface temperature are: the speed with 26% contribution, followed by the amplitude of oscillation, 19%, and the applied load, 10%. It was found that while the clearance and bushing aspect ratios have relatively minor contributions (less than 1%) to the temperature rise when acting alone within the range of geometry and operating conditions under investigation, their interaction effect is however significant with a contribution of 6%. A regression model is used based on the main and second-order interaction effects within the factors range considered. This prediction model predicts the surface temperature with reasonably good accuracy and can be useful for design purposes as was shown by example. While the prediction model is demonstrated for new observations limited to the factor range under investigation, extrapolation to predictions outside of this range should be tested which would add to its usefulness. Further, it is recommended that a wider range of clearance and aspect ratios be considered as these parameters affect the contact behavior and therefore the heat flux input.

Chapter 13. Conclusions and Recommendations

The following discussions and recommendations are relevant aspects to this research that are believed to be useful for future work.

Effect of Material Properties

In the work in [45], which was discussed and extended to include a factorial analysis of variance in the previous chapter, five key factors that influence the surface temperature rise at steady state were considered for analysis. The pertinent parameters included operating parameters, namely the applied load, the speed, and the amplitude, and geometric parameters, namely the bushing clearance ration and aspect ratio. Thermal and elastic material parameters of the contacting bodies were not considered. In practice, it is likely that the two parts in contact are made of different materials. The effects of material properties of the contacting bodies or coating that may be present are very important and must be considered for analysis.

The previous analysis was based on the solution of the steady state problem. This assumption took away the terms in the heat equation that are explicitly dependent on the amplitude and speed of oscillation. Thus, a time dependent solution is required in order to obtain a more accurate assessment of the factor effects.

The governing equations and boundary conditions for the pin-bushing joint were given in Chapter 8 for the thermal problem and Chapter 9 for the conformal contact model. Repeated here for convenience, recall from Chapter 8 that, the dimensionless boundary condition at the sliding interface is

$$K\frac{\partial \Theta}{\partial n} + Bi\Delta\Theta = Bi_e Q \tag{152}$$

$$K = k/k_r\,,\; Bi = hr_s/k_r\,,\; Bi_e = h_e r_s/k_r \tag{53}$$

where the reference thermal conductivity is that of the moving part. The dimensionless heating and cooling fluxes at the interface are described by

$$Q = \begin{cases} Q_c & \left|\theta - \phi_c\right| \le \alpha \\ 0 & Otherwise \end{cases},\; B_i = \begin{cases} 0 & \left|\theta - \phi_c\right| \le \alpha \\ B_{ig} & Otherwise \end{cases} \tag{154}$$

$$Q_c = q_c/q_r = \mu_c P_c \left|V(\tau)\right|,\; Bi_g = h_g r_s/k_r \tag{155}$$

The heat equation in dimensionless form is:

$$P_e \frac{K}{\Lambda}\frac{\partial \Theta}{\partial \tau} + mP_e \frac{K}{\Lambda}\phi_m \dot{\Phi}(\tau)\frac{\partial \Theta}{\partial \theta} = \nabla\bullet\left(K\nabla\Theta\right) + B_{ie}Q_b \tag{156}$$

where

$$Q_b = \frac{r_s q_b}{q_r} = -\frac{2h_e r_s}{Lq_r}\Delta T = -\frac{L_r}{A_r}\Theta \tag{157}$$

$$\Lambda = \kappa/\kappa_r\,,\; P_e = r_s^{\,2}\omega/\kappa_r \tag{158}$$

$$A_r = L_c/D\,,\; L_r = L_c/L \tag{159}$$

The length ratios $A_r,\; L_r$ are the bushing aspect ratio and the length ratio and represent ratios relative to the directions perpendicular to the sliding direction. The dimensionless cooling boundary condition at the outer surface is

$$K\frac{\partial \Theta}{\partial n} + B_{ie}\Theta = 0 \;\; :: \text{on } \mathrm{S_e} \tag{160}$$

The dimensionless form of the heat equation within the conducting media and the boundary conditions are clearly defined by the dimensionless thermal material properties. In order to assess the effect of thermal properties on the surface temperature, the ratios of thermal conductivities and thermal diffusivities must be considered as pertinent factors influencing surface

temperature rise.

The dimensionless contact parameters were given in Chapter 9, and are rewritten here for clarity. The following dimensionless equations are based on conformal contact theory.

$$P_c = \frac{2}{\left(1+C_r\right)}\left[\frac{2\sqrt{\beta^2-\xi^2}}{\pi\sqrt{1+\beta^2}\left(1+\xi^2\right)}+\frac{f_c(\beta,\xi)}{2\pi\beta^2\left(1+\beta^2\right)}\right] \tag{161}$$

$$f_c(\beta,\xi) = \ln\left[\frac{\sqrt{1+\beta^2}+\sqrt{\beta^2-\xi^2}}{\sqrt{1+\beta^2}-\sqrt{\beta^2-\xi^2}}\right] \tag{162}$$

$$\frac{2\beta^4+2\beta^2-1}{\beta^2\left(\beta^2+1\right)} = g_c\left(\beta\right) \tag{163}$$

$$g_c\left(\beta\right) = \frac{2\left(1+E_p\right)-\nu_p E_p}{1+E_p} - \frac{\pi M_s C_r}{2\left(1+E_p\right)} + \frac{2}{1+E_p}\frac{\left(1+C_r\right)}{2}\int_{-\beta}^{\beta}\frac{P_c\left(\xi\right)d\xi}{1+\xi^2} \tag{165}$$

The dimensionless modulus of elasticity M_s of the pin is defined as: $E_s = p_l M_s$. The dimensionless frictional heat flux distribution is given by

$$Q_c = \mu_c\frac{2}{\left(1+C_r\right)}\left[\frac{2\sqrt{\beta^2-\xi^2}}{\pi\sqrt{1+\beta^2}\left(1+\xi^2\right)}+\frac{f_c(\beta,\xi)}{2\pi\beta^2\left(1+\beta^2\right)}\right]\phi_m\left|\dot{\Phi}\right|\left|\cos\left(\phi_m\Phi\right)\right| \tag{166}$$

It is clear that the elastic material properties of the contacting bodies will greatly influence the contact pressure and contact width, and therefore the resulting frictional heat flux and surface temperature. In order to assess this effect, the elastic modulus of elasticity parameter, $E_p = E_2/E_r$, is considered in the factorial analysis of surface temperature.

Based on the above formulation, there are eight pertinent bulk parameters influencing the dimensionless surface temperature are:

1. The applied load, w_a,

2. The angular frequency, ω

3. The amplitude of oscillations, ϕ_m

4. The thermal conductivity ratio, $K = k/k_r$

5. The thermal diffusivity ratio, $\Lambda = \kappa/\kappa_r$

6. The elastic modulus ratio, $E_p = E/E_r$

7. The clearance ratio, $C_r = C/r_s$

8. The aspect ratio, $A_r = L_c/2r_s$

A full factorial analysis of the eight factors effects requires 256 runs, which is too large in practice. A half-fractional factorial analysis calls for 128 runs. For a time dependent solution that must be carried out until a steady state is reached, the computational time for this many runs may be prohibitive. One way to reduce the number of simulations is to fix one or more of the parameters defining the key factors listed above.

Temperature, Friction, and Wear Correlation

In machinery with sliding contact such as dry sliding bearings and pin-bushing joints and the like, the interface temperatures has major effects on the friction and wear behavior of the contacting surfaces and determines the functional limit of the tribo-system [56]. For instance, galling and scuffing of machine elements have been found to be related to interfacial temperature. Galling occurs when the temperature at the sliding interface reaches an upper limit for the lubricating film or the surface materials, leading to thermal degradation of any boundary lubricant film and eventual material transfer [57]. On the other hand, wear alters the interfacial area. As a result, the heat flux input and therefore the surface temperature are affected.

Therefore, there is a need to for a correlation between surface temperature, friction and wear in order to assess the likelihood of system failure due to thermal effects.

Studies to determine the influence of surface temperature on friction and wear have been reported in the literature for polymer/metal sliding bearings in unidirectional [58] and oscillatory [59] sliding. Such studies were experimental in nature; the surface temperature was controlled by changing the bulk temperature of the contacting body. Relationships were developed between that temperature and measured friction and wear, at various sliding velocities and contact pressures. However, the contact temperature is not readily controllable or predictable as it depends on the contact size and shape, and other parameters including the coefficient of friction, the applied load, the sliding velocity, and the thermal properties of the contacting bodies at the interface.

Floquet and Play [33] used the infrared thermocouple technique to measure the surface temperature in unidirectional sliding of dry bearings, and developed analytical methods for predicting the surface temperature distribution resulting from frictional heating. Kennedy et al. [12] used a similar technique to investigate the relationship between the contact temperature rise and the friction and wear rate for the case of dry sliding between a pin and flat in oscillatory motion. The finite element method model was used to predict the surface temperature in an oscillatory contact. The prediction model was validated by comparison to temperature measurements in an oscillatory pin-on-flat contact using infrared radiometry. The predicted surface temperature was then correlated with the measured coefficient of friction and wear rate. This technique was applied in [12] to correlate the contact temperature with friction and wear rate in an oscillatory pin-on-flat configuration where the contact was between a polymer and a stainless steel. It was found that the contact temperature increased with increasing frequency or amplitude of oscillation, while the resulting wear rate decreased. This is believed to be the result

of the transfer film smearing and covering rough surface asperities. The work in [12] also concluded that the influence of the contact temperature on friction was less clear and more intricate to explain.

Kannel and Barber [57] developed a simple model for predicting the steady state interface temperature in a sliding system under the condition in which wear alters the contact area in concentrated contact tribological applications. They showed that a peak interface temperature was reached after a finite number of cycles, and that interface temperature decreased as wear progressed. They state that systems prone to galling would fail during this initial peak temperature, but if the contact interface survived past this time period, it would most likely not experience failure by galling as the peak temperatures decrease as wear progressed.

The above studies indicate that a correlation between contact temperature and friction and wear rate may be developed by the use of finite element method for temperature prediction, and measurements of the friction coefficient and wear rate. The pin-bushing tribo tester, described in Chapter 3, is capable of friction and temperature measurements. Temperature measurements can be improved by positioning the thermocouples closer to the contact interface and by considering measurement locations distributed along the axial as well as the circumferential directions at the proximity of the contact interface. In the pin-bushing assembly, the pin and bushing hardened, but most of the wear occurs in the bushing. Thus, by weighing the bushing before and after experiments, the wear can be measured according the amount of material lost during each test.

Fretting is a type of wear that occurs wherever short amplitude oscillatory (repetitive) relative motion between contacting surfaces is sustained for a large number of cycles. The small relative motion can be caused by internal vibrations due to external mechanical excitation, or different thermal expansion of the contacting bodies.

Fretting results in damage in the form of surface wear and deterioration of fatigue life [60], [61]. Material damage caused by fretting wear is of significant concern in engineering applications. The fretting damage results from a simultaneous or sequential occurrence of two or more different wear processes, such as adhesion, oxidation, fatigue, and abrasion [62]. Fretting wear and fretting fatigue are present in almost all machinery and are the cause of total failure of some otherwise robust components. For instance, fretting occurs in applications such as aircraft components (e.g., bearings, hinges, seals, actuating devices, rocket propulsion fuel tanks, etc.) [63], automobiles, electrical contacts, and surgical implants [64]. Such contact vibrations are often induced by cyclic accelerations, cyclic stresses, acoustic noises, or thermal cycling [65]. The most common wear mechanisms are: melting wear, wear due to electric discharges, diffusive wear and impact wear. Melting wear is a direct result of frictional temperature rises and careful investigations reveal that it is much more common than widely believed, and is associated with low to moderate friction coefficients [60]. In this case, the fundamental unknown is the surface temperature generated by friction during fretting.

Greenwood and Alliston-Greiner [25], seeking solutions to surface temperatures in fretting contact, considered a simple analytical solution by ignoring the varying position of the slider for small amplitudes, and assuming that the slider takes no heat. They used Carslaw and Jaeger's approach [23] to obtain steady and periodic parts of the surface temperature at the center of contact. It was found the temperature of a small-amplitude oscillating contact quickly reaches a quasi-steady state consisting of a cyclic variation about a steady value that is equal to the response to a steady heating at the mean heat flux. It was found that at low frequencies, the maximum surface temperature is the same as the response of a unidirectional contact sliding at the maximum speed of the oscillatory contact. At high frequencies, the cyclic term becomes smaller and the temperature becomes almost independent of time.

Furey et al. [26] theoretically and experimentally examined surface temperatures in fretting contact between solids. A theoretical model and solution based on a full-space moving Green's function and the boundary integral equation method, were developed in order to predict the thermal response to frictional heating in systems with oscillating/fretting contact. The authors believed that knowledge of the surface temperatures produced during oscillating contact would shed light on the mechanisms of fretting wear and possibly ways to alleviate the problem.

In the case of the pin-bushing system, Fretting temperature analysis can be carried out using the finite element method and conformal contact model with small amplitude oscillatory contact. The time dependent solution must be carried out to steady state. Of interest in such an analysis is to determine the behavior of the predicted maximum steady state surface temperature rise for small amplitude contact oscillation, and how the amplitude interacts with other parameters to influence the thermal response. Small amplitude solutions require that the amplitude-to-contact half width be small compared to unity. The limiting case is the stationary problem solution (no oscillation); here, an equivalent heat flux is imposed at the contact interface for comparison with the transient steady state results.

Model Enhancements

- While axial averaging of the thermal problem resulted in a simpler quasi-three dimensional model, the magnitude of the resulting heat source is in error. The key source of the error in the axial averaging was the assumption that both ends of the components (the pin, the bushing, and housing) were exposed to ambient convective cooling. This explains much of the discrepancy between the measured and computed temperatures. However, due its additive nature, it provides room for adjustment. A method based on an overall algebraic error measure between the computed surface temperatures and the measured temperatures at the four

thermocouples is described in the appendix. Preliminary calculations using this method gave promising results. However, generalization to arbitrary pin-bushing pairs requires more research and numerical experimentation, and is therefore recommended for possible future work.

- The theoretical model for surface temperature rise can be enhanced by augmenting it with a dynamic coefficient of friction that takes advantage of the experimental data as well as existing theory. See the appendix for an example of a dynamic coefficient of friction model.
- Another enhancement is to consider thermal contact resistance at the contact junction and possibly at the bushing-housing interface. The models proposed in the appendix take into account the sliding effects, the surface roughness, and the nature of the fluid at the interface.
- The mathematical model did not take into account the thermal-mechanical interaction at the sliding interface. Clearly this is a key issue in the process. The heat flux in the oscillating pin-bushing problem is localized over one region of the interface. The thermal field is not axisymmetric. One way to treat the thermomechanical coupling is to consider the basic thermoelasticity equations in conjunction with load equilibrium as described in Chapter 6. This problem however is difficult to treat mathematically and numerically and special tools must be used to handle it. Such tools are in existence such as Abaqus and Ansys.
- A three-dimensional finite element analysis with a special tool that allows for the direct modeling of contact interactions (thermal and mechanical) may be necessary in order to capture modeling details such as misalignments and realistic heat transfer and thermal-mechanical interactions. The averaging scheme that was used is lacking in the way of end point boundary conditions.
- Solid coating films may be placed at the interface of the contacting components, such as on the inner wall of the bushing, in order to enhance wear properties and extend component life and

operational limits of the process. This provides a more realistic model for the production (hard-coated) bushing used in experiments. The addition of such coating layers does not alter the mathematical model much, and only some additional equations and boundary conditions are required to analyze the coating effect on the surface temperature.

References

[1] Bishop J.L. and McC. Ettles C.M. 1982, “The seizure of journal bearings by thermoelastic mechanisms”, *Wear,* 79, pp. 37-52.

[2] Ling, F. F., 1969, “On Temperature Transients at Sliding Surfaces,” *ASME Journal of Lubrication Technology,* 91, p. 397 - 405.

[3] Dyson A., 1979, “Scuffing”, *Treatise on Material Science and Technology,* 13, pp. 175-215.

[4] Dufrane K. and Kannel J., 1989, “Thermally induced seizures of journal bearings”, *ASME Journal of Tribology*, 111, p. 288-92.

[5] Khonsari M.M. and Kim H.J. 1989, “On thermally induced seizure in journal bearings”, *ASME Journal of Tribology*, 111, pp. 661-7.

[6] Hazlett T.L., Khonsari M.M., 1992 "Finite-element model of journal bearings undergoing rapid thermally induced seizure”, *Tribology International*, 25 (3), pp. 177-182.

[7] Wang H., Conry T.F. and Cusano C., 1996, “Effects of Cone/Axle Rubbing Due to Roller Bearing Seizure on the Thermomechanical Behavior of a Railroad Axle”, *ASME Journal of Tribology*, 118, pp.311-319.

[8] Wang H., 1996, “Axle Burn-off and Stack-up Force Analyses of a Railroad Roller Bearing using the Finite Element Method”. Ph.D. Thesis, Department of Mechanical and Industrial Engineering, University of Illinois at Urbana- Champaign, pp.140-147.

[9] Pascovici M.D., Khonsari M.M. and Jang J.Y., 1995, “On the Modeling of Thermomechanical Seizure”, *ASME Journal of Tribology*, 117, pp. 744-747.

[10] Krithivasan R, Khonsari M. M., 2003, "Thermally induced seizure in journal bearings during startup and transient flow disturbance", *Journal of Tribology – Transactions of the ASME*, 125 (4), pp. 833-841.

[11] Berthier, Y., and Play, D., 1982, “Wear Mechanisms in Oscillating Bearings”, *Wear*, 75, pp. 369-387.

[12] Kennedy F. E., Cullen S. C., and Leroy J. M., 1989, “Contact Temperature and Its Effects in an Oscillatory Sliding Contact”, *ASME Journal of. Tribology,* 111, pp. 63-69.

[13] Tian, X., and Kennedy, F. E., 1993a, ‘‘Contact Surface Temperature Models for Finite Bodies in Dry and Boundary Lubricated Sliding” *ASME Journal of Tribology*, 115, pp. 411-418.

[14] Tian, X., and Kennedy, F. E., 1993b, ‘‘Temperature Rise at the Sliding Contact Interface for a Coated Semi-Infinite Body, ’’ *ASME Journal of Tribology*, 115, pp. 1-9.

[15] Tian, X., and Kennedy, F. E., 1994, ‘‘Maximum and Average Flash Temperatures in Sliding Contacts’’ *ASME Journal of Tribology*, 116, pp. 167–174.

[16] Tian, X. and Kennedy, F. E. 1994, “Prediction and measurement of surface temperature rise at the contact interface for oscillatory sliding.” *Proc. Instn. Mech. Engrs.*, 209, pp. 41-51.

[17] Hirano, F. and S. Yoshida, 1966, “Theoretical study of temperature rise at contact surface for reciprocating motion,” *American Inst. Chemical Eng*., 4, Paper 127, pp. 127-132.

[18] Blok, H. 1937, “Theoretical study of temperature rise at surfaces of actual contact under oiliness lubricating conditions,” *Institution of Mechanical Engineers*, 2, pp. 222-235.

[19] Jaeger, J. C., 1942, “Moving sources of heat and temperatures at sliding contacts,” *Proc. Royal Society. N. S. W*., 56, pp. 203-224.

[20] Holm, R., 1948, “Calculation of the Temperature Development in a Contact Heated in the Contact Surface, and Application to the Problem of the Temperature Rise in a Sliding Contact,” *Journal of Applied Physics*, **19**, p.361-366.

[21] Archard, J. F. “The temperature of rubbing surfaces,” 1958-1959, Wear, 2, pp 438-455.

[22] Francis, H. A., 1970, “Interfacial temperature Distribution within a Sliding Hertzian Contact,” ASLE Transactions, **14**, pp. 222-235.

[23] Carslaw, H. S., and Jaeger J. C., 1950 “*Conduction of Heat in Solids*”, Oxford University Press.

[24] Gecim, B., and Winer, W. O., 1984, “Steady Temperature in Rotating Cylinder Subject to Surface Heating and Convective Cooling”, *ASME Journal of Tribology*, 106, p. 120-127.

[25] Greenwood, J. A. and A. F. Alliston-Greiner, 1992, “Surface temperatures in fretting contact,” *Wear*, 155, p. 269-275.

[26] Furey, M. J., Vick, B., Foo, S. S., and Weick, B. L.,1990, “A Theoretical and Experimental Study of Surface Temperatures Generated during fretting”, *Proc. Japan International Tribology Conference, Nagoya*, Vol. 2, pp. 809-814.

[27] Tseng, A. A., 1999, “Thermal Modeling of Roll and Strip Interface in Roliing Processes: Part 1 – Review”, Num. Heat Transfer, Part A, 35, pp. 115-133.

[28] Rashid M. and Seireg A., 1987, “Heat Partition and Transient Temperature Distribution in Layered Concentrated Contacts. ” Part I – Theoretical Model. *JOURNAL Tribology*, 109, pp. 487-495

[29] Rashid M. and Seireg A., 1987, "Heat Partition and Transient Temperature Distribution in Layered Concentrated Contacts. Part II – Dimensionless Relationships and Numerical Results." *Journal of Tribology*, 109, pp. 496-502.

[30] Abdel-Aal H. A. and Smith S. T., 1998, "Thermal Compatibility of Metallic Pairs in Sliding Contact." *Int. Comm. Heat Mass Transfer*, 25, No. 5, pp. 599-608

[31] Abdel-Aal H. A., "Division of Frictional Heat: The Dependence on Sliding Parameters." *Int. Comm. Heat Mass Transfer*, 26, No. 2, pp. 279-288.

[32] Abdel-Aal H. A., "A note on the Intrinsic Response of Metallic Pairs in Dry Sliding Friction." *Int. Comm. Heat Mass Transfer*, 26, No. 2, pp. 289-298.

[33] Floquet A., and D. Play, 1981, "Contact Temperature in Dry Bearings - Three Dimensional Theory and Verification." Journal of lubrication Technology, 103, pp. 243-252.

[34] Robert D. Cook, David S. Malkus, and Michael E. Plesha, 1989, *Concepts and Applications of Finite Element Analysis.* John Wiley & Sons.

[35] Boley, Bruno A., 1985, *Theory of Thermal Stresses.* Krieger Pub. Company.

[36] Krishnamurthy H. 2002, "Application of Duhamel's Theorem to problems involving oscillating heat source", M.S. Thesis, Louisiana State University, Baton Rouge, Louisiana.

[37] Tseng A. A, Tong, S., and Lin, S.S., 1989, "Thermal Stresses of Rotating Rolls in Rolling Processing." *Journal of Thermal Stresses*, 12, pp. 427-450.

[38] Mills A.F., 1995, *Heat and Mass Transfer*, Richard D Irwin Inc.

[39] Khonsari, M. M., and Hua, D. Y., 1993, "Genralized Non-Newtonian Elastohydrodynamic Lubrication", Tribology International, 26, No. 6, p. 405-411.

[40] Johnson, K. L., *Contact Mechanics*, Cambridge University Press, 1985.

[41] Persson, A., 1964. "On the Stress Distribution of Cylindrical Elastic Bodies in Contact", Dissertation, Chalmers Tekniska Hogskola, Goteborg, pp. 117-118.

[42] Hou J. P. and D A Hills, 2000, "Contact between a pin and a plate with a hole under interference-fit and clearance-fit conditions." *Proc. Instn. Mech. Engrs*. 215, Part C, pp. 629-639.

[43] Mansouri, M., and Khonsari, M. M., 2005, "Surface temperature in oscillating sliding interfaces." *Journal of Tribology*, 127, No. 1, pp. 1-9

[44] Patankar, S.V., 1980, *Numerical Heat Transfer and Fluid Flow.* Hemisphere.

[45] Wang, P., Hua, D. Y., Mansouri M., and Khonsari M. M., 2006, "Evaluation of Critical Design Factors on the Thermal Behavior due to Frictional Heat in the Oscillatory Sliding Conformal Contact. " *Proc. of the 2006 ASME International Mechanical Engineering Congress and Exposition*, Nov. 5-10, Chicago, Ill, USA.

[46] Zhang G., S. Jack Hu and Xin Wu, "Numerical analysis and optimization of hemming processes.**"** *Journal of Manufacturing Processes*, 2 No.4, p241-246.

[47] Sacks, J., Welch, W.L., Mitchell, T.J. and Wynn, H.P., 1989, "Design and analysis of computer experiments." *Statistical science*, 4, No.4, pp. 409-435

[48] Sacks, J., Schiller, S.B., and Welch, W.J., 1989,"Designs for computer experiments." *American Statistical Association and the American Society for Quality Control, Techometrics*, 31, No.1,pp. 41-47

[49] Mansouri, M., Holgerson, M., Khonsari, M. M., and Aung, W., 2002, "Application of Analysis of Variance to Wet Clutch Engagement." *Journal of Engineering Tribology, Proceedings of the Institution of Mechanical Engineers*. 216, No. J3. pp. 117-126.

[50] Montgomery, D. C., 2001, *Design and Analysis of Experiments*. John Wiley & Sons, Inc. New York.

[51] Hsu, Y. C. and Burton, R. A., 1967, "Exact Thermoelastic Solutions for Clearance Variation in a Short Cylindrical Bearing Configuration with Unsymmetrical Frictional Heating." *Journal of Lubrication Technology*, pp. 167-176.

[52] Özisik, M. N. 1993, *Heat Conduction.* John Wiley & Sons, New York, NY.

[53] Polycarpou, A. A., and Soom, A., Jan. 1995, "Two-Dimensional Models of Boundary and Mixed Friction at a Line Contact." *Trans. ASME*, 117, pp. 178-184.

[54] Polycarpou, A. A., and Soom, A., Jan. 1996, "Two-Componenet Mixed Friction Model for a Lubricated Line Contact." *ASME Journal of Tribology*, 118, pp. 183-189.

[55] Dowson, D. and Higginson, G. R., 1977, *Elastohydrodynamic Lubrication.* Pergamom Press, Oxford.

[56] Play D. and Godet M., 1977, "Design of High performance Dry Bearings", *Wear*, 141, pp. 25-44.

[57] Kannel J. W., and Barber S. A., 1989, "Analysis of Scuffing Temperatures With Considerations of Wear." *Journal of Tribology*, pp. 1-5.

[58] Uetz, H., Richter K. and Wiedemeyer J., 1983, "System Temperature and Tribological Behavior of Polymer-metal sliding couples in Pin-on-Disk Model testing." *Wear*, 88, pp. 103-114.

[59] Berthier Y. and Play D., 1982, "Wear Mechanisms in Oscillating Bearings." *Wear*, 75, pp. 369-387.

[60] Stachowiak G. W., and Batchelor, A. W., 2000, *Engineering Tribology*. Butterworth-Heinemann.

[61] Waterhouse R.B., 1992, *Fretting Wear.* ASM Handbook. 18, p. 242.

[62] Huq M.Z., Butaye C, and Celis J-P., 2000, "An innovative system for fretting wear testing under oscillating normal force." *Journal. Mater. Res*., 15, pp. 1591-1599.

[63] Kennedy P., Peterson M.B., and Stallings L., 1982, "An Evaluation of Fretting at Small Slip Amplitudes." *ASTM STP 780*, p. 30.

[64] Sandstrom P.W., Sridharan K., and Conard J. R., 1993, "A fretting wear study of a nitrogen implanted titanium alloy." *Wear*, 166, p. 163.

[65] Anders Ekberg, 1997, "WEAR - SOME NOTES." Dep. of Solid Mechanics, Chalmers University of Technology.

Appendix A. Axial Averaging Correction Procedure

The source term generated from axial averaging of the thermal problem is believed to be in error due to the uncertain end-point Boundary conditions. A method is proposed here to match the computed temperature with the experimental values throughout the duration of a test until steady state. One way to adjust the axial averaging is to use an error measure and iterate such that the overall error, between the computed and measured temperatures, remains small. The following description considers a scalar correction function representing the overall error that is to be added to the derived source term, which was generated from axial averaging of the thermal problem, in each component of the pin-bushing system.

Temperature measurements in the test rig are taken at four locations at the mid-plane on the bushing surface, 45 degrees apart as described in detail in Chapter 3. The error between the computed and measured temperature is $E_T^l = \left(T_m - T_c\right)^l$, where the superscript (*l*) denotes the thermocouple locations, and the subscripts (*m*) and (*c*) indicate measured and computed temperatures, respectively. Iteration may be performed to simultaneously minimize the total error with respect to the four thermocouples. The overall error measure is defined as follows:

$$E_{TT} = \sum_{l=1}^{4} E_T^l = \sum_{l=1}^{4} \left(T_m - T_c\right)^l \tag{A1}$$

Since the computed temperature at the end point $z = -L/2$ of the shaft depends on the computed temperatures at the thermocouple locations, this scalar equation may be used to determine the additional source term, $q_b^{'} = -\left(h_e^{'}/L\right)\left(T - T_e\right)$, where $h_e^{'}$ is the correction to the assumed heat transfer coefficient. An average value of this heat transfer coefficient may be estimated as follows:

Compute the average temperature rise T_a and correction term, $q_{b,a}^{'}$, at the end point and estimate the average heat transfer coefficient using:

$$h_{e,a}^{'} = -Lq_{b,a}^{'} \Big/ \left(T_a - T_e \right) \tag{A2}$$

This determines the heat transfer coefficient that minimizes the total error between the measured and computed temperatures. The modified heat transfer problem is now stated as follows:

Compute the heat equation

$$\rho c \frac{\partial T}{\partial t} + m\rho c\dot{\phi}(t) \frac{\partial T}{\partial \theta} = k\nabla^2 T + q_b + q_b^{'} \tag{A3}$$

Subject to the given boundary conditions, with the added requirement that the error between computed and measured temperature is algebraically minimized

$$\frac{dE_T^l}{dt} - \sum_{l=1}^{4} w_l \left(T_m - T_c \right)^l = 0 :: l = 1,2,3,4 \tag{A4}$$

where w_l, $l = 1-4$, are weight factors such that, $0 \le w_l \le 1$, selected for the measured temperatures. The adjusted heat source is set to its average value given by the overall error $q_b^{'} = E_{TT}$.

Preliminary calculations using this procedure show great improvement in the results. This was achieved at the expense of very oscillatory heat source compensation. The oscillatory behavior is thought to be due to attempting to correct large discrepancies between the measured and computed values. The validity of this result is yet to be justified. Moreover, the adjusted heat source must be curve fit in terms of key process parameters and generalized for use in the solution of an arbitrary pin-bushing pair. This requires additional simulations and comparisons to measured data.

Appendix B. Ambient Heat Transfer Coefficient

The convection heat transfer coefficient between the ambient surroundings and the outer boundary of the bushing can be estimated using empirical relations proposed by Mills [38]. He considers a cylinder rotating in an infinite quiescent fluid medium. The empirical relation reads:

$$Nu_D = 0.133\,\mathrm{Re}_D^{\,2/3}\,\mathrm{Pr}^{1/3},\ \mathrm{Re_D} = \omega D^2/\nu \tag{B1}$$

An additional Nusselt number due to free convection is used to compute the total Nusselt number. This is given by:

$$Nu_0 = \left[0.60 + \frac{0.387 Ra^{1/6}}{\left(1 + \left(\frac{0.559}{\mathrm{Pr}}\right)^{9/16}\right)^{8/27}}\right]^2 \tag{B2}$$

$$Ra = \frac{g\beta\left(T_s - T_e\right)D^3}{\nu\kappa},\ \beta = 1/T_e \tag{B3}$$

$$Nu = Nu_D + Nu_0 = h_e D/k \tag{B4}$$

where

Nu_D = the Nusselt Number for forced convection,

Nu_0 = the Nusselt Number for free convection,

$\mathrm{Re_D}$ = the Reynolds number,

Pr = Prandtl Number.

h_e = Convective heat transfer coefficient, W/m^2-C

D = Diameter of the surface exposed to convection, m

k = Thermal Conductivity of the convecting fluid, W/m-C.

κ = Thermal diffusivity of the convecting fluid, m^2/s.

$\dot{\omega}$ = Angular velocity of the rotating member, rad/s

ν = Kinematic viscosity of the convecting fluid, m^2/s.

$T_s - T_e$ = Surface temperature rise above ambient (K),

T_e = Fluid temperature.

The validity of the above relations was verified by Krithivasan [10], with air as the convecting fluid at room temperature, by using the empirical relations to estimate the convection heat transfer coefficient of an axle and cone problem solved by Wang et.al [8]. The convection between the outer boundary of the bushing and the ambient is found by assuming a mild flow of air over the bushing outer surface at a speed of 10 mph, at a temperature of T_e = 300 K. The properties for the convecting fluid (Air) can be found in Özisik [52]. Using T_e = 300 K (Room Temperature), $T_s - T_e$ = 100 K, Pr = 0.69 (for air), ν = 15.89 x 10^{-6} m^2/s, k = 26.3 x 10^{-3} W/m-C, and κ = 22.5 x 10^{-6} m^2/s, and assuming bushing diameter of 1 inch, we find h_e ~ 80 W/m^2-C.

Appendix C. Interfacial Heat Transfer Coefficient

Preliminary computations and measurements of the surface temperature rise, under heavy loads and oscillatory motion revealed that surface temperatures can reach high steady state values ranging from 150 ^{o}C to 450 ^{o}C. Therefore, the convection and radiation properties of the interface need to be evaluated. Krithivasan [10] evaluated the convective heat transfer coefficient based on the empirical relations for a range of temperatures from room temperature to 1100 K, where the medium within the clearance of the pin and bushing is air. An average value of h_{fluid} = 10 W/m^2-C was found for the convection heat transfer coefficient of hot air.

A linearized model of the radiation exchange at the interface was performed to estimate the equivalent heat transfer coefficient due to radiation h_{rad}. Let T_{h} be the surface temperature of the hotter body and T_{c} that of the cooler body. The heat flux due to radiation exchange may be written as follows:

$$q_{rad} = \varepsilon\sigma\left(T_h^{\,4} - T_c^{\,4}\right) = h_{rad}\left(T_h - T_c\right) \tag{C1}$$

So that,

$$h_{rad} = \varepsilon\sigma\left(T_h^{\,2} + T_c^{\,2}\right)\left(T_h + T_c\right) \tag{C2}$$

where ε is the emissivity of the radiating body (ε = 0.4 for steel), and σ is the Stefan-Boltzmann's constant (σ = 5.6696 x 10^{-8} W/m^2-K^4) and the surface temperatures are in absolute units (K). Clearly, the equivalent convective coefficient due to radiation is rather a nonlinear function of the surface temperatures. The equivalent model estimated by Krithivasan [10] was plotted as a linear and increasing function of time, which does not seem to be practical, especially considering the steady state. The variation of h_{rad} with temperature is insignificant at low surface temperatures. At high surface temperatures, h_{rad} varies as a function of the

arithmetic average of the surface temperatures, as given above. The total equivalent heat transfer coefficient within the enclosure is given by the combined effects:

$$h_g = h_{fluid} + h_{rad} \tag{C3}$$

Appendix D. Dynamic Coefficient of Friction

A simple model for the instantaneous friction coefficient was proposed and tested by Polycarpou and Soom ([53]-[54])

$$\mu(t) = \frac{c_1 e^{-c_2 V(t)}}{1 + c_3 \left(a(t)/L_c \right)^2 \left(\eta_i/\eta_0 \right) \left(1 - e^{-dH(t)} \right)} \tag{D1}$$

$$V = \eta_i \alpha v_s / a \,,\; H(t) = \frac{h_0(t)}{\sigma \dfrac{a(t)}{L_c} \sqrt{\eta_i/\eta_0}} \tag{D2}$$

The dimensionless film thickness $H(t)$ is defined so as to represent the sliding speeds, the normal load, the changing contact width, the lubricant, and surface roughness. The central film thickness, $h_0(t)$, for a line contact between smooth surfaces is given by the Dowson-Higginson formula [55]

$$h_0(t) = \frac{5}{2} r_c \left(\frac{\alpha \eta_i v_s}{r_c} \right)^{0.70} \left(2\alpha E_c \right)^{0.10} \left(\alpha p_m \right)^{-0.26} \tag{D3}$$

where α_p is the pressure-viscosity coefficient, η_i is the viscosity at the inlet, v_s is the sliding speed, p_m is the mean Hertzian contact pressure,

$$p_m = \frac{w_a(t)}{2a(t)L_c},\ a(t) = \sqrt{\frac{4w_a(t)r_c}{\pi E_c L_c}}. \tag{D4}$$

where w_a is the normal load, L_c is the length of contact, $a(t)$ is the semi-contact width. The constant empirical coefficients c_i are determined from curve fitting measurements.

Appendix E. Thermal Contact Resistance

There is likely to be discrepancies in the contact mechanism and the amount of heat input actually used by the experiments due to misalignment and error in the contact area. Other sources of error come from a lack of knowledge of thermal conductance at the contact junction and the gap interface surrounding it.

The perfect contact theory is not accurate. Use of a thermal contact resistance model may in effect be appropriate. Considering a thermal contact conductance law at the interface, the mixed BC in Equation (6) may be modified to read

$$k\frac{\partial T(r,\theta,t)}{\partial n} + h\Delta T = q_c \tag{E1}$$

The thermal interfacial conductance *h*, represents thermal contact resistance at the contact junction and the thermal conductance within the gap where there is no contact.

$$h\Delta T = h\left(T_{(1)} - T_{(2)}\right) :: \text{For body 1} \tag{E2}$$

$$h\Delta T = h\left(T_{(2)} - T_{(1)}\right) :: \text{for body 2.} \tag{E3}$$

where

$$h(\theta,\phi) = \begin{cases} h_c\left(p\right) & \text{on } \mathcal{S}_{\text{c}} \\ h_g(\bullet) & \text{on } \mathcal{S}_{\text{g}} \end{cases} \tag{E4}$$

In a study by Tseng A. [27] on rolling processes, the thermal contact conductance at the contact junction is given by

$$h_c = 3800 k_h \sigma^{-0.257} \left(\frac{p}{p + H_a} \right)^{0.94} + \left(\frac{k_m}{\delta_m} \right) A_r \qquad \text{(E5)}$$

where k_h is the harmonic average of the thermal conductivities of the contacting bodies, σ is the surface roughness height *rms* value, p is the contact pressure, H_a is the hardness of the softer material, k_m is the thermal conductivity of the fluid film at the interface, and δ_m its thickness, and A_r is the ratio of the real contact area to the nominal area of contact.

Vita

Mongi Mansouri was born and raised in a small village in Beja, Tunisia. After completing his secondary school education in Beja, Tunisia, with a Baccalaureate degree, he moved to the United States under a scholarship program in order to pursue a higher education in engineering.

In the United States, He attended the Center for English as a Second Language program at Southern Illinois University at Carbondale. In 1983 he moved to Minneapolis, Minnesota, where he attended the University of Minnesota's Institute of Technology and earned a Bachelor of Science in Mechanical Engineering degree in June 1986.

In August 1986, he joined the Department of Mechanical Engineering at Carnegie Mellon University, where he completed his Master of Engineering degree in August 1988.

He transferred to Louisiana State University, Baton Rouge, Louisiana, in August 1999 to pursue the doctoral program in the Department of Mechanical Engineering. His major research was in the field of tribology under the supervision of Dr. Michael M. Khonsari, with a minor in civil engineering mechanics. During this program, he participated in several research projects, and attended Caterpillar Inc., Peoria, Illinois, in 2004 for an internship in the Materials Technology division.

He earned a Doctor of Philosophy degree in mechanical engineering in December 2007. His research interests are in the fields of tribology, heat transfer, computational mechanics, and advanced engineering analysis and design. He plans to pursue these research fields in future research/teaching/career endeavors.